Politecnico di Milano

Dipartimento di Scienze e Tecnologie Aerospaziali

Corso di Laurea Magistrale in Ingegneria Aeronautica

Development and implementation of an aeroacoustic module for wind turbine noise prediction

Relatore: Prof. Alessandro CROCE

Tesi di Laurea di:

Carlo Rosario SUCAMELI

Matricola: 837050

Anno Accademico 2016-2017

Ringraziamenti

È stato un percorso lungo quello che mi ha portato fino a qui. Nel concludere un altro capitolo della mia vita, non posso fare a meno di ringraziare le persone che hanno reso possibile la realizzazione di questa tesi.

Vorrei ringraziare il mio relatore, il Professor Alessandro Croce, innanzitutto per avermi dato la possibilità di affrontare questa stimolante sfida lasciandomi ampio margine di ricerca e mantenendo al contempo salda la direzione del lavoro, ma sono soprattutto grato per la serietà ed il rispetto con cui sono sempre stato trattato: è una qualità che ho molto apprezzato.

Ho avuto inoltre la magnifica possibilità di trascorrere parte del periodo di tesi all'università tecnica di Monaco, e di questo sono molto grato.

Un ringraziamento speciale e sentito vorrei dedicarlo a Pietro Bortolotti, il cui aiuto è stato di fondamentale importanza e senza il quale non sarei mai riuscito a farcela.

Infine, il più grande ringraziamento va ai miei genitori, per la loro completa e totale fiducia nei miei confronti. Non ho mai percepito alcun dubbio da parte vostra, e cercherò di non deludervi mai nella vita, come voi non avete mai deluso me.

Questo traguardo è tanto mio quanto vostro.

Abstract

The present thesis work, conducted at Politecnico di Milano and Technische Universität München, focused on developing and implementing an aeroacoustic code for wind turbine noise prediction through semi-empirical frequency based methods. The noise analysis tool has been included in *Cp-Max*, the framework in use for wind turbine simulation and design.

Frequency based methods consider contributions of different noise sources: turbulent boundary layer - trailing edge and turbulent inflow noise have been taken into account, and most of the models present in the literature were included in the aeroacoustic module. Turbulent boundary layer - trailing edge noise has been computed according to *Brooks, Pope, Marcolini* (*BPM*) and *TNO* model, while turbulent inflow noise is calculated through *Amiet* and *Lowson* models.

Anisotropy of boundary layer can be considered for the *TNO* model according to *Bertagnolio*, and the software *Xfoil* was included for turbulent boundary layer characterization. Validation of the noise sources implemented is performed through direct comparison with experimental results from different researches, and discrepancies among models have been investigated, particularly between *BPM-TNO* and *Amiet-Lowson*.

The aeroacoustic tool implemented have been tested on a $3.6MW$ wind turbine model, where it has shown the ability of predicting reasonable results and reproducing typical trends of wind turbine noise spectra. No validation of the code has been possible, due to unavailability of detailed wind turbine and noise measurements data.

Keywords: Wind energy, wind turbine, Cp-Max, Cp-Lambda, aeroacoustic, trailing edge noise, turbulent inflow noise, BPM, TNO, Amiet, Lowson

Sommario

Il presente lavoro di tesi, condotto presso le università Politecnico di Milano e la Technische Universität München, si è concentrato sullo sviluppo e l'implementazione di un codice aeroacustico per il calcolo del rumore prodotto da generatori eolici, attraverso l'impiego di metodi in frequenza. Lo strumento sviluppato è stato incluso in *Cp-max*, il framework utilizzato da entrambe le università per la simulazione ed il design di aerogeneratori.

I metodi in frequenza considerano il contributo al rumore fornito da diverse sorgenti acustiche: il codice sviuppato tiene in conto di *turbulent boundary layer - trailing edge noise* ed il *turbulent inflow noise*, includendo molti dei modelli attualmente in uso nella letteratura per la previsione di tali contributi. Il calcolo del *turbulent boundary layer - trailing edge noise* è reso possibile attraverso l'inclusione dei modelli *Brooks, Pope, Marcolini* (*BPM*) e *TNO*, mentre il *turbulent inflow noise* è dato dai modelli di *Amiet* e di *Lowson*. Nel modello *TNO* è stata inclusa la possibilità di tenere in conto dell'anisotropia dello strato limite turbolento, come riportato da *Bertagnolio*, ed il software *Xfoil* è stato utilizzato per il calcolo degli strati limite turbolenti. Le implementazioni delle varie sorgenti sono state validate attraverso la comparazione con risultati sperimentali provenienti da differenti fonti; i modelli sono inoltre stati confrontati tra loro, al fine di valutarne le discrepanze, specialmente tra i modelli *BPM-TNO* e *Amiet-Lowson*.

Il codice aeroacustico implementato è stato infine verificato su un modello di aerogeneratore da $3.6MW$, ed è stata dimostrata l'effettiva capacità dello strumento di prevedere risultati ragionevoli e di riprodurre correttamente tendenze tipiche di emissioni acustiche di aerogeneratori. Una validazione del modulo non è stata possibile, a causa della mancanza in letteratura dei dettagliati dati geometrici, operativi ed acustici necessari al funzionamento del codice.

Parole chiave: Energia eolica, aerogeneratore, Cp-Max, Cp-Lambda, aeroacustica

Contents

List of Figures

List of Tables

Chapter 1

Introduction

Importance of wind energy has progressively increased over the past decades, due to a growing need of sustainable energy. According to WindEurope[1], formerly the European Wind Energy Association (EWEA), $12.5GW$ of wind capacity has been installed only in 2016, leading to a total capacity of $153.7GW$ and overtaking coal as the second largest form of power source (Fig:1.1). Wind power today meets 10.4% of EU's power requirements, and is considered to be the key for EU's long term decarbonisation.

The constant need of renewable energy has led to increasing issues in finding suitable sites for wind farms, pushing the wind industry to offshore power plants. Onshore wind turbines are usually located on remote or rural areas, far away from human dwellings: a key factor for public acceptance of wind energy is in fact reduction of noise emission from wind turbines. A lot of effort has been made in developing increasingly bigger and more efficient wind turbines (1.2), able to produce more power and supplying the growing request of power at a price of higher noise production.

Wind energy industry is interested in integrating wind turbines in urban environment; for this reason noise production is rapidly becoming an important parameter to be taken into account already in the design process.

[1] https://windeurope.org/

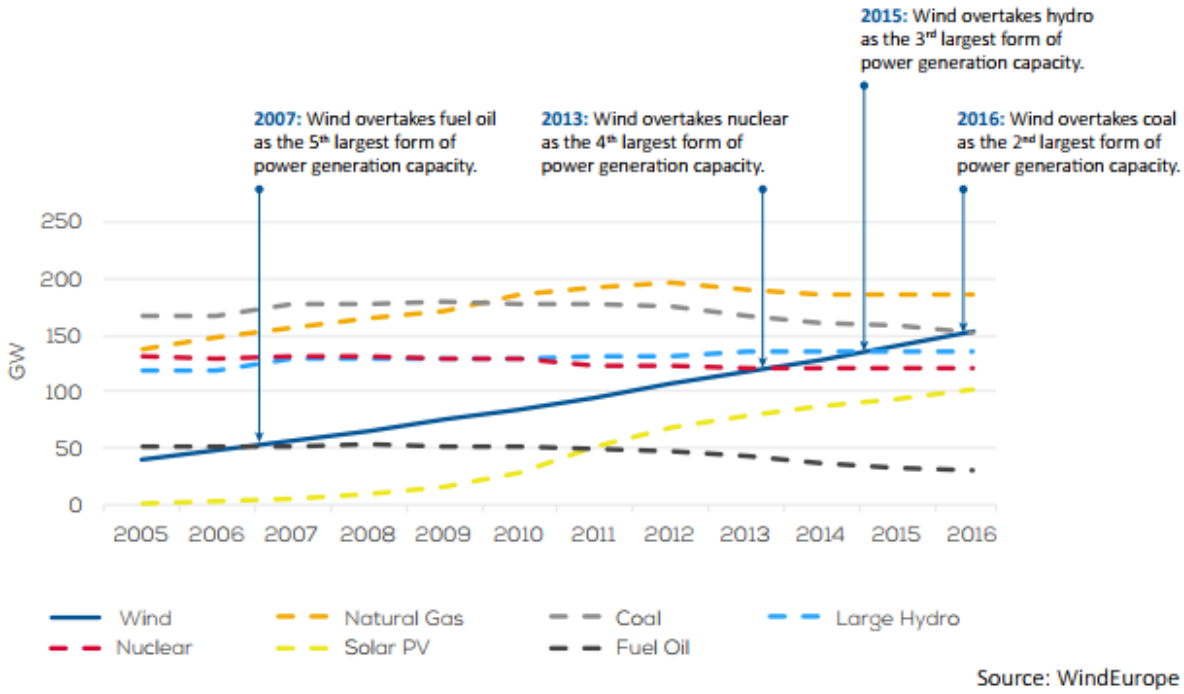

Figure 1.1: Cumulative power capacity in the European Union 2005-2016. Image taken from WindEurope: 2016 European statistics

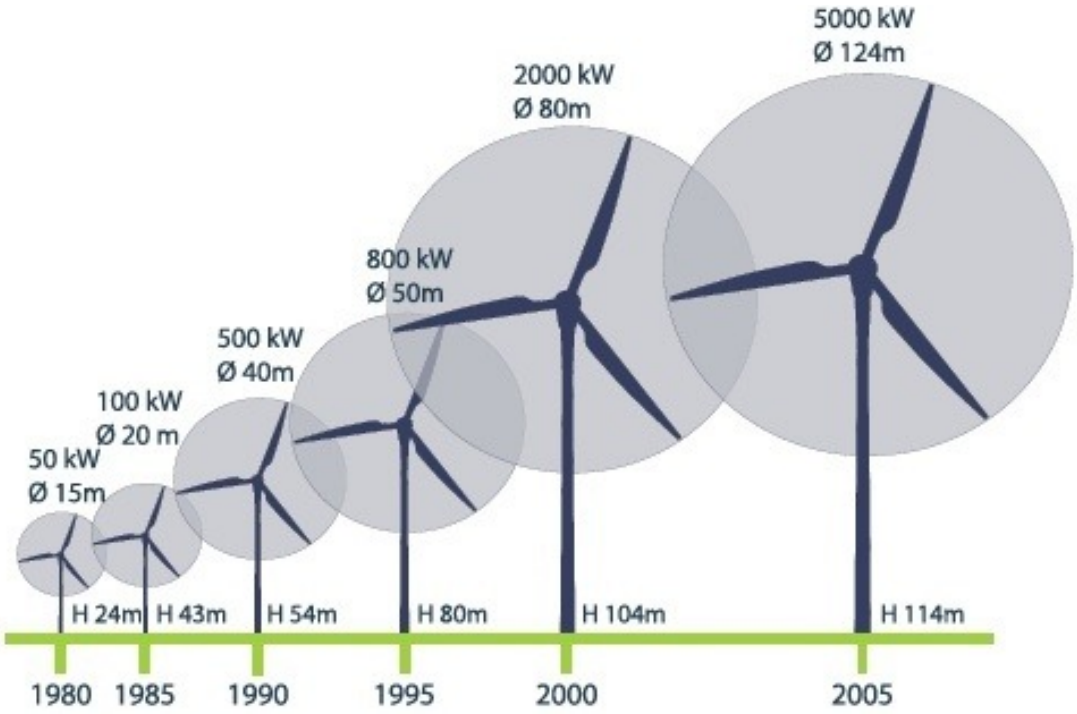

Figure 1.2: Trend of wind turbine size

Wind turbine noise is usually distributed over a broad range of frequencies and considered annoying by people, being constant and repetitive. For this reason, many countries possess regulations to limit noise emissions in urban and rural area. Example of noise limitations for different countries is given in Tab.1.1, taken from [1].

Country	**Regulations or Guideline**
Australia	Greater of 35/40 dBA or existing plus 5 dBA
Canada (Ontario)	40 dBA to 51 dBA; increasing with increasing wind speed. 40 dBA is typically controlling limit
Denmark	Typically 42 dBA @ 6 m/s and 44 dBA @ 8 m/s
Germany	35 to 40 dBA at night
Netherlands	41 dBA at night or 47 dBA as annual average
United Kingdoom	Greater of 43 dBA or 5 dBA above existing at night

Table 1.1: Noise emission limits for different countries

All wind speeds are referred to $10m$ height according to IEC61400-11[2], that reports all details of acoustic noise measurements of wind turbines.

From what said above, it is clear that noise computation is a state of the art problem for wind turbine applications, and development of tools for noise prediction is still an interesting and open problem.

1.1 Aim and organization of the project

The present thesis work has been developed at Politecnico di Milano (PoliMi) and Technische Universität München (TUM), and was motivated by the need of including an aeroacoustic tool in the current framework used for wind turbine design. Objective of the project was to study, develop and implement a noise analysis tool for wind turbines based on semi-empirical models, which are the state of the art in wind energy industry.

A brief description of each chapter is given below, to help the reader understand the whole picture of the project:

- **Chapter 1** gives an overview on wind energy status and explains importance of noise emissions of wind turbines.
- **Chapter 2** introduces all the theoretical tools needed to understand the current work. Theory of aeroacoustics, state of the art and noise sources description is also given.
- **Chapter 3** accurately describes all the noise source models implemented.
- **Chapter 4** gives an explanation of the numerical tools used in this thesis. Wind turbine framework is described, with a detailed overview of the aeroacoustic module developed.
- **Chapter 5** compares results among all the noise sources in a 2d solver, in order to evaluate correct implementation and discrepancies between the models.
- **Chapter 6** investigates noise results obtained on a wind turbine model, together with a sensitivity analysis on the aeroacoustic tool.
- **Chapter 7** concludes the work, summing up all the main achievements of the project and suggesting interesting possible developments.

Chapter 2

Fundamentals of aeroacoustics

This chapter gives the reader a general overview on the theory behind aeroacoustics necessary for comprehension of the terms presents in the following sections. At first a general introduction to sound is given, with particular attention on the human perception of noise. Useful quantities necessary for aeroacoustic measurements are described, such as sound pressure level, intensity, power level and others. A brief introduction to theoretical aeroacoustics work from *Lighthill*[3] is given, together with a description of state of the art in wind turbine noise predictions. At last, an overview of noise mechanisms of wind turbine gives the basis for noise source modeling, which is the object of the next chapters.

2.1 Introduction to sound

Sound is a vibration that propagates through a medium as wave. Sound waves in air are characterized by rapids and small fluctuations of atmospheric pressure around a mean value, perceived by humans through the sense of hearing. Being composed of waves, sound has an energy content distributed at different frequencies: human ear can perceive sounds on a range between $20Hz$ and $20kHz$ for a young and healthy person, and this range tends to decrease with the age. A sound is said to be *broadband* when energy is distributed over a broad portion of the frequency spectrum, while is called *narrowband* when it occupies only a small portion of it. It is important to remark that, even though human ear is able to hear sounds on a broad range of frequencies, it is not equally sensitive to all of them, nor it reacts

linearly to changes in amplitudes of sound.

2.1.1 Sound levels

Due to the fact that humans do not react linearly to changes in sound amplitude, a doubling in sound emissions is not perceived as a noise twice louder but less. This fact has led to adoption of logarithmic scale for sound level measurements. The *sound pressure level* is then defined as:

$$SPL = 10 \log_{10} \left(\frac{p^2}{p_{ref}^2} \right) \tag{2.1}$$

Where p indicates the pressure amplitude and p_{ref} is a reference pressure value (usually $p_{ref} = 20\mu Pa$). Sound pressure levels are measured in dB, and a doubling in sound amplitude would produce an increase in only $\approx 3dB$: a representation of typical noise emissions is given in fig:2.1.

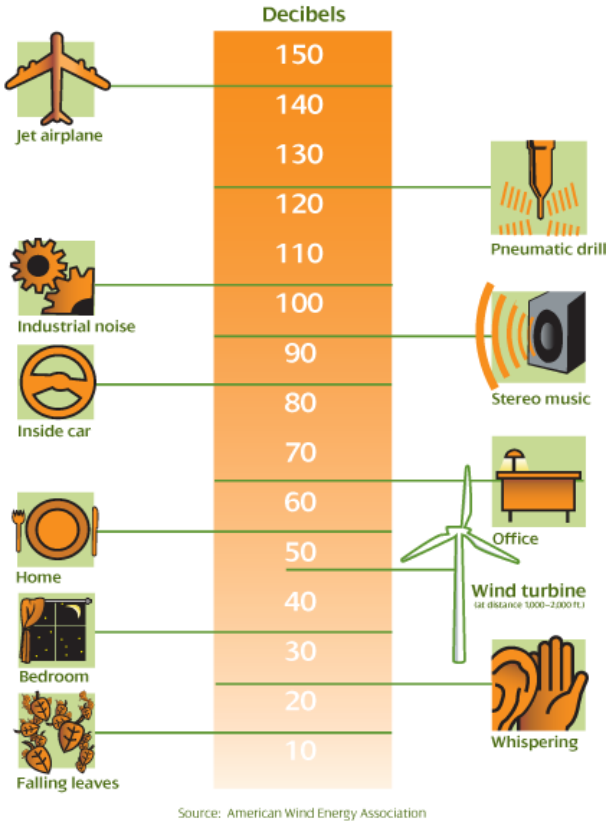

Figure 2.1: Sound Pressure levels for different noise sources

A very important property is that the sound pressure levels of different sources can be summed up to give the total sound pressure level:

$$SPL_{Tot} = 10\log_{10}\left(\sum_{i=1}^{n} 10^{0.1SPL_i}\right) \tag{2.2}$$

In which n indicated the number of sources involved in the summation.

Sound intensity level can also be determined by making use of the sound intensity:

$$SIL = 10\log_{10}\left(\frac{I}{I_{ref}^2}\right) \tag{2.3}$$

With I sound intensity and I_{ref} reference intensity value, both measured in $[W/m^2]$ ($I_{ref} = 10^{-12}W/m^2$). Noise intensity allows computation of sound power, defined as the integral of intensity on a surface S:

$$P = \int_S IdS \tag{2.4}$$

Allowing computation of sound power level as:

$$SWL = 10\log_{10}\left(\frac{P}{P_{ref}}\right) \tag{2.5}$$

With $P_{ref} = 10^{-12}W$

It must be remarked that sound pressure level depends on the sound and on the relative position between source and observer, while sound power level is a property of the noise source, representing the acoustic power emitted. Conversion between sound pressure level to sound power level can be performed through the following expression, reported in IEC 61400-11[2].

$$SWL = SPL + 10\log_{10}\left(\frac{4\pi R_{obs}^2}{S_0}\right) - B \tag{2.6}$$

With R_{obs} distance between source and observer, S_0 is a reference surface ($1m^2$) and $B = 6$.

2.2 Frequency Analysis

As already mentioned, sound can be distributed over a broad range of frequencies, meaning that a frequency analysis of the signal constitutes an important part of sound identification. Even though it is possible to analyze amplitude of noise for single frequencies, this approach is not necessary; Audible range is usually divided into smaller bands, and signal is analyzed only inside this bandwidth, excluding the rest. The most common frequency discretization is the octave band, in which each band is characterized by an upper bound and lower bound related by:

$$f_u = 2f_l \tag{2.7}$$

Frequency can the be discretized on octave band or fraction of octave, such as the *1/3 octave band discretization:*

$$f_u = 2^{1/3} f_l \tag{2.8}$$

This last discretization being very used for noise measurements. For each band it is possible to compute the center frequency f_c:

$$f_c = \sqrt{f_l f_u} = \sqrt{2^k} f_l \tag{2.9}$$

Where k indicates the octave band fraction discretization (i.e $1, 1/3, etc...$). Example of 1/3 octave discretization is reported in tab:2.1 It is possible to compute also the frequency bandwidth:

$$\Delta f = f_u - f_l = 2^k f_l - f_l = f_l(2^k - 1) = \frac{f_c}{2^{k/2}}\left(2^k - 1\right) = f_c\left(2^{k/2} - \frac{1}{2^{k/2}}\right) \tag{2.10}$$

By making use of the above formulas, it is possible to relate the power spectral density of a noise spectrum to sound pressure levels defined in octave bands, by multiplying the PSD evaluated at a center frequency f_c for the respective pulsation bandwidth $\Delta\omega = 2\pi\Delta f$:

$$SPL(\omega) = 10\log_{10}\left(\frac{PSD(\omega)4\pi\Delta f(\omega)}{P_{ref}^2}\right) \tag{2.11}$$

Lower band $[Hz]$	**Center frequency** $[Hz]$	**Upper band** $[Hz]$
11.2	12.5	14.1
14.1	16	17.8
17.8	20	22.4
22.4	25	28.2
28.2	31.5	35.5
35.5	40	44.7
44.7	50	56.2
	...	
4467	5000	5623
5623	6300	7079
7079	8000	8913
8913	10000	11220
11220	12500	14130
14130	16000	17780
17780	20000	22390

Table 2.1: 1/3 Octave bands discretization

As already said, humans are not equally sensitive to all the frequencies, but react more for frequencies between $1000Hz$ and $4000Hz$, with very bad response in the low frequency range: for this reason measured pressure levels are often weighted by applying *weighting filters*. Many filters exists in the literature, and some of them are reported in fig:2.2. A-weighting is the most common filter used for noise measurements and its curve represents the human ear response to noise. Analytically, its curve can be given by:

$$R_A(f) = \frac{12200^2 f^4}{(f^2 + 20.6^2)\sqrt{(f^2 + 107.7^2)(f^2 + 737.9^2)}(f^2 + 12200^2)} \tag{2.12}$$

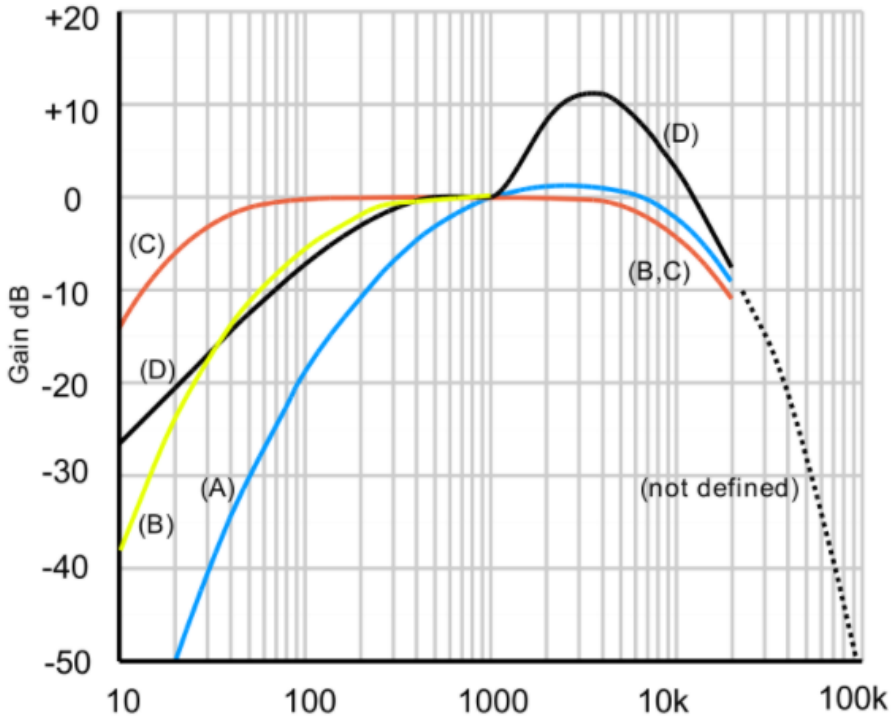

Figure 2.2: Compensation curves for A-B-C-D weighting filters

2.3 Theoretical aeroacoustics

Aeroacoustics research over the past decades starts from the *Lighthill's acoustic analogy*[3], a rearrangement of *Navier-Stokes* mass and momentum equations to give a wave equation for computation of aerodynamic sound:

$$\frac{\partial^2 \rho}{\partial t^2} - c_0^2 \frac{\partial^2 \rho}{\partial x_i^2} = \frac{\partial^2 T_{ij}}{\partial x_i \partial x_j} \tag{2.13}$$

Where $T_{ij} = \rho u_i u_j + p_{ij} - c_0^2 \delta_{ij}$ is called Lighthill stress tensor. Eq 2.13 describes the motion of waves in a fluid at rest forced by the Lighthill stress tensor T_{ij}, which is composed by three terms: flow convection, shear stress and acoustic propagation. For low Mach numbers, Lighthill showed that shear stress and acoustic propagation can be neglected, leading to:

$$T_{ij} = \rho u_i u_j \tag{2.14}$$

Being eq:2.13 a wave equation, solution can be found by making use of linearity and green theorems. If the flow field is known aerodynamic sound can then be computed

through:

$$4\pi c_0^2 \rho = \frac{\partial^2}{\partial x_i \partial x_j} \int_V \frac{T_{ij}\left(y, t - \frac{|x-y|}{c_0}\right)}{|x-y|} dy \tag{2.15}$$

In the volume integral above, T_{ij} is a quadrupole term and must be evaluated at the retarded time, defined as $t_{ret} = t - \frac{|x-y|}{c_0}$.

Lighthill's theory has been extended by Curle [4], incorporating the effects of static solid surfaces on aerodynamic noise. Curle also showed importance of interaction between turbulent flow and solid boundaries on the generation of sound. *Ffowcs-Williams, Hawkings and Hall*[5][6] further extended the theory to take into account influence of arbitrary moving surfaces. Solid surfaces can be acoustically represented as a distribution of monopoles and dipoles, called generally thickness and loading noise. The resulting *Ffowcs-Williams and Hawkings* (FW-H) model has been also reformulated in time or frequency domain, useful formulations are those given by Farassat [7][8]. Many studies have focused on determination of far field noise due to turbulence convecting over an infinitely extended half plane[6][9][10], leading to a scaling law for sound intensity I scattered from an edge:

$$I \approx \rho U^3 \left(\frac{U}{c_0}\right)^2 \frac{\delta}{R} \tag{2.16}$$

With δ length scale of the turbulence. This dependence of sound intensity from the fifth power of U is of great importance, and constitutes a starting point for semi-empirical modeling of noise sources.

2.4 State of the art

Determination of sound emissions has progressively become a very important problem in the wind energy industry. In the literature, approaches typically follows two different paths: computational aeroacoustics methods of semi-empirical methods.

Computational aeroacoustics methods (CAA) are numerical techniques, that allows determination of both noise sources and propagation of sound waves. CAA methods are deeply linked to computational fluid dynamics techniques and

are usually numerically and time demanding; high spatial and temporal resolution is required to capture the small and quick fluctuations generated by sound radiations. A fist category of CAA are the so-called *direct methods*, that couples simultaneous computation of aeroacoustic source region with acoustic propagation to far field. Due to high computational requirements, those methods are very requiring and rarely applied in practice. Another group of CAA techniques are the *hybrid schemes*, that computes source near field pressure fluctuations with CFD (DNS, LES, LEE, etc..) and then propagates it to the far field through wave equations such as those already explained above: FW-H[5], Curle[4], Farassat[7] and others.

Improvements in computational capacity has allowed application of CAA techniques for calculation of noise emissions from rotors, from both helicopters and wind turbines: *Brentner*[11] [12], developed a "near real-time" code (called *WOPWOP*) for helicopter noise computations. *Arakawa et al.*[13] calculated the noise of a wind turbine, by making use of LES for the near-field computation and FW-H for far-field propagation. Others examples of CAA applications can be found in [14],[15],[16].

Semi-Empirical frequency methods are used to approximate sound spectra from wing sections or whole WT configurations, reducing computational time. Those methods are the most used tools for noise prediction in the wind energy industry, thanks to their simplicity and rapidity.

First models used for the computations of wind turbine noise are reported by *Lowson*[17], based on the knowledge of very basic parameters such as rated power, rotor diameter and tip speed. Modeling of aeroacoustic noise sources opened the road to more sophisticated noise prediction tools such as the one developed by *Grosveld*[18] or *Glegg*[19], that take into account contributes of inflow turbulence, turbulent boundary layer - trailing edge and trailing edge bluntness noise. In 1989 *Brooks, Pope ans Marcolini* developed an empirical method based on experimental fitting to compute noise spectra of wing sections, taking into account contributions from 5 self-noise sources: turbulent boundary layer - trailing edge, laminar boundary layer - vortex shedding, trailing edge bluntness, separation-stall and tip noise. The *BPM* model is still one of the most used for wind turbine noise prediction, and

recent work conducted by *Lau*[20] helped improving the model.

A more recent model for turbulent boundary layer - trailing edge noise computation has been developed by *Parchen*[21] and is called TNO: this method, differently from the entirely empirical BPM, uses detailed boundary layer characteristics to compute sound spectra, that must be given through CFD or boundary layer solver.

Another source of great interest is turbulent inflow noise: work due to *Amiet*[22][23] constitutes the basis for computation of noise radiated from a solid surface as a result of incoming gusts of unsteady flow. Starting from Amiet, *Lowson*[17] proposed a correction model to allow smooth transition between low and high frequency range spectra. More recently *Guidati et al*[24] developed a method combining a boundary element method with Amiet theory, improving accuracy of prediction of 2d turbulent inflow noise at the price of a higher computational cost. In order to reduce numerical effort, *Moriarty*[25] designed an empirical correction based on Guidati model to include effects of airfoil shape and angle of attack, not included in the original Amiet formulation.

A number of tools for noise computation have been developed by different authors: *NREL's* code *NAFNoise* by *Moriarty*[26] includes all the mentioned model and computes sound emissions of a 2d wing section. *Fulglsang*[27] from *DTU* implemented a tool based on semi-empirical empirical formulations for wind turbine noise prediction. Also the code SILANT[28], based on BPM model coupled with boundary layer code R-FOIL[29], has been successfully used in SIROCCO[30], an European project that aimed at reducing acoustic emissions from wind turbines.

2.5 Noise sources of wind turbines

Wind turbine noise can originate from different mechanisms: a typical distinction is among *mechanical* noise, generated by gearbox and generator, and *aerodynamic* noise, generated from the interaction between blades and the flow.

- **Mechanical noise** is produced by rotating parts; for this reason its spectrum

is distributed over a narrow band of frequencies, making it a "tonal" noise source. This can be reduced by carefully design of gearbox, acoustic damping of nacelle and generators.

The most problematic noise mechanism that occurs in wind turbine is the aerodynamic noise: division is among self-noise mechanisms and turbulent inflow noise.

- **TI, Turbulent inflow noise** originates from interaction between blades and incident turbulence: eddies of various size impacting on the airfoil cause an unsteady change in loading conditions that produces a broadband noise spectrum.

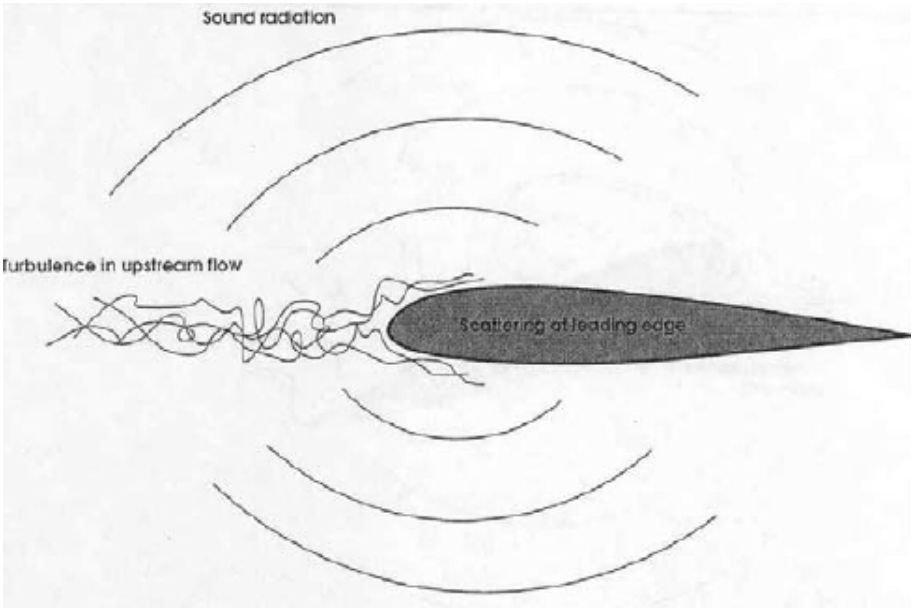

Figure 2.3: Turbulent inflow noise

It is evident that this noise mechanism strongly depends on the characteristics of incident turbulence, such as eddies extension and intensity of the turbulence. In case of wind turbine application this noise source is considered important, especially at low frequencies.

Self-noise generates from interaction of the solid airfoil with its boundary layer and near wake, it is then "self-produced" by the blade. Main sources of self noise

are reported herein, taken from the work of *Brooks, Pope and Marcolini:*

- **TBL-TE, Turbulent boundary layer - trailing edge noise** is considered as a major source of airfoil self-noise. It generates from interaction between a turbulent boundary layer and a trailing edge. Turbulent boundary layers are composed by eddies of various sizes, and their convection over the trailing edge causes propagation of pressure fluctuations to the wake and then to the far field.

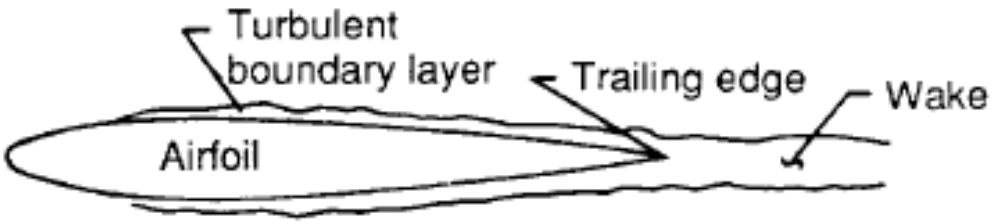

Figure 2.4: Turbulent boundary layer - trailing edge noise

Due to the random nature of turbulence, noise spectra due to this source is usually broadband and its contribution must be computed on both pressure and suction side.

- **Separation - Stall noise** generates when a high angle of attack on the airfoil produces wide areas of separation on the suction side of the profile, that sheds vorticity and then broadband noise to the far field.

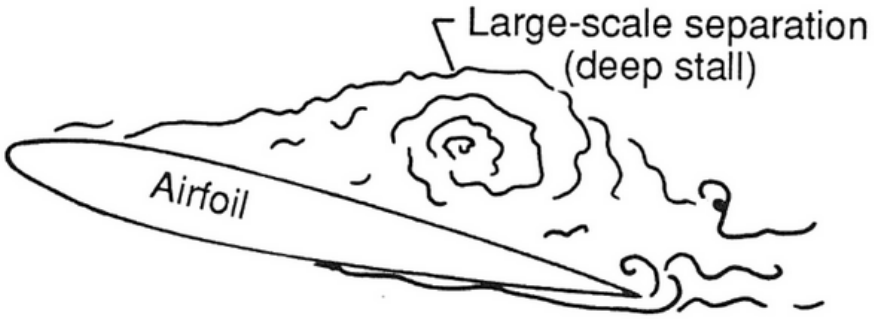

Figure 2.5: Stall Noise

Stall noise knowledge is very limited and no predictive method has yet been developed, but this source could be potentially important for stall-regulated wind turbines.

- **LBL-VS, Laminar boundary layer - vortex shedding noise** generates when boundary layer on suction or pressure side remains laminar for most of the surface of the blade, which occurs if the Reynolds number remains in a range from 10^5 to 10^6. Acoustically excited feedback loops between the trailing edge and Tollmien-Schlichting waves may cause vortex shedding, usually distributed on a narrow band of frequencies.

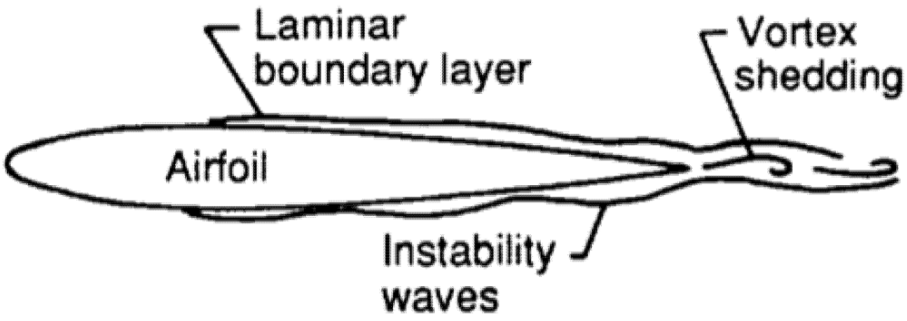

Figure 2.6: Laminar boundary layer - vortex shedding noise

LBL-VS is not considered as an important noise sources for wind turbine, due to the high operation Reynolds number that cause very limited extension of laminar boundary layer.

- **TEB-VS, Trailing edge bluntness - vortex shedding noise** is generated by vortex shedding due to the presence of a thick trailing edge. Noise levels strongly depend on the shape of the trailing edge and the ratio between trailing edge thickness and displacement thickness.

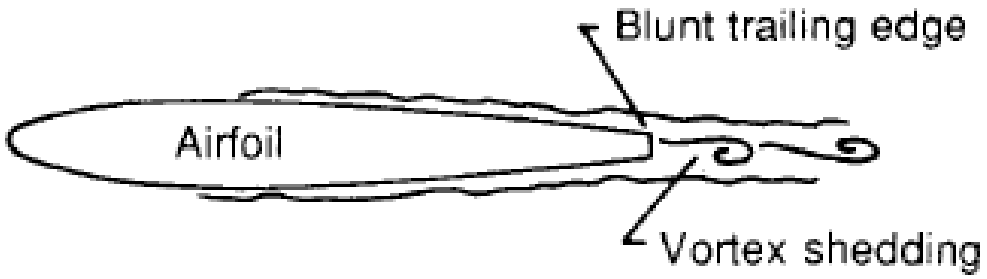

Figure 2.7: Trailing edge bluntness - vortex shedding noise

Trailing edge bluntness is usually tonal, and its contribution can be important for wind turbine application and can be reduced by accurate design of trailing edge angle and thickness.

- **Tip vortex formation noise** is caused by the three-dimensionality of the flow around the tip of the blade. Differences in pressure among suction and pressure side causes the formation of a rotational area that shed noise to the far field. Tip noise strongly depends on geometry details of the blade tip, and was an important source of noise for old wind turbines with thick and squared tips.

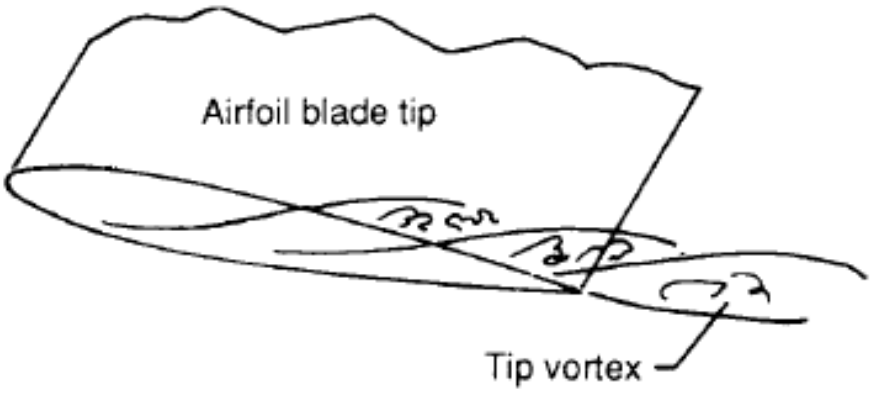

Figure 2.8: Tip vortex formation noise

For modern wind turbines, tip noise is not considered as an important source of aerodynamic noise.

Chapter 3

Modeling of noise sources

The present chapter reports a detailed explanation of all the noise source models implemented. In wind turbine applications the main sources contributing to overall sound levels are turbulent boundary layer - trailing edge noise and turbulent inflow noise. Those sources of aerodynamic noise are broadband by nature and must be taken into account in a noise prediction tool. The chapter starts with description of TNO model, a sophisticated method for TBL-TE noise prediction. Latest improvement of the model allows to take into account anisotropy of boundary layer at the trailing edge, as will be described. *Brooks, Pope, Marcolini* modeling of TBL-TE noise has been included in the present tool, being the most used model in the literature. Turbulent inflow noise modeling follows the approach given by *Amiet* and *Lowson*, where pressure fluctuations due to incident turbulence are related to far field sound pressure level. Thickness corrections due to *Moriarty and Guidati* is also discussed, as well as turbulent length considerations.

3.1 Turbulent boundary layer, trailing edge noise

3.1.1 TNO model

The first model implemented for the computation of the noise due to a turbulent boundary layer at the trailing edge is the so-called TNO. This model was developed by *Parchen* [21] following theoretical studies of *Blake* [31], who derived an expression for the surface pressure fluctuations spectrum using a detailed description of the turbulent boundary layer; this spectrum is then related to the power spectral density

of the far field noise, as reported by *Howe* [10], who unified theories from *Chase* [32] and *Chandiramani* [33]. Contribution to far field noise must be computed for both suction side and pressure side of the profile.

The expression for the surface pressure fluctuations is the following:

$$P(k_1,k_3,\omega) = 4\rho_0^2 \frac{k_1^2}{k_1^2+k_3^2} \int_0^\delta L_2(x_2)\overline{u_2^2}\left(\frac{\partial U_1}{\partial x_2}\right)^2 \phi_{22}(k_1,k_3,\omega) \times \phi_m(\omega - U_c(x_2)k_1)e^{(-2|\vec{k}|y_2)}dx_2 \quad (3.1)$$

Where index $1,2,3$ represent respectively the directions: perpendicular to the trailing edge and directed as the mean flow U, normal to the surface of the profile, parallel to the trailing edge, as reported in Fig 3.1.

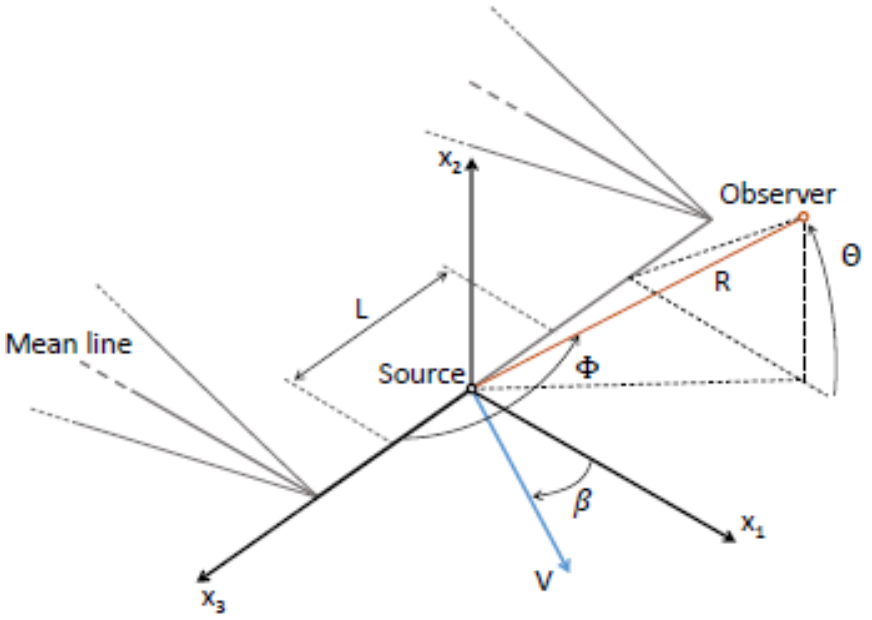

Figure 3.1: Reference frame and observer angles for TNO model

The terms present in equation 3.1 are the following:

ρ_0: Air density

k_1, k_3: Components in direction 1 and 3 of tridimensional wavenumber vector $\vec{k}$

ω: Pulsation $2\pi f$, defined depending on the frequency discretization

δ: Boundary layer thickness

L_2: Integral length that indicates the vertical extension of the vortices that convect over the trailing edge

$\overline{u_2^2}$: *Vertical velocity Reynold stress component* (proportional to turbulent kinetic energy k_t)

U_1: Mean velocity in the boundary layer, its derivative represents the mean shear across the BL.

ϕ_{22}: Component of velocity fluctuations spectrum in the vertical direction.

ϕ_m: *Moving axis spectrum*, it describes how ϕ_{22} is distorted by generation and destruction of eddies during their convection along the trailing edge

U_c: Convection velocity of eddies

$|\vec{k}|$: Norm of the wavenumber vector $\vec{k} = (k_1, 0, k_3)$

The method then requires a quite detailed knowledge of the turbulent boundary layer, all the terms previously mentioned are evaluated at the trailing edge and **must be modeled**. In order to do so, two approaches are generally followed in the literature:

- **CFD analysis**, typically incompressible RANS simulation to solve the 2d Navier-Stokes equations with $k - \epsilon$ or $k - \omega$ turbulence model.
- **A 2d panel method** with boundary layer solver, such as Xfoil.

CFD methods are usually more accurate but pay the price of a higher computational cost, while panel methods are normally much faster. For the present work, the software Xfoil [34] have been used to obtain the boundary layer data. This approach has already been followed by *Moriarty et al* (NREL) [25] and more recently by *Bertagnolio et al* (DTU) [9] [35].

A number of input that must be provided from the aeroelastic simulations are required by Xfoil, reported in Tab 3.1; as output, the code calculates many parameters that can be used to determine the quantities of interest in the boundary layer, which are computed only at the trailing edge. Those data are presented in Tab 3.2.

Parameter	**Symbol**
Profile geometry	-
Angle of attack	α
Reynolds Number	$Re = \frac{\rho_0 C U_{inf}}{\nu}$
Mach Number	$Ma = U_{inf}/c_0$

Table 3.1: Xfoil data input

Parameter	**Symbol**
Velocity at the outer edge of the BL	U_0
Friction coefficient	C_f
Pressure coefficient	Cp
Shape factor	Hk
Displacement thickness	δ^*
Momentum displacement thickness	θ

Table 3.2: Output required from Xfoil

First of all, displacement thickness and momentum thickness are used to obtain an expression of the boundary layer thickness, through the relation given by M.Drela:

$$\delta = C(\theta\left(3.15 + \frac{1.72}{H_k - 1}\right) + \delta^*) \tag{3.2}$$

The term C indicates the chord of the considered wing section, this term is needed because θ and δ^* from Xfoil are given based on unitary chord.

Dimensional velocity at the outer edge of the boundary layer is obtained from:

$$U_0^{dim} = U_{inf} U_0 \tag{3.3}$$

Which allows computation of the friction velocity as:

$$U^* = U_0^{dim} \sqrt{\frac{C_f}{2}} \tag{3.4}$$

By making use of the quantities just derived, all remaining terms of Eq.3.1 can be calculated.

To model the speed $U_1(x_2)$ in the boundary layer the Cole's law of the wall/ of the wake is used. Through this relation it is possible to relate the average speed to parameters such as friction velocity, viscosity, boundary layer thickness and other constants:

$$U_1(x_2) = U^* \left(\frac{1}{K} \log \left(\frac{U^* x_2}{\nu} \right) \right) + B + \frac{1}{2} \left(1 - \cos \left(\frac{\pi x_2}{\delta} \right) \right) \left(\frac{U_0^{dim}}{U^*} - \frac{1}{K} \log \left(\frac{U^* \delta}{\nu} - B \right) \right) \tag{3.5}$$

According to eq.3.5, the term $\partial U_1 / \partial x_2$ present in eq.3.1 can be obtained by direct differentiation:

$$\frac{\partial U_1}{\partial x_2} = \frac{U^*}{K x_2} + \frac{1}{2} U^* \sin \left(\frac{\pi x_2}{\delta} \right) \frac{\pi}{\delta} \left(\frac{U_0^{dim}}{U^*} - \frac{1}{K} \log \left(\frac{U^* \delta}{\nu} \right) - B \right) \tag{3.6}$$

Where $K = 0.41$ is the Prandtl constant and $B = 5.5$ is a correction factor.

A first possible problem of the model now emerges: the case of negative friction coefficient (which is typical of separations) cannot be considered by the TNO; in such cases C_f is set to a very small value ($C_f = 0.0001$).

It is now modelled the integral length L_2; there are many ways to define this parameter and the approach used in the present work makes use of the mixing length that, based upon Prandtl theory, is proportional to distance from the wall for values of x_2 close enough to the wall.

$$L_m = kx_2 \qquad\qquad x_2 \to 0 \tag{3.7}$$

However it is generally accepted the fact that mixing length doesn't increase linearly across the whole boundary layer. For this reason the expression of *Schlichting* [36] is used, which states that L_m reaches its maximum value around 0.085δ

$$L_m = 0.085\delta \tanh\left(\frac{Kx_2}{0.085\delta}\right) \tag{3.8}$$

At this point it's possible to estimate the integral length L_2; two are the approaches found in the literature, the first followed by the *NREL* [25]:

$$L_2(x_2) = c_1\delta x_2\left(1 - e^{-(c_2(1-\frac{x_2}{\delta})^3)}\right) \tag{3.9}$$

With $c_1 \sim 2-4$ and $c_2 \sim 0.5-1.5$ empirical constants. A second approach is the one followed by *DTU* [9], that used the following expression for the integral length:

$$L_2(x_2) = \frac{L_m}{K} \tag{3.10}$$

The following parameter to be modelled is the vertical velocity Reynolds stress component $\overline{u_2^2}$; again different authors make use of different formulas to estimate this parameter, both ways relying on the determination of the *turbulent viscosity*:

$$\nu_t = l_m^2\left|\frac{\partial U_1}{\partial x_2}\right| \tag{3.11}$$

NREL approach computes $\overline{u_2^2}$ as:

$$\overline{u_1 u_2} = \nu_t \frac{\partial U_1}{\partial x_2} \tag{3.12}$$

$$\overline{u_2^2}(x_2) = \frac{\overline{u_1 u_2}}{c_3} = \frac{l_m^2}{c_3}\frac{\partial U_1}{\partial x_2}\left|\frac{\partial U_1}{\partial x_2}\right| \tag{3.13}$$

With $c_3 \sim 0.3-0.6$

Different is the approach followed by *DTU*, that makes use of the turbulent

kinetic energy in the boundary layer, calculated through:

$$k_t = \sqrt{\nu_t \frac{\left(\frac{\partial U_1}{\partial x_2}\right)^2}{C_\mu}}, \qquad C_\mu = 0.09 \tag{3.14}$$

Vertical component of the Reynolds stress tensor is evaluated as proportional to the turbulent kinetic energy

$$\overline{u_2^2}(x_2) = \alpha k_t, \quad \alpha = \begin{cases} 0.45 \text{ Suction side} \\ 0.3 \text{ Pressure side} \end{cases} \tag{3.15}$$

In the present work, computation of noise spectra from TNO model will follow the approach of *DTU* (Eq 3.10 and 3.15).

Convection velocity U_c is computed simply as 70% of the mean velocity in the boundary layer

$$U_c(x_2) = 0.7U_1(x_2) \tag{3.16}$$

In order to evaluate the spectrum of velocity fluctuations in vertical direction ϕ_{22}, an estimation of the wavenumber of energy-containing eddies k_e is needed; such estimate is made possible by the assumption of isotropic turbulence:

$$k_e = \frac{\sqrt{\pi}\Gamma(\frac{5}{6})}{\Gamma(\frac{1}{3})L_2} \sim \frac{0.7468342...}{L_2} \tag{3.17}$$

k_e is then related to the vertical length L_2 and the gamma function $\Gamma(x)$:

$$\Gamma(x) = \int_0^\infty e^{-t}t^{x-1}dt \tag{3.18}$$

The vertical velocity spectrum ϕ_{22} is computed as:

$$\phi_{22}(k_1, k_3, k_e) = \frac{4}{9\pi k_e^2} \frac{\hat{k}_1^2 + \hat{k}_3^2}{(\hat{k}_1^2 + \hat{k}_3^2 + 1)^{\frac{7}{3}}} \tag{3.19}$$

Where the components of the wavenumber vector k_i are adimensionalized with k_e:

$$\hat{k}_i(\omega, y_2) = \frac{k_i}{k_e} \qquad\qquad i = 1, 3 \tag{3.20}$$

The last quantity to be computed is the *moving axis spectrum* ϕ_m, modeled as a gaussian distribution:

$$\phi_m(k_1, \omega, x_2) = \frac{1}{\alpha_G\sqrt{\pi}} e^{-((\omega - U_c k_1)/\alpha_G)^2} \tag{3.21}$$

Where:

$$\alpha_G = 0.05\frac{U_c}{L_2} \tag{3.22}$$

The absolute value of the wave number directional array is then defined as:

$$|\vec{k}| = \sqrt{k_1^2 + k_2^2} \tag{3.23}$$

with k_1 and k_3 computed with respect of ω and the relative position between source and observer:

$$k_1(\omega, x_2) = \frac{\omega}{U_c(x_2)} \qquad\qquad k_3(\omega, \vec{r}) = \frac{\omega}{c}\cos(\Phi) \tag{3.24}$$

More recently, studies conducted by *Bertagnolio et al* [37] brought to a new formulation of the velocity spectrum and the integral length, that takes into account anisotropy of the turbulent boundary layer; the new ϕ_{22} has the following representation:

$$\phi_{22}(k_1, k_3, \Lambda) = \frac{4\Lambda^2\beta_1\beta_3}{9\pi} \frac{(\beta_1\Lambda k_1)^2 + (\beta_3\Lambda k_3)^2}{((\beta_1\Lambda k_1)^2 + (\beta_3\Lambda k_3)^2 + 1)^{\frac{7}{3}}} \tag{3.25}$$

Where:

$$\Lambda(x_2) = \frac{L_m}{0.7468K} \tag{3.26}$$

The spectrum now is not isotropic anymore, but depends directionally on the values of coefficients $\beta_{1,2,3}$. A new definition of the integral length L_2 is given; it is

interesting to note that now this length shows a dependency on the frequency ω.

$$L_2(\omega) = \frac{55\Gamma(1/3)}{108\sqrt{\pi}\Gamma(17/6)}\Lambda\beta_2\frac{3+11(\beta_1\Lambda k_1)^2}{3+8(\beta_1\Lambda k_1)^2}\frac{1}{\sqrt{1+(\beta_1\Lambda k_1)^2}} \tag{3.27}$$

It is clear that the model strongly relies on the determination of coefficients $\beta_1, \beta_2, \beta_3$, which are to be determined sperimentally. The tuning of such parameters have been performed by Bertagnolio using a *NACA0015*, and the results are reported as follows:

$$\beta_1 = 0.4 \tag{3.28}$$

$$\beta_2 = \gamma^{1/5} \tag{3.29}$$

$$\beta_3 = (2\gamma)^{1/2} \tag{3.30}$$

With:

$$\gamma(y_2) = \frac{\delta}{U^*}\left(\frac{1}{\rho^2\nu}\left(\frac{\partial P}{\partial x_1}\right)^2\right)^{1/3} \tag{3.31}$$

$\partial P/\partial x_1$ represents the pressure gradient in direction 1, evaluated at the trailing edge.

The difference among the "isotropic" and "anisotropic" TNO is little when symmetrical profiles are used at low angles of attack, while it rapidly increases for asymmetrical profiles at high angle of attack.

Once the pressure fluctuation spectrum $P(k_1, k_3, \omega)$ is known, it is possible to relate it to the power spectral density of the far field noise $S(\omega)$ that, for a general observer placed in the space, can be calculated as:

$$S_{pp}(\omega) = \frac{L}{2\pi R^2}D\int_{-\infty}^{+\infty}\frac{\omega}{c_0|\vec{k}\cdot\vec{n}|}\frac{P(k_1,k_3,\omega)}{(1-M_{v,R})^2(1-M_{v,1}\sin\Phi)}dk_1 \tag{3.32}$$

In the above formula L indicates the span of the wing section, R is the distance from the mid-span point of the trailing edge (which represent the source point of the trailing edge noise models) to the observer, c_0 is the speed of sound and the term $|\vec{k}\cdot\vec{n}|$ indicates the dot product between the wavenumber vector $\vec{k} = (k_1, 0, k_3)^T$, the versor $\vec{n}$, parallel to the mean eddy convection velocity, $M_{v,R}$ and $M_{v,1}$ are the component of eddy convection Mach number projected in the observer direction and along the chord, respectively. The term D is the directivity factor of the sound.

Directivity takes into account the fact that strength of the noise varies depending on the direction from the sound source, therefore it depends on the relative position between source-observer and generally on noise frequency. For trailing edge noise, a possible expressions of directivity is due to Howe [10]:

$$D = \frac{\sin\Phi \sin^2\frac{\Theta}{2}\cos\beta}{(1+M_{0,R})^2(1-M_{W,R})^2} \tag{3.33}$$

The angles Φ, Θ and β are shown in Fig. 3.1 and are calculated accordingly to Tab. 3.3. the term $M_{O,R}$ represents the far field flow Mach number and $M_{W,R}$ is the wake convection Mach number, both projected on the direction of the observer. In order to estimate $M_{O,R}$ and $M_{W,R}$ however, it is necessary to introduce some additional hypothesis, linked to the lack of information provided by the aeroelastic simulation:

- $\underline{M_0}$ is evaluated at the airstation as $\underline{M_0} = \underline{V}/c_0$
- $\underline{M_W}$ is computed as the mean speed in the boundary layer:

$$\underline{M_W} = \underline{M_0}\frac{\int_0^\delta U_1 dx_2}{U_{inf}\delta} \tag{3.34}$$

  $\int_0^\delta U_1 dx_2$ can be computed analytically from 3.5:

$$\int_0^\delta U_1 dx_2 = U^*\delta\left(\frac{1}{K}\left(\log\left(\frac{U^*\delta}{\nu}\right)-1\right)+B+\frac{1}{2}\left(\frac{U_0^{dim}}{U^*}-\frac{1}{K}\log\left(\frac{U^*\delta}{\nu}\right)-B\right)\right) \tag{3.35}$$

- Eddy convection Mach number is the wind speed at the outer edge of the boundary layer:

$$\underline{M_v} = \underline{V}U_0/c_0 \tag{3.36}$$

Another directivity used in the present work is taken from *Bertagnolio et Al* [38]:

$$D = \frac{2\sin^2\frac{\Theta}{2}\sin^2\Phi}{(1+M_r\cos\Theta_c)^3} \tag{3.37}$$

It must be noted that the angles Φ and Θ **are not** the same of eq. 3.33 but are taken from work of *Brooks, Pope and Marcolini* [39] as explained in section 3.1.2.

Parameter	Formula
$\underline{R}$	$(x_1, x_2, x_3)^T$
R	$\lvert\underline{R}\rvert$
$\cos\Phi$	$\frac{x_3}{R}$
$\sin\Phi$	$\sqrt{1-\cos^2\Phi}$
$\sin\Theta$	$\frac{x_2}{R\sin\Phi}$
$\sin\Theta$	$\frac{x_1}{R\sin\Phi}$
$\sin^2\frac{\Theta}{2}$	$\frac{1-\cos\Theta}{2}$

Table 3.3: Directivity angles computation for TNO

In case of observer placed directly above the trailing edge, $\Theta = \Phi = 90°$ and equation 3.32 simplifies to (see [40]):

$$S(\omega) = \frac{L}{4\pi R^2}\int_{-\infty}^{+\infty}\frac{\omega}{c_0 k_1}P(k_1, k_3 = 0, \omega)dk_1 \tag{3.38}$$

Numerically speaking, the integral to be solved for determination of trailing edge noise spectrum is the following, obtained combining eq 3.32 and 3.1:

$$S_{pp}(\omega) = \frac{L}{2\pi R^2}D\int_{-\infty}^{+\infty}\int_0^{\delta}4\rho_0^2\frac{k_1^2}{k_1^2+k_3^2}\frac{\omega}{c_0|\vec{k}\cdot\vec{n}|}\frac{1}{(1-M_{v,R})^2(1-M_{v,1}\sin\Phi)}$$
$$L_2(x_2)\overline{u_2^2}\left(\frac{\partial U_1}{\partial x_2}\right)^2\phi_{22}(k_1, k_3, \omega)\times\phi_m(\omega - U_c(x_2)k_1)e^{(-2|\vec{k}|y_2)}dx_2dk_1 \tag{3.39}$$

It is possible to avoid the computation of the integral on k_1 by exploiting the sampling effect of the moving axis spectrum, treating ϕ_m as a Dirac's delta:

$$\int_{-\infty}^{+\infty}f(x)\delta(g(x)) = \sum_i\frac{f(x_i)}{|g'(x_i)|} \tag{3.40}$$

Where x_i are the zeros of the function $g(x)$. For $\phi_m(\omega - k_1U_c)$, it means to evaluate the integrand in $k_1 = \omega/U_c$ and multiplying it by $1/|U_c|$.

It is finally worth to mention that even for a quite sophisticated model such as the TNO just described in details, accuracy of the results strongly depend on many factors such as constants, modeling, hypothesis, aeroelastic input and boundary layer data. Validation and discussion of the results will be discussed in chapter 5

3.1.2 Brooks, Pope, Marcolini TBL-TE

Another model implemented to predict turbulent boundary layer trailing edge noise is the one developed by *Brooks, Pope and Marcolini*(BPM) [39]: in their work, the authors developed a method to compute the contribution of noise from various noise, based on the fitting of experimental results obtained on many $NACA0012$ (with different chord size) at various speed and angle of attack.

During the experiments, in order to assure the transition from laminar to turbulent boundary layer, all the profiles were "heavily tripped" with grit in strips from leading edge to 20% of the chord: the boundary layer thickness was then measured for this profile on pressure and suction side at varying angles of attack and used as input of the model.

The input required to the TBL-TE routine of BPM are presented in Tab.3.4:

Parameter	**Symbol**
Displacement thickness	δ^*
Mach number	M
Span	L
High frequency directivity	D_h
Distance source-observer	R

Table 3.4: Input of the BPM model

Due to the fact that boundary layer thickness is computed from experimental fitting, one of the problem of the BPM is that it tends to give similar results even for profiles very different from a *NACA0012*. This problem can be overcome by

using Xfoil to compute the boundary layer thickness, allowing to give as input the real geometry of the blade that in case of wind turbine application is usually much different from that of a *NACA0012*.

The BPM directly gives results in SPL in 1/3 octave band discretization. For the case of turbulent boundary layer trailing edge noise, this contribution is constituted by the sum of 3 terms:

$$SPL_{TOT} = 10\log(10^{SPL_\alpha/10} + 10^{SPL_p/10} + 10^{SPL_s/10}) \tag{3.41}$$

Where:

$$SPL_p = 10\log(\frac{\delta_p^* M^5 L D_h}{R^2}) + A(\frac{St_p}{St_1}) + (K_1 - 3) + \Delta K_1 \tag{3.42}$$

$$SPL_s = 10\log(\frac{\delta_s^* M^5 L D_h}{R^2}) + A(\frac{St_s}{St_1}) + (K_1 - 3) \tag{3.43}$$

$$SPL_\alpha = 10\log(\frac{\delta_s^* M^5 L D_h}{R^2}) + B(\frac{St_s}{St_1}) + K_2 \tag{3.44}$$

Contribution SPL_p, SPL_s, SPL_α are respectively due to pressure side, suction side and angle of attack. For angles of attack above 12.5° (where the profile is considered stalled):

$$SPL_p = -\infty \tag{3.45}$$

$$SPL_s = -\infty \tag{3.46}$$

$$SPL_\alpha = 10\log(\frac{\delta_s^* M^5 L D_l}{R^2}) + A'(\frac{St_s}{St_2}) + K_2 \tag{3.47}$$

A' is the same curve A but evaluated at a Reynolds number 3 times larger. Strouhal numbers St are defined as:

$$St_p = \frac{f\delta_p^*}{U} \qquad St_s = \frac{f\delta_s^*}{U} \tag{3.48}$$

$$St_1 = 0.02M^{-0.6} \tag{3.49}$$

$$\overline{St}_1 = \frac{St_1 + St_2}{2} \tag{3.50}$$

The value of St_2 is then calculated through:

$$St_2 = St_1 \times \begin{cases} 1 & \alpha < 1.33° \\ 10^{0.0054(\alpha - 1.33)^2} & 1.33° \leq \alpha \leq 12.5 \\ 4.72 & 12.5° < \alpha \end{cases} \tag{3.51}$$

The spectrum function A is now computed:

$$A(a) = A_{min}(a) + A_R(a_0)[A_{max(a)} - A_{min}(a)] \tag{3.52}$$

With:

$$a = |\log(St/St_{peak})| \tag{3.53}$$

St can be either St_p or St_s, while $St_{peak} = St_1, \overline{St}_1$ or St_2, and:

$$A_{min}(a) = \begin{cases} \sqrt{67.552 - 886.788a^2} - 8.219 & a < 0.204 \\ -32.665a + 3.981 & 0.204 \leq a \leq 0.244 \\ -142.795a^3 + 103.656a^2 - 57.757a + 6.006 & 0.244 < a \end{cases} \tag{3.54}$$

$$A_{max}(a) = \begin{cases} \sqrt{67.552 - 886.788a^2} - 8.219 & a < 0.13 \\ -15.901a + 1.098 & 0.13 \leq a \leq 0.321 \\ -4.669a^3 + 3.491a^2 - 16.699a + 1.149 & 0.321 < a \end{cases} \tag{3.55}$$

$a_0(R_c)$ is given as a function of the Reynolds number R_c:

$$a_0(R_c) = \begin{cases} 0.57 & R_c < 9.52 \times 10^4 \\ (-9.57 \times 10^{-13})(R_c - 8.57 \times 10^5)^2 + 1.13 & 9.52 \times 10^4 \leq R_c \leq 8.57 \times 10^5 \\ 1.13 & 8.57 \times 10^5 < R_c \end{cases} \tag{3.56}$$

The last term to compute is the interpolation factor:

$$A_R(a_0) = \frac{-20 - A_{min}(a_0)}{A_{max}(a) - A_{min}(a)} \tag{3.57}$$

Evaluation of function B is performed in a manner similar to function A:

$$B(a) = B_{min}(a) + B_R(b_0)[B_{max(b)} - B_{min}(b)] \tag{3.58}$$

With:

$$b = |\log(St_s/St_2)| \tag{3.59}$$

$$B_{min}(b) = \begin{cases} \sqrt{16.888 - 886.788b^2} - 4.109 & b < 0.13 \\ 83.607b + 8.138 & 0.13 \leq b \leq 0.145 \\ -817.810b^3 + 355.210b^2 - 135.024b + 10.619 & 0.145 < b \end{cases} \tag{3.60}$$

$$B_{max}(a) = \begin{cases} \sqrt{16.888 - 886.788b^2} - 4.109 & b < 0.10 \\ -31.330b + 1.854 & 0.10 \leq b \leq 0.187 \\ -80.541b^3 + 44.174b^2 - 39.381b + 2.344 & 0.187 < b \end{cases} \tag{3.61}$$

$b_0(R_c)$ is computed as:

$$b_0(R_c) = \begin{cases} 0.30 & R_c < 9.52 \times 10^4 \\ (-4.48 \times 10^{-13})(R_c - 8.57 \times 10^5)^2 + 0.56 & 9.52 \times 10^4 \leq R_c \leq 8.57 \times 10^5 \\ 0.56 & 8.57 \times 10^5 < R_c \end{cases} \tag{3.62}$$

Where:

$$B_R(b_0) = \frac{-20 - B_{min}(b_0)}{B_{max}(b) - B_{min}(b)} \tag{3.63}$$

The last terms to be computed are K_1, ΔK_1 and K_2, those terms are given by:

$$K_1 = \begin{cases} -4.31\log(R_c) + 156.3 & R_c < 2.47 \times 10^5 \\ -9.0\log(R_c) + 181.6 & 2.47 \times 10^5 \leq R_c \leq 8.0 \times 10^5 \\ 128.5 & 8.0 \times 10^5 < R_c \end{cases} \tag{3.64}$$

$$\Delta K_1 = \begin{cases} \alpha^*[1.43\log(R_{\delta_p^*}) - 5.29] & R_{\delta_p^*} \leq 5000 \\ 0 & 5000 < R_{\delta_p^*} \end{cases} \tag{3.65}$$

$$K_2 = K_1 + \begin{cases} -1000 & \alpha^* \leq \gamma_0 - \gamma \\ \sqrt{\beta^2 - (\beta/\gamma)^2(\alpha^* - \gamma_0)^2} + \beta_0 & \gamma_0 - \gamma \leq \alpha^* \leq \gamma_0 + \gamma \\ -12 & \gamma_0 + \gamma < \alpha^* \end{cases} \tag{3.66}$$

Where:

$$\begin{cases} \gamma = 27.094M + 3.31 \\ \gamma_0 = 23.43M + 4.651 \\ \beta = 72.65M + 10.74 \\ \beta_0 = -34.19M - 13.82 \end{cases} \tag{3.67}$$

$R_{\delta_p^*}$ is the Reynolds number based on pressure side displacement thickness.

From what shown above, it is clear that the model is entirely obtained from empirical relations, making it much "less physical" than the TNO model described in the previous section.

Two are the directivity factors used in the BPM model, $\overline{D}_l$ and $\overline{D}_h$, defined respectively for low and high frequency:

$$\overline{D}_l(\Theta_e, \Phi_e) = \frac{\sin^2\Theta_e \sin^2\Phi_e}{(1 + M\cos\Theta_e)^4} \tag{3.68}$$

$$\overline{D}_h(\Theta_e, \Phi_e) = \frac{2\sin^2\frac{\Theta_e}{2}\sin^2\Phi}{(1 + M\cos\Theta_e)[1 + (M - M_c)\cos\Theta_e]^2} \tag{3.69}$$

The convection Mach number M_c is defined as $M_c = 0.8M$; the angles Θ_e and Φ_e are

reported in fig 3.2, taken directly from the original work of *Brooks, Pope, Marcolini* [39].

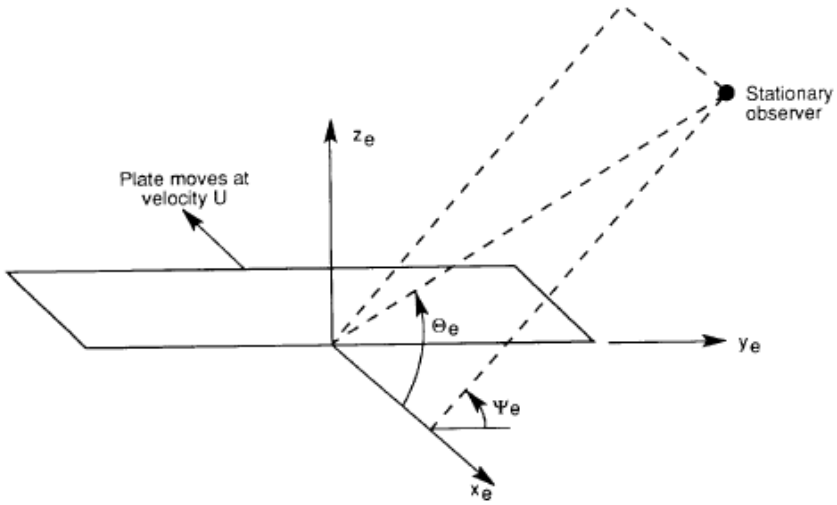

Figure 3.2: Reference frame and observer angle for BPM model

For completeness reason, it is noteworthy to mention the recent work due to *Lau et al* [20] in which two new enhanced versions of BPM are proposed, based on interpolation of many airfoils of common use on wind turbine applications, denominated BPMM-PVII and BPMM-BL$k\omega$. The two models differ in the computation of the boundary layer parameters: panel methods with viscous-inviscid interaction for BPMM-PVII, CFD with $k-\omega$ turbulence model for BPMM-BL$k\omega$.

After a presentation of the model, a comparative study between BPM and TNO is performed, showing quite good agreement.

3.2 Turbulent inflow noise

3.2.1 Amiet model

Modeling of turbulent inflow noise is performed following the work of *Amiet and Paterson*[22][23]. In this work, the authors developed and validated experimentally a model to predict power spectral density of the noise generated by interaction between a turbulent stream with the leading edge of the profile, modeled as a flat plate of span $2d$ and chord $2b$, with no thickness nor angle of attack. Reference system of

the problem is represented in fig. 3.3

In his publication, *Amiet* arrived at the following expression of the far-field power spectral density of the noise:

$$S_{PP}(\underline{x},\omega) = \left(\frac{\omega x_3 \rho_0 b}{c_0 \sigma^2}\right)^2 U_{inf} d\pi \int_{-\infty}^{+\infty} \left[\frac{\sin^2(d(k_2+\omega x_2/c_0\sigma))}{(k_2+\omega x_2/c_0\sigma)^2 \pi d}\right] |\mathcal{L}(\underline{x},K_1,k_2)|^2 \Phi_{ww}(K_1,k_2) dk_2 \quad (3.70)$$

With:

$$\sigma^2 = x_1^2 + \beta^2(x_2^2+x_3^2) \quad (3.71)$$

$$\beta^2 = 1 - M^2 \quad (3.72)$$

$$K_1 = \frac{\omega}{U_{inf}} \quad (3.73)$$

k_1 and k_2 are the axial (chordwise) and lateral (spanwise) wavenumbers of the turbulence, $\underline{x} = (x_1, x_2, x_3)^T$ is the position of the observer with respect to the **mid chord point** of the wing section, in the TI reference frame. Other terms present in 3.70 are $\mathcal{L}(\underline{x}, K_1, k_2)$, defined as the effective lift, and the two-dimensional spectrum $\Phi_{ww}(K_1, k_2)$.

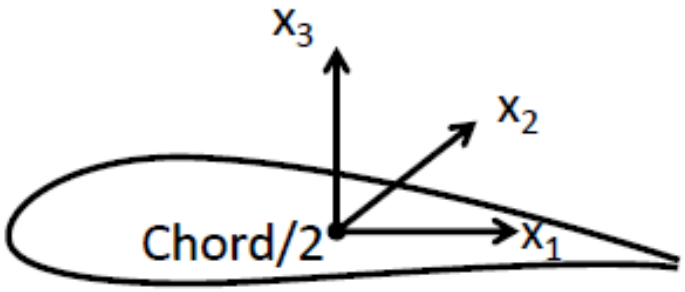

Figure 3.3: Reference frame for Amiet model

Equation 3.70 can be simplified by exploiting the fact that, if the semi-span d

increases, the quantity in square brackets behaves like a Dirac delta:

$$\lim_{d\to+\infty}\left[\frac{\sin^2(\xi d)}{\xi^2\pi d}\right]\to\delta(\xi) \tag{3.74}$$

If the acoustic wavelength λ is much smaller than the airfoil semi-span d, or $MK_1d \gg 1$, equation 3.70 becomes:

$$S_{pp}(\underline{x},\omega)=\left(\frac{\omega x_3\rho_0 b}{c_0\sigma^2}\right)^2\pi U_{inf}d|\mathcal{L}(\underline{x},K_1,K_2)|^2\Phi_{ww}(K_1,K_2) \tag{3.75}$$

$$K_y=\omega x_2/c_0\sigma \tag{3.76}$$

Atmospheric turbulence is considered isotropic, and its Von Karman spectrum is computed as:

$$\Phi_{ww}(k_1,k_2)=\frac{4\overline{u^2}}{9\pi k_e^2}\frac{\hat{k}_1^2+\hat{k}_2^2}{(1+\hat{k}_1^2+\hat{k}_2^2)^{7/3}} \tag{3.77}$$

$\hat{k}_i=k_i/k_e$ and k_e is the wavenumber of the energy containing eddies, that can be expressed as a function of the longitudinal integral length of the turbulence L_t:

$$k_e=\frac{\sqrt{\pi}}{L_t}\frac{\Gamma(5/6)}{\Gamma(1/3)} \tag{3.78}$$

The parameter L_t is a function of the turbulent flow field, and for wind turbine applications is usually given as a function of the height of the source with respect to the ground, as will be explained in section 3.2.3. The term $\overline{u^2}$ indicates the mean square value of the velocity fluctuations normal to the profile, and can be computed from the aeroelastic simulations.

The effective lift $\mathcal{L}$ is given by:

$$\mathcal{L}(\underline{r},K_1,k_2)=\int_{-1}^{+1}g(\xi,K_1,k_2)e^{-i\mu\xi(M-x_1/\sigma)}d\xi \tag{3.79}$$

Where $g(\xi,K_1,k_2)$ is the transfer function between turbulent velocity and air pressure jump. Considering a normal gust of shape

$$w_g=w_0e^{i[k_1(U_{inf}t-x_1)-k_2x_2]} \tag{3.80}$$

The pressure jump across the airfoil is:

$$\Delta P(x_1, x_2, t; K_1, k_2) = 2\pi\rho_0 U_{inf} w_0 g(\xi, K_1, k_2) e^{i[k_1 U_{inf} t - k_2 x_2]} \tag{3.81}$$

The adimensional pressure jump g is obtained through approximation, one for the low frequency regime and another for the high frequency; the parameter governing whether the regime is "high frequency" or "low frequency" is the following:

$$\mu = M K_x b/\beta^2 \tag{3.82}$$

- if $\mu < 0.4$:

$$g(\xi, k_x, 0) = \frac{1}{\pi\beta}\sqrt{\frac{1-\xi}{1+\xi}} S(k_1^*) \exp\left(i\overline{k}_1^*(M^2\xi + f(M))\right) \tag{3.83}$$

  Where $-1 < \xi < 1$ is the integration variable, S is the Sears function, $k_1^* = k_1/\beta^2$, $\overline{k}_1^* = k_1^* b$ and $f(M)$ is equal to:

$$f(M) = (1-\beta)\ln M + \beta\ln(1+\beta) - \ln 2 \tag{3.84}$$

- if $\mu > 0.4$, Adamczyk solution is used, composed by two terms:

$$g_1(\xi, k_1, 0) = \frac{1}{\pi\sqrt{\pi(1+M)\overline{k}_1(1+\xi)}} \exp\left(-i\left(\mu(1-M)(1+\xi) + \frac{\pi}{4} - \overline{k}_1\right)\right) \tag{3.85}$$

$$g_2(\xi, k_1, 0) = \frac{1}{\pi\sqrt{2\pi(1+M)\overline{k}_1}} \exp\left(-i\left(\mu(1-M)(1+\xi) + \frac{\pi}{4} - \overline{k}_1\right)\right) \left[(1+i)E^*(2\mu(1-\xi)) - 1\right] \tag{3.86}$$

$$g = g_1 + g_2 \tag{3.87}$$

And $E*(x)$ is a combination of Fresnel integrals:

$$E^*(x) = \frac{1}{\sqrt{2\pi}} \int_0^x e^{-i\xi} \frac{d\xi}{\sqrt{\xi}} \tag{3.88}$$

All the g functions given above are referred to the case with an observer placed in the plane $x_2 = 0$, i.e., $k_2 = 0$. The general case of skewed compressible gust may be obtained by making use of the *Graham's similarity rules* [41]; this technique allow to retrieve the skewed compressible gust function g from the equation of a parallel compressible gust and a skewed incompressibile gust. Similarity rules must be applied to the following function, resulting from integration of eq. 3.81 in the wavenumbers domain and applying the fourier trasform:

$$g(\overline{x}_1, \overline{K}_1, \overline{k}_2) e^{-k_2 x_2} \tag{3.89}$$

The two cases mentioned are distinguished by the parameter θ:

$$\theta = \frac{\overline{K}_1 M}{\overline{K}_2 \beta} \qquad \overline{K}_i = K_i b \tag{3.90}$$

And the similarity rules for the two cases are:

- Subcritical flows $\theta \leq 1$

  In this case each term of the group is similar to an incompressible oblique problem, so $M_0 = 0$ and upwash $\omega_0 = e^{i(\omega t - k_1 x_1 - k_2 x_2)}$, members of this group are identified by the subscript $_0$:

$$M_0 = 0 \tag{3.91}$$

$$\overline{k}_{1,0} = \frac{\overline{k}_1}{\beta^2} \tag{3.92}$$

$$\overline{k}_{2,0} = \frac{\overline{k}_1}{\beta} (1 - \theta^2)^{1/2} \tag{3.93}$$

The loading coefficients per unit upwash are related by:

$$c_{\Delta P}(M,\overline{k}_1,\overline{k}_2) = g_0(\overline{k}_{1,0},\overline{k}_{2,0})\exp\left(-i\frac{\overline{k}_2}{\beta}(1-\theta^2)^{1/2}\overline{x}_2\right) \exp\left(i\left(\overline{k}_1\frac{M^2}{\beta^2}\overline{x}_1+\overline{k}_2\left(\frac{(1-\theta^2)}{\beta}-1\right)\overline{x}_2\right)\right)\frac{1}{\beta} \quad (3.94)$$

$$= g_0(\overline{k}_{1,0},\overline{k}_{2,0})\exp\left(i\left(\overline{k}_1\frac{M^2}{\beta^2}\overline{x}_1\right)\right)\frac{1}{\beta}\exp\left(-i\overline{k}_2\overline{x}_2\right) \quad (3.95)$$

And the g function to be implemented is:

$$g(x,\overline{k}_1,\overline{k}_2) = g_0(\overline{k}_{1,0},\overline{k}_{2,0})\exp\left(i\left(\overline{k}_1\frac{M^2}{\beta^2}\overline{x}_1\right)\right)\frac{1}{\beta} \quad (3.96)$$

- Supercritical flows $\theta > 1$

  Each term of this group is similar to a compressible two-dimensional problem, i.e., $M_\infty \neq 0$, $\omega_\infty = \exp(i(\omega t - k_1 x_1))$ and the members of the group are subscripted by the term $_\infty$:

$$M_\infty = M\left(1-\frac{1}{\theta^2}\right)^{1/2} \quad (3.97)$$

$$\overline{k}_{1,\infty} = \overline{k}_1\left(1+\left(\frac{\overline{k}_2}{\overline{k}_1}\right)^2\right) \quad (3.98)$$

$$\overline{k}_{2,\infty} = 0 \quad (3.99)$$

  The loading coefficients are related as:

$$c_{\Delta P}(M,\overline{k}_1,\overline{k}_2) = g_\infty(M_\infty,\overline{k}_{1,\infty})\left(1+\left(\frac{\overline{k}_2}{\overline{k}_1}\right)^2\right)^{1/2} \exp\left(i\overline{k}_2\left(\frac{\overline{k}_2}{\overline{k}_1}\overline{x}_1-\overline{x}_2\right)\right) \quad (3.100)$$

$$= g_\infty(M_\infty,\overline{k}_{1,\infty})\left(1+\left(\frac{\overline{k}_2}{\overline{k}_1}\right)^2\right)^{1/2}\exp\left(i\overline{k}_2\left(\frac{\overline{k}_2}{\overline{k}_1}\overline{x}_1\right)\right)\exp(-i\overline{k}_2\overline{x}_2) \quad (3.101)$$

With g function:

$$g(x, M, \overline{k}_1, \overline{k}_2) = g_\infty(M_\infty, \overline{k}_{1,\infty})\left(1 + \left(\frac{\overline{k}_2}{\overline{k}_1}\right)^2\right)^{1/2} \exp\left(i\overline{k}_2\left(\frac{\overline{k}_2}{\overline{k}_1}\overline{x}_1\right)\right) \quad (3.102)$$

In case of $\theta = 1$, both expressions converge to the same g function. It is finally interesting to note the fact that, given $K_1 = \omega/U_{inf}$ and $K_2 = \omega x_2/c_0\sigma$, the parameter θ is always greater than one, if source and observer are not coincident:

$$\theta = \frac{\overline{K}_1 M}{\overline{K}_2 \beta} = \frac{\omega}{U_{inf}} \frac{c_0\sigma}{\omega x_2} \frac{M}{\beta} = \frac{\sigma}{\beta} = \frac{\sqrt{x_1^2 + \beta^2(x_2^2 + x_3^2)}}{\beta} \quad (3.103)$$

Nevertheless, for the sake of completeness, both subcritical and supercritical cases were reported.

The normalized pressure jump due to an oblique incompressible gust is defined now; the general case for skewed compressible gust can be calculated by means of the similarity rules just explained. the computation differs depending on the parameter k_2:

- $k_2 \leq 0.3$

$$g_0(\xi, k_1, k_2) = \frac{1}{\pi}\sqrt{\frac{1-\xi}{1+\xi}} S(\overline{k}_1) \exp\left(i\overline{k}_1 \hat{f}(\frac{k_2}{k_1})\right) \quad (3.104)$$

With:

$$\hat{f}(\epsilon) = (\sqrt{1+\epsilon^2} - 1)(i\frac{\pi}{2} - \log\epsilon) + \sqrt{1+\epsilon^2}\log(1 + \sqrt{1+\epsilon^2}) - \log 2 \quad (3.105)$$

- $k_2 > 0.3$

$$g_0(\xi, k_1, k_2) = g_{0,1}(\xi, k_1, k_2) + g_{0,2}(\xi, k_1, k_2) \quad (3.106)$$

$$g_{0,1}(\xi, k_1, k_2) = \frac{1}{\pi\sqrt{\pi(\overline{k}_2 + i\overline{k}_1)(1+\xi)}} \exp(-\xi\overline{k}_2 + i\overline{k}_1) \quad (3.107)$$

$$g_{0,2}(\xi, k_1, k_2) = \frac{1}{\pi\sqrt{2\pi(\overline{k}_2 + i\overline{k}_1)}} [erf(2\overline{k}_2(1-\xi)) - 1] \exp(-\xi\overline{k}_2 + i\overline{k}_1) \quad (3.108)$$

This concludes the modeling of turbulent inflow noise based on Amiet-Paterson theory. As it can be seen such a model is quite complex and requires deep knowledge of unsteady aerodynamics; in addition to that, this method relies on strong assumptions:

- The whole theory is built considering a flat plate with no thickness nor camber.
- The noise spectrum is **independent** on the angle of attack.

Implementation of all the above formulas is often avoided in practical application: approximate expressions of $SPL_{1/3}$ are given by the authors, as will be shown in section 3.2.1.

Studies have tried to extend the prediction capacity of the model: *Moriarty and Guidati*[25] developed a method to correct $SPLs$ of *Amiet* in order to take into account the real shape of the profile and the angle of attack, based on previous studies conducted by *Guidati et Al*[24]; those corrections have been included in the prediction code and are explained in a later section.

Approximated expressions for far-field noise

Expression given in equation 3.75 can be approximated to directly give sound pressure level in 1/3 octave band discretization. This solution allows a much faster implementation procedure with respect to the full method previously described and is usually adopted in wind turbine application ([42]).

In case of observer placed directly above the profile $x_1 = x_2 = K_2 = 0$, the far-field power spectral density may be expressed as:

$$S_{pp}(x_1, x_2, x_3, \omega) = S_p p(0, 0, x_3, \omega) = \left(\frac{\omega \rho_0 b}{c_0 z}\right)^2 \pi U d |g(\hat{\omega})|^2 \Phi_{ww}(K_1, 0) \tag{3.109}$$

With $g(\hat{\omega})$ two-dimensional airfoil lift response function and $\hat{\omega} = \omega b/U$ is the reduced frequency. In the high frequency asymptote, airfoil response function may be approximated as:

$$\lim_{\hat{\omega} \to \infty} \quad g(\hat{\omega}) = \frac{-i}{\pi \hat{\omega} \sqrt{M}} \tag{3.110}$$

Inserting this expression in 3.109, together with 3.78, one obtain:

$$S_{pp}(z,\omega) = \frac{d}{\pi c_0}\left(\frac{2L}{3\pi z}\right)^2 \frac{\overline{u^2}}{U^2}(\rho_0 U^2)^2 \left[\frac{\Gamma(1/3)}{\Gamma(5/6)}\right]^2 \frac{\hat{K}_1^2}{(1+\hat{K}_1^2)^{7/3}} \tag{3.111}$$

It is possible to express the results in sound pressure level, multiplying the power spectral density by a third octave bandwidth

$$\Delta\omega = 2\pi\Delta f = 2\pi 0.232 f \tag{3.112}$$

$$SPL_{high} = 10\log_{10}\left(\frac{4\pi 0.232 f S_{pp}}{P_{ref}^2}\right) \tag{3.113}$$

The factor 2 is necessary to convert from double-sided to single-sided PSD and the subscript *high* indicates that the formula has been obtained for the high-frequency asymptote. At this point the approximated expression is readily obtained:

$$SPL_{high} = 10\log_{10}\left(\frac{Ld}{x_3^2}M^5\frac{\overline{u^2}}{U^2}\frac{\hat{K}_1^3}{(1+\hat{K}_1^2)^{7/3}}\rho_0^2 c_0^4\right) + 10\log_{10}\left(\frac{2\times 0.232\sqrt{\pi}}{\pi P_{ref}^2}\left(\frac{2}{3\pi}\right)^2\frac{\Gamma(1/3)}{\Gamma(5/6)}\right) \tag{3.114}$$

The right term of 3.114 is grouping all the known terms, and assumes different values depending on the system of units of measure used. In his original work Amiet adopted $P_{ref} = 2\times 10^{-4} dynes^2/cm^4$, leading to:

$$10\log_{10}\left(\frac{2\times 0.232\sqrt{\pi}}{\pi P_{ref}^2}\left(\frac{2}{3\pi}\right)^2\frac{\Gamma(1/3)}{\Gamma(5/6)}\right) = 58.4 \tag{3.115}$$

In the case of S.I. units, the reference pressure is $P_{ref} = 2\times 10^{-5} Pa$, and the constant assumes the value of 78.4.

Finally, the general expression to be implemented numerically for approximation of high frequency turbulent inflow noise is:

$$SPL_{high} = 10\log_{10}\left(\frac{L_t d}{x_3^2}M^5\frac{\overline{u^2}}{U^2}\frac{\hat{K}_1^3}{(1+\hat{K}_1^2)^{7/3}}\rho_0^2 c_0^4\right) + 78.4 \tag{3.116}$$

Turbulent inflow noise is then strongly dependent on the turbulent integral length-

scale L_t and the turbulence intensity $I = \overline{u^2}/U^2$. ρ_0, c_0 are expressed in kg/m^3 and m/s, respectively. It must be remarked the fact that use of eq.3.116 must be coherent: adoption of units of measure different from those shown would need a redefinition of the constant present in the equation.

Low frequency approximation are also given by *Amiet*[23]; however in the current implementation expression by Lowson [17] is preferred, assuring a smooth transition between low and high frequency regimes:

$$SPL_{total} = SPL_{high} + 10\log_{10}\left(\frac{LFC}{1+LFC}\right) \tag{3.117}$$

The term LFC stands for *Low frequency correction*, approximated by the following expression:

$$LFC = 10S^2M\frac{\overline{\omega}^2}{\beta^2} \tag{3.118}$$

The Sears function S is given by Lowson in a very simple form:

$$S^2 \approx \left(\frac{2\pi\overline{\omega}}{\beta^2} + \left(1 + 2.4\frac{\overline{\omega}}{\beta^2}\right)^{-1}\right)^{-1} \tag{3.119}$$

All the formulas given above have been obtained thanks to the hypothesis of source located directly above the profile. This fact may be overcome by taking into account, in eq. 3.116, the directivity of sound, as reported by *Moriarty et al*[26]:

$$SPL_{high} = 10\log_{10}\left(\frac{Ld}{R^2}M^5\frac{\overline{u^2}}{U^2}\frac{\hat{K}_1^3}{(1+\hat{K}_1^2)^{7/3}}\rho_0^2c_0^4D_L\right) + 78.4 \tag{3.120}$$

Term R indicates the distance between source and observer. Function D_L is the same function used for low frequency directivity in the BPM model:

$$D_L(\Theta_e, \Phi_e) = \frac{\sin^2\Theta_e \sin^2\Phi}{(1+M\cos\Theta_e)^4} \tag{3.121}$$

Where the angles present in the equation are, again, the same shown in fig. 3.2

Extension of Amiet theory for cambered airfoils

As already mentioned above, the Amiet theory computes spectra of flat plates, thus neglecting the real shape of the airfoil. Sound spectra are, in fact, overpredicted by Amiet theory, and noise level decreases as the profile thickens. *Guidati* [24] derived a method to correct the sound pressure levels predicted by Amiet by adding a terms that takes into account shape and camber of the real profile. The method uses a boundary-element solver to compute mean flow and interaction between sound waves and solid surface. Even though the model accurately predicts noise differences due to shape of airfoils, it is too computationally expensive for being used in the evaluation of turbulent inflow noise of a whole wind turbine (it is, nonetheless, faster than any computational aeroacoustics code). For this reason *Moriarty* and *Guidati* [43] [26] developed a simplified model based on geometric characteristics of six airfoils in use on wind turbine applications.

Validity of correction is limited to Mach numbers in the order of $M \approx 0.1 - 0.2$ and in this range the correction factor is depending in airfoil shape and Strouhal number only. For Strouhal numbers below 75, influence of camber and thickness on ΔSPL is less than $2dB$, and this is considered to be the limit of the tool.

Geometric input of the model are the relative thickness of the profile at 1% and 10% of the chord, namely $D_{rel,1\%}$ and $D_{rel,10\%}$, reported in fig. 3.4, taken from [26].

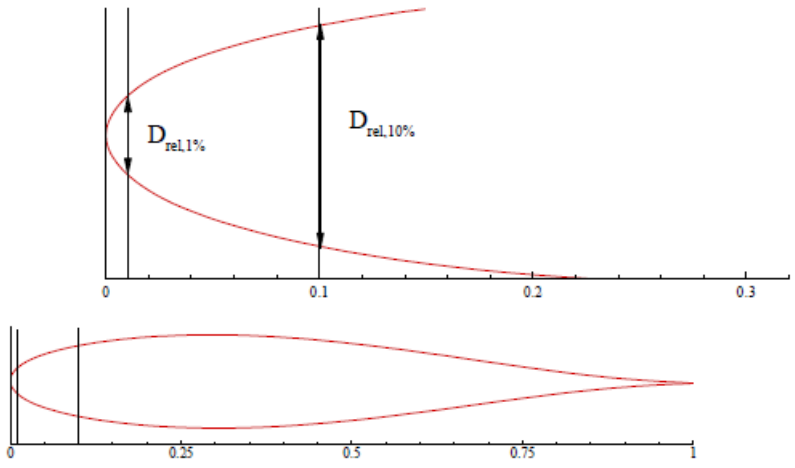

Figure 3.4: Geometric parameters of Moriarty-Guidati model

Inflow turbulence noise indicator IT is given by:

$$IT = D_{rel,1\%} + D_{rel,10\%} \tag{3.122}$$

This term is used to estimate a slope parameter SL, obtained through quadratic fitting:

$$SL = 1.123IT + 5.317IT^2 \tag{3.123}$$

The complete formula for the difference in SPL between airfoil and flat plate is:

$$\Delta SPL_{TI} = -\left(1.123\left(D_{rel,1\%}+D_{rel,10\%}\right)+5.317\left(D_{rel,1\%}+D_{rel,10\%}\right)^2\right)\left(\frac{2\pi fc}{U_{inf}}+5\right)+10 \tag{3.124}$$

With c chord of the profile. The additional factor of 10 has been included by *Moriarty* and *Guidati* in order to achieve a better fitting among experimental data. It must also be remarked that the formula above mentioned is an approximation of the full Guidati method and as such its applicability is limited; using the model outside its boundaries would result in a too strong correction.

Another correction to take into account geometry of profiles is that proposed by *Tian, Cotté and Chaigne* [44], based on data reported by *Roger and Moreau.* sound pressure level reduction is given by the following formula:

$$\Delta SPL_{TI} = -9/50\frac{(e/c)}{(e/c)_{ref}}\frac{f}{U_{inf}}\frac{(L_t/c)_{ref}}{(L_t/c)} \tag{3.125}$$

With e maximum thickness of the profile, L_t integral lengthscale of the turbulence. The subscript $_{ref}$ stands for "reference": in the current implementation, $(e/c)_{ref} \approx 0.12$ and $(\Lambda/c)_{ref} \approx 0.1$.

3.2.2 Lowson model

A second model for the computation of turbulent inflow noise included in the current implementation is the one developed by Lowson [17], who adopted and modified the model of Amiet [22] to make it more suitable for wind turbine applications. The expression given by Lowson is formally identical to that shown by eq. 3.116; all the

formulas below indicates SPL discretized in 1/3 octave bandwidth:

$$SPL_{high} = 10\log_{10}\left(\rho_0^2 c_0^2 L_t \frac{d}{r^2} M^3 \overline{u^2} \frac{K^3}{(1+K^2)^{7/3}}\right) + 58.4 \tag{3.126}$$

With:

$$K = \frac{\pi f c}{U_{inf}} \tag{3.127}$$

For the high frequency domain. Low frequency range can be calculated through equations 3.117,3.118 and 3.119.

Although extensively used (e.g. [27], [26]), derivation of Lowson model was not found in the literature. Units of measure were not reported by Lowson but, considering the fact that the constant is set to 58.4, units are supposedly g/cm^3 for ρ_0 and cm/s for c_0, the same of *Amiet-Paterson* model.

Different are the results obtained from implementation of Lowson model by different authors: *Moriarty*[26] used S.I units in his implementation, obtaining turbulent inflow noise largely dominating the whole frequency spectrum, while *Madsen* [27] units are not reported but the turbulent inflow spectrum dominates only at low frequency. In a work from *DTU*, *Wei Jun Zhu*[45] implemented a "modified" version of Lowson model:

$$SPL_{high} = 10\log_{10}\left(\overline{D}_h \rho_0^2 c_0^2 L_{turb} \frac{d}{r^2} M^3 \frac{\overline{u^2}}{U_{mean}^2} \frac{K^3}{(1+K^2)^{7/3}}\right) + C \tag{3.128}$$

Value of the constant depends on units of measure chosen. It is clear that such a model differs from eq 3.126 by a factor of $1/U_{mean}^2$, and results on total spectra would vary accordingly.

3.2.3 Integral lengthscale and turbulent intensity

As already mentioned, the turbulent inflow model needs the definition of an integral lengthscale L_t and a turbulent intensity I in order to compute noise spectra. Those quantities are required by all the TI models.

In the full Amiet models L_t and I are needed to define the spectrum of vertical

velocity fluctuations:

$$\Phi_{ww}(k_1, k_2) = \frac{4\overline{u^2}}{9\pi k_e^2} \frac{\hat{k}_1^2 + \hat{k}_2^2}{(1 + \hat{k}_1^2 + \hat{k}_2^2)^{7/3}} \tag{3.129}$$

$$k_e = \frac{\sqrt{\pi}}{L_t} \frac{\Gamma(5/6)}{\Gamma(1/3)} \tag{3.130}$$

Whit $\overline{u^2} = I^2 U_{mean}^2$. For what concerns Amiet approximated and Lowson model, those quantities enter directly equations for the SPL (eq: 3.116,3.126).

Many are the approaches available in the literature for estimating L_t and I for wind turbine applications. *Moriarty et al*[26] sets L_t as a function of distance from the ground up to a specific height, where it is then set constant. Another approach is the one proposed by *W.J. Zhu et al*[45], in which the turbulence intensity is given as a function of height from the ground h and surface roughness z_0, according to *Couniham* [46]:

$$I = \gamma \frac{\log(h/z_0)}{\log(h/z_0)} \tag{3.131}$$

$$\gamma = 0.24 + 0.096 \log_{10} z_0 + 0.016 (\log_{10} z_0)^2 \tag{3.132}$$

Also L_t is modeled by:

$$L_t = 25 h^{0.35} z_0^{-0.063} \tag{3.133}$$

Table 3.5 reports examples of surface roughness for various types of ground surfaces. A third approach followed in the literature has been used by *Boorsma and Schepers*[28] based on *ESDU* standards [47]:

$$I = \frac{0.286 + 0.187 \log_{10} H - 0.081 \log_{10}^2 H}{z_0^{0.07} \log_{10} H / \log_{10} z_0} \tag{3.134}$$

$$L_t = 2H \Big(0.5 + 0.316 (3 + \log z_0) \Big) \tag{3.135}$$

With H hub height of the wind turbine. Comparison among *Moriarty* and *W.J.Zhu* turbulent length is plotted in Fig.3.5, where strong differences between the two models can be observed: there is in fact no generally unified vision of the problem. The aeroacoustic community is still discussing about which model should be used, being turbulent inflow noise a very complicated noise source to measure and validate.

In the present implementation solution proposed by *Moriarty* has been adopted and L_t is defined as:

$$L_t(h) = \begin{cases} 0.7h & h \leq 60m \\ 42 & h > 60m \end{cases} \tag{3.136}$$

$\overline{u^2}$ is computed as the root mean square of the component of the relative velocity normal to the airfoil chord, allowing to finally compute the turbulent inflow noise.

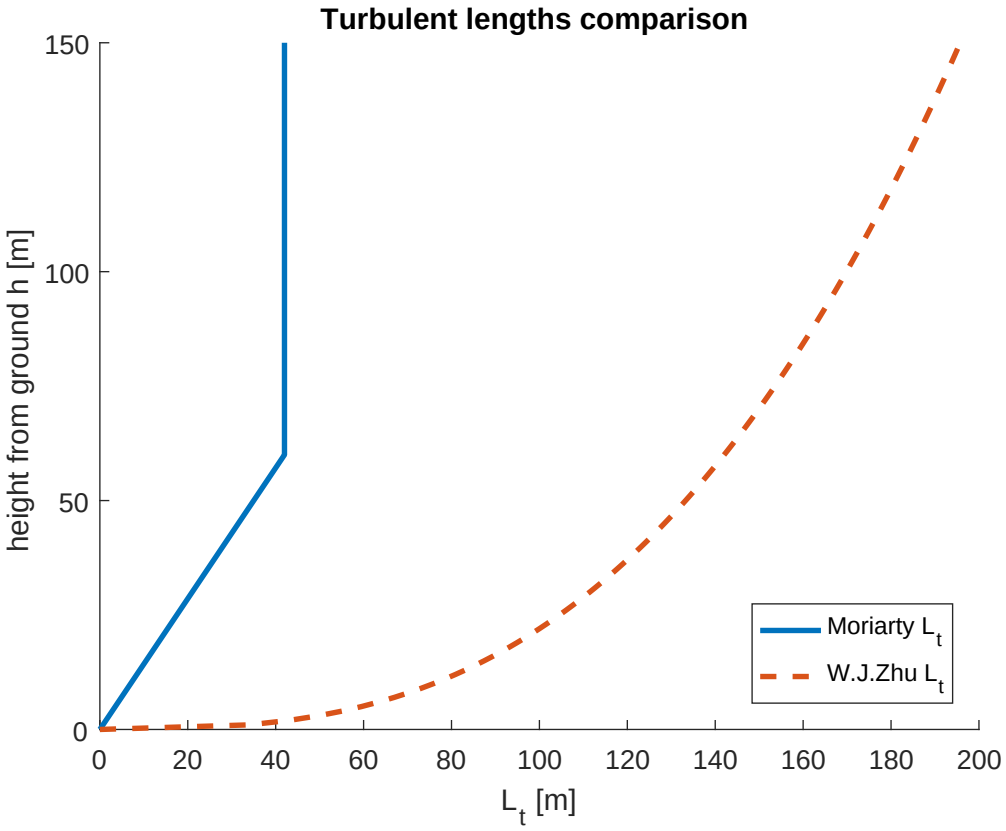

Figure 3.5: Comparison among turbulent length from Moriarty and W.J.Zhu models as a function of distance from ground, for lawn grass terrain.

Terrain type	$z_0(mm)$
Very smooth, ice or mud	0.01
Calm open sea	0.20
Blown sea	0.50
Snow surface	3.00
Lawn grass	8.00
Rough pasture	10.00
Fallow field	30.00
Crops	50.00
Few trees	100.00
Many trees, hedges	250.00
Forest and woodlands	500.00
Suburbs	1500.00
Centers of cities with tall buildings	3000.00

Table 3.5: Surface roughness for various types of terrain

Chapter 4

Numerical Tools

In this section a description of the softwares used or developed for the present work is given. The first tools presented are *Cp-Lambda* and *Cp-Max*, that together constitutes the framework in which the aeroacoustic code developed operates. After that, the software *NAFNoise* from *NREL* is explained; this code have been particularly useful for debugging the noise source models described in the previous chapter. In the last section description of the implementation of the aeroacoustic model implemented is given.

4.1 Cp-Lambda and Cp-Max

Determination of dynamic simulations of the wind turbines have been performed using the aero-servo-elastic finite element software ***Cp-Lambda*** [48] (Code for Performance, Loads, Aero-Elasticity by Multi-Body Dynamic Analysis), a software developed by the Department of Aerospace Engineering at Politecnico di Milano. The code was initially developed for helicopter application but, due to the multibody nature of the code, it has been possible to turn it into a valid tool for wind turbine modeling and design. Sketch of a horizontal axis wind turbine model is reported in fig. 4.1. Structure of a real wind turbine is virtually modeled by using structural elements such as beams, rigid bodies, joints, actuators, sensors and many others, taken from Cp-Lambda libraries. Beams are described by their 6×6 stiffness matrix, allowing a complete aeroelastic description of the problem. Aerodynamics is modeled by lifting line theory that, although being a simplified model, is able to

describe accurately the loading condition on the rotor.

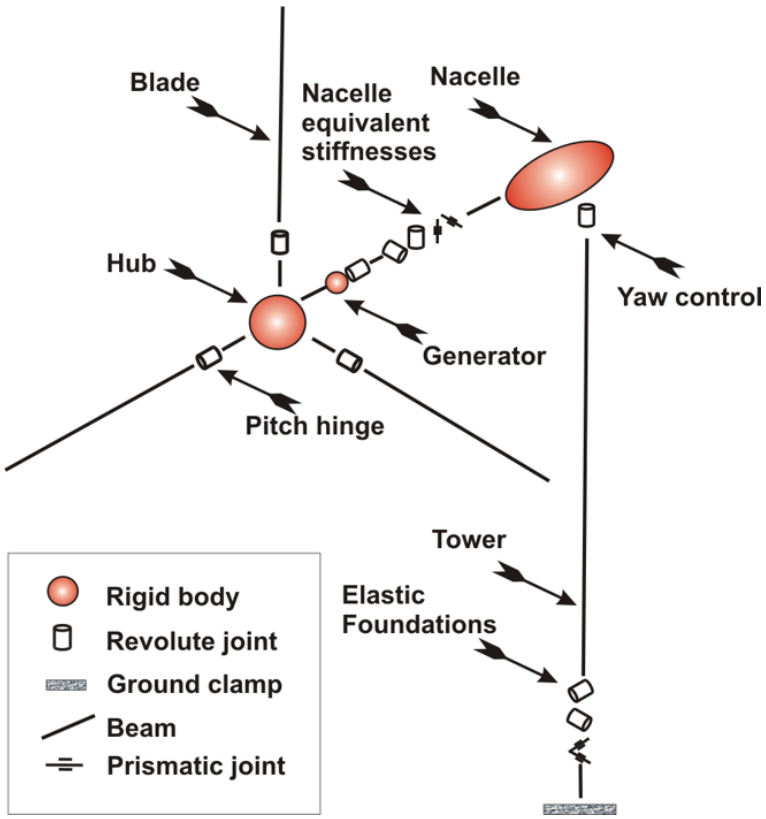

Figure 4.1: Multibody model of a HAWT in Cp-Lambda

It is possible to give, during aeroelastic simulations, informations about the wind time history acting on the model. Turbulent wind grids can be generated by the software *Turbsim*[49]; this tool can take as input informations such as turbulence intensity, mean speed, wind shear, ecc and generate a wind grid accordingly.

Informations about the simulation are retrieved thanks to the so-called *sensors*: those units can be placed in any element or position of the wind turbine model and can be of various type, depending on the quantity to be measured (loads, displacements, deformations, rotations, ecc...). Position of sensors must be specified by the user as input before running the simulation; once the process has successfully converged, the required informations are written in an output file.

Cp-Max is the multidisciplinary framework in which Cp-Lambda is used, developed specifically for wind turbines applications. This powerful tool, developed in $MATLAB^{®}$ environment, can be used for simulation or design of wind turbines (Fig 4.2). Differently from Cp-Lambda, whose use is quite complex and requires

deep knowledge of the code, Cp-Max "only" requires definition of an input file in excel format.

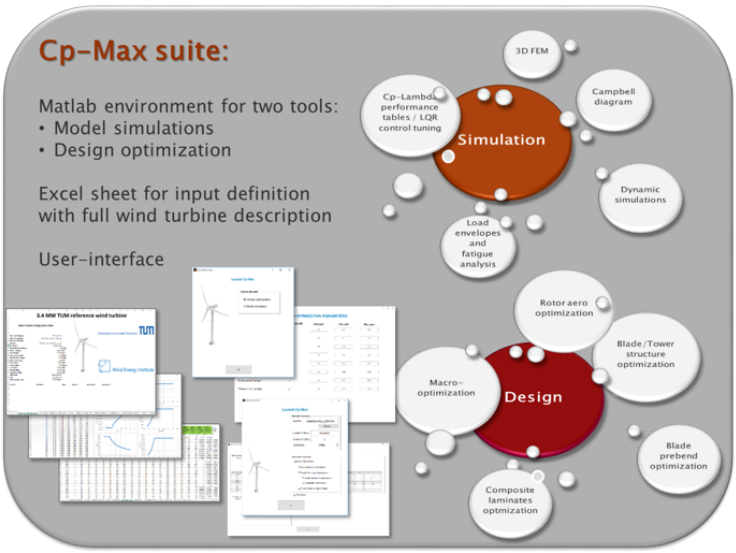

Figure 4.2: Cp-Max Framework: Overview

In the present work Cp-Max has been used principally in simulation mode; main features of this routine are:

- Generation of Campbell diagram
- Generation of Cp-TSR diagram
- Creation of control laws
- Generation of wind grid (through *TURBSIM*)
- Computation of static simulations
- Computation of dynamic simulations
- Fatigue analysis

Static simulations are used as starting point for the dynamic ones while wind grids are generated depending on the design load cases (DLC) to simulate, according to IEC-61400-1, [50].

Finally, the modularity of Cp-Max makes it suitable for extensions through implementation of additional modules (such as the aeroacoustic module object of the present study).

4.2 NAFNoise

NAFNoise is an open source software developed by *Pat Moriarty* from *NREL*[51], able to predict aeroacoustic emission of an airfoil section. The code, whose name stands for *NREL Airfoil Noise*, allows the user to compute the noise spectra of any airfoil shape and to take into account all the noise sources already mentioned in the previous sections such as turbulent boundary layer-trailing edge noise, separation-stall noise, laminar boundary layer- vortex shedding, trailing edge bluntness noise and turbulent inflow noise.

Inputs of the code include atmospheric parameters, airfoil properties, computation settings and observer location: a complete set of the input required can be found in [51]: those inputs are very similar to the ones needed by the aeroacoustic 2d solver used in section 5. Outputs of the software are given in sound pressure levels discretized on a 1/3 octave band, from $10Hz$ to $20KHz$. Example of such outputs is reported in fig. 4.3.

Several are the models implemented in the code: BPM model by *Brooks, Pope and Marcolini* was the first model implemented [39]. More recently TNO model (described in 3.1.1) has been included, as reported in [26]; inclusion of *Xfoil* in the code allows computation of any airfoil shape. Turbulent inflow noise model from *Amiet* was included, and thickness correction through full Guidati or approximated Moriarty-Guidati can be applied.

Output file of NAFNoise v1.00 for s809.dat
Executed 03-Jan-2017 at 01:33:18
==========

ONE-THIRD OCTAVE
SOUND PRESSURE LEVELS

FREQUENCY(HZ)	PRESSURE SIDE TBL	SUCTION SIDE TBL	SEPARATION SIDE TBL	LAMINAR	BLUNTNESS	INFLOW	TOTAL
10.000	-28.339	6.738	-100.000	0.000	-10.694	16.885	17.293
12.500	-20.735	12.061	-100.000	0.000	-9.119	21.260	21.757
16.000	-12.955	17.454	-100.000	0.000	-7.376	25.984	26.556
20.000	-6.465	21.908	-100.000	0.000	-5.801	30.129	30.740
25.000	-0.466	25.989	-100.000	0.000	-4.226	34.136	34.757
31.500	5.258	29.849	-100.000	0.000	-2.595	38.112	38.718
40.000	10.682	33.478	-100.000	0.000	-0.909	41.993	42.568
50.000	15.322	36.563	-83.319	0.000	0.666	45.355	45.898
63.000	19.722	39.475	-53.741	0.000	2.297	48.497	49.014
80.000	23.867	42.213	-28.245	0.000	3.984	51.286	51.800
100.000	27.394	44.547	-8.621	0.000	5.559	53.381	53.925
125.000	30.615	46.693	7.405	0.000	7.134	54.913	55.536
160.000	33.853	48.876	21.473	0.000	8.876	55.912	56.720
200.000	36.513	50.707	31.360	0.000	10.451	56.203	57.330
250.000	38.947	52.427	39.014	0.000	12.026	55.965	57.676
315.000	41.255	54.120	45.058	0.000	13.657	55.233	58.044
400.000	43.444	55.805	49.805	0.000	15.344	54.034	58.759

Figure 4.3: Example of output from NAFNoise

4.3 Aeroacoustic Module

Computation of noise spectra from wind turbines has required the development of an aeroacoustic module able to cope with the aeroelastic simulations performed by Cp-Max. As already mentioned, modularity of the code has allowed implementation of the module by making only minor changes to the rest of the code. Noise analysis has then been added as an additional tool available to Cp-Max in the simulation mode; graphic user interface (GUI) of Cp-Max is reported in Fig. 4.4.

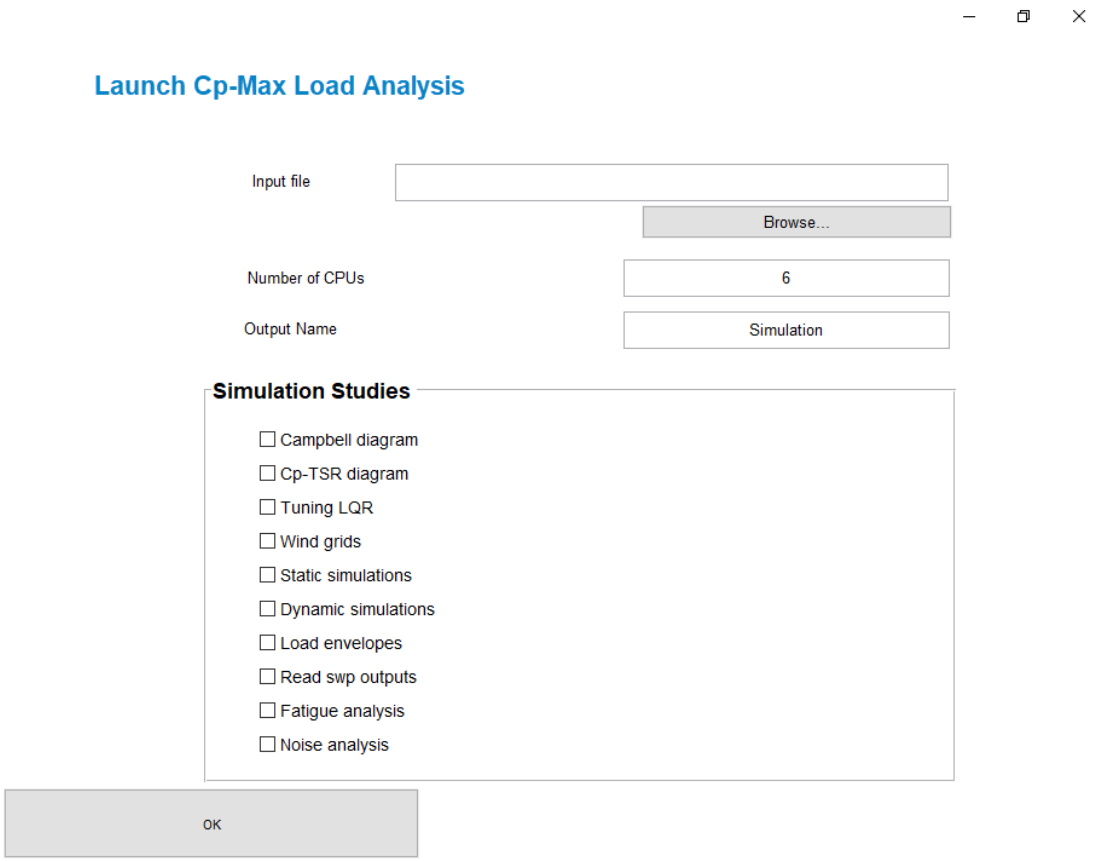

Figure 4.4: Graphic user interface of Cp-Max simulation routine

Main purpose of the module is generation of noise spectra produced by a wind turbine and perceived by an observer (or many observers) placed around the model.

The aeroacoustic module is build to take as input the dynamic simulations coming from Cp-Lambda, geometric information of the rotor and many other informations (constants, settings, etc...) and can produce as output a great variety of useful parameter to assess the noise emission of the turbine, such as sound pressure level, sound power level, A-Weighted SPL and overall SPL.

Many are the models implemented to compute noise. All of those have been already described in the previous chapter and are here summarized:

Turbulent Boundary Layer - Trailing Edge noise

- TNO - directivity based on Howe[10]
- TNO - directivity based on Bertagnolio [38]
- BPM

Turbulent inflow noise

- Full Amiet
- Approximated Amiet
- Lowson

Thickness corrections based on *Moriarty-Guidati* or *Roger-Moreau* may also be applied to improve turbulent inflow results but, due to the Strouhal limitations already mentioned above, those models very quickly operate outside their boundaries in case of wind turbine applications.

Four are the sections in which the code may be split:

- Input definition
- Preprocessing
- Noise Analysis
- Postprocessing

Description of each part will now be given.

4.3.1 Input definition

The aeroacoustic module necessitates a wide variety of data in order to perform the noise analysis, that must be provided by the aeroelastic simulations.

Computation of turbulent boundary layer - trailing edge noise and turbulent inflow noise is performed through the methods described in chapter 3; by default

the module computes noise spectra from all the $DLC1.1$ produced by $Cp-Lambda$ (i.e. 12 wind speeds simulations), but it is possible to perform single simulation to save up on computational time.

Position of observers must be given in a reference frame with the origin placed on the ground coincident with the tower base, with x vertical and aligned as the tower, y positive if pointing downwind and z defined accordingly, as reported in figure 4.5.

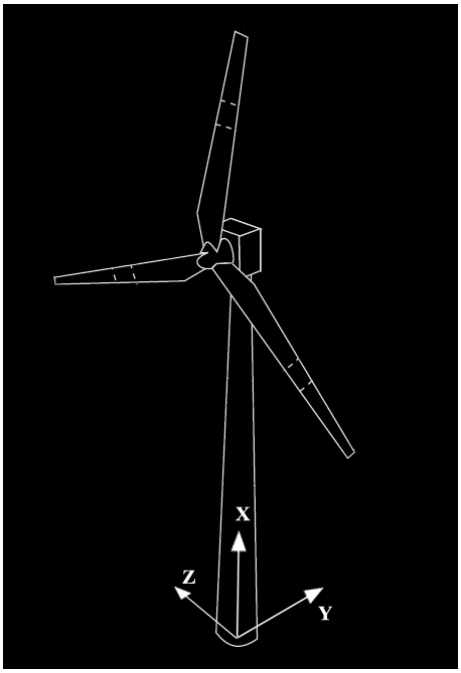

Figure 4.5: Reference frame of the observer

An important parameter to define is the sensor distribution along the blades, given by the parameter $\eta_{simulation}$; this array identifies the position of sensors on the blade, adimensionalized with respect to the blade length. Many different types of data are required by the aeroacoustic module, to be defined for each airstation located at $\eta_{simulation}$:

- Airstation position
- Airstation velocity
- Airstation relative velocity of the flow
- Airstation angle of attack

- Airstation properties ($C_L, C_D, C_M, Chord$)
- Airstation displacements
- Rotor azimuth angle

Once inputs and sensors are defined, dynamic simulations can be run once for all, allowing the user to compute noise spectra without the need of performing all the simulations again.

4.3.2 Preprocessing

After performing the simulations and if computation of noise is required, Cp-Max calls the routine *NoiseAnalysis*.

It is important to mention that noise computation is performed exploiting the "strip theory": blades are divided in several sections of constant chord; noise emitted from each blade portion is then calculated and summation of spectra gives the total noise of the rotor. This approach is intrinsically compatible with outputs from Cp-Lambda in which wind turbine data are given on airstations placed along the blade.

At first, frequency array is defined according to user input discussed in the previous section (frequency bounds, octave discretization). By default noise analysis is performed on a frequency range from $10Hz$ to $20KHz$, covering the whole audible frequency range.

Dynamic simulations are calculated on a simulation time of $630s$, and the use of the whole time window from Cp-Lambda for noise analysis computations would be unnecessary. For this reason, data from dynamic simulations are retrieved and interpolated on a shorter time window and with a sampling frequency f_{sim} . Airstations data are then 3-dimensional arrays, functions of timestep, blade and sensor:

$$f = f(iTime, iBlade, iSensor) \tag{4.1}$$

Example of an angle of attack time history is shown in fig:4.6. At this point the wind turbine configuration is defined on the time set $T_{sim} = [t_1, t_1 + \Delta t, t_1 + 2\Delta t, ..., t_1 + k\Delta t = t_{end}]$, with $\Delta t = 1/f_{sim}$.

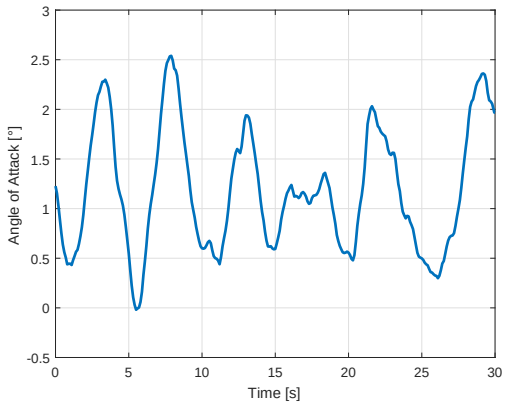

Figure 4.6: Angle of attack time history

Reconstruction of retarded configuration is then performed: as already mentioned, trailing edge noise is considered emitted from the trailing edge while turbulent inflow noise is generated at the mid-chord. Position of trailing edge and mid-chord can then be easily reconstructed by using airstations position and blade chord distribution.

Noise spectra are not defined on the same time vector basis described by the sampling frequency f_{sim}, but it is more convenient to define a new time sequence, sampled by the frequency $f_{analysis}$. This new time set identifies all the observation times t_i in which the retarded configuration must be computed. $f_{analysis}$ is usually set lower than f_{sim}: it is in fact enough to produce only few noise spectra per revolution of the rotor instead of computing retarded configurations at sampling frequency of f_{sim} (typically $f_{analysis} \approx 2 - 3Hz$ and $f_{sim} \approx 20Hz$).

$$T_{obs} = [t_1, t_1 + \Delta t, t_1 + 2\Delta t, ..., t_1 + k\Delta t = t_{end}] \qquad \Delta t = 1/f_{analysis} \tag{4.2}$$

For each $t_i \in T_{obs}$ the emission time τ_i of each noise source is evaluated by solving the nonlinear problem:

$$\tau_i = t_i - \frac{\underline{X}_O - \underline{X}_S(\tau_i)}{c_0} \tag{4.3}$$

Where $\underline{X}_O$ indicates position of the observer and $\underline{X}_S(\tau)$ is the position of noise source, obviously function of time. Through interpolation of time histories τ_i the retarded configuration of the whole wind turbine is calculated for each observation time.

Computation of trailing edge noise requires detailed characterization of the bound-

ary layer. For this purpose the software Xfoil is used, as already discussed above. In order to reduce computational time, BL data are not computed at each time step but collected into lookup tables, defined for a set of Mach numbers, Reynolds numbers and angles of attack (Fig:4.7).

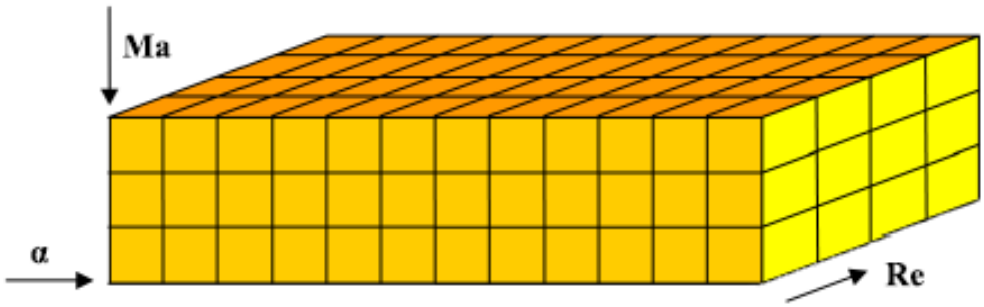

Figure 4.7: Three dimensional lookup table reporting Xfoil boundary layer data structure

Airfoil coordinates are given from the excel input file of Cp-Max and lookup tables are obtained only for those profiles located on the blade portion covered by sensors, i.e. $\eta_{sim}(1) < \eta < \eta_{sim}(end)$, allowing important reduction on computation time.

4.3.3 Noise Analysis

In this section noise spectra for each observer and observation time are calculated, azimuthally averaged and summed up together to give the total noise spectra of the wind turbine.

Noise levels can be computed through all the models, for comparison among the different sources, or can be directly summed to give the overall spectra; the user has complete freedom on the produced outputs.

If turbulent boundary layer - trailing edge noise is required, BL data are retrieved from the lookup tables previously computed and interpolated along the blade to obtain detailed characterization of turbulent boundary layer (for pressure and suction side) for each observation instant.

By default Cp-Max computes a finite number of simulations (12 for the $DLCs1.1$), each one at different wind speed. The user can decide whether to perform noise analysis for all the wind speeds or to select the DLC to analyze. Starting from this point, for each simulation the aeroacoustic code cycles on observation time instants, observers, blades and sensors, computing sound pressure levels for each of the noise model chosen:

$$SPL = SPL(iTime, iObs, iBlade, iSensor) \tag{4.4}$$

Each noise source is then azimuthally averaged and doppler shifting is also taken into account. The approach followed is that taken from *Amiet-Schlinker*[52]; this correction accounts for the fact that each airfoil spends a different acoustic time at each azimuthal location. While this correction is important for helicopters, it has very limited effects for wind turbine applications.

The ratio between angular frequency ω and doppler shifted angular frequency ω_0 can be computed as:

$$\frac{\omega}{\omega_0} = 1 + \frac{\underline{M}_t \cdot \underline{n}_r}{1 - \underline{M}_0 \cdot \underline{n}_r} \tag{4.5}$$

Where:

- $\underline{M}_t$: Relative source-receiver Mach number
- $\underline{M}_0$: Mach number of the source relative to the fluid
- $\underline{n}_r$: Unit vector from retarder source position to the observer

Power spectral densities are then corrected as follows:

$$S_p p(\underline{x}, \omega) = \frac{1}{\phi_2 - \phi_1} \int_{\phi_1}^{\phi_2} \left(\frac{\omega}{\omega_0}\right)^2 S_{PP}(\underline{x}, \omega, \phi) d\phi \tag{4.6}$$

At the end of this section, each noise source model gives as output sound pressure levels for all the rotor, averaged for all the observation times, as a function of the frequency.

4.3.4 Postprocessing

At last, the aeroacoustic modules computes A-Weighted SPL, sound power level, overall SPL and allows the user to plot a number of useful graph for the evaluation

of the noise emitted from the wind turbine.

Weighting factor for A-weighted SPL is obtained through:

$$R_A(f) = \frac{12200^2 f^4}{(f^2 + 20.6^2)\sqrt{(f^2 + 107.7^2)(f^2 + 737.9^2)}(f^2 + 12200^2)} \tag{4.7}$$

A-Weighted SPL is then calculated through summation of normal SPL and the weighting factor:

$$ASPL(f) = SPL(f) + R_A(f) \tag{4.8}$$

Sound power level is computed through relations given by IEC 61400-11:

$$SWL = SPL + 10\log_{10}\frac{4\pi R^2}{S_0} - B \tag{4.9}$$

R is the distance between the rotor center and the microphone, $S_0 = 1m^2$ is a reference area and $B = 6$ takes into account approximate pressure doubling that occurs for the sound level measurements on a ground board.

Overall sound pressure level is computed through summation on incoherent and not in phase sound pressure levels for all the frequencies:

$$OASPL = 10\log_{10}\left(\sum_f 10^{\frac{SPL(f)}{10}}\right) \tag{4.10}$$

Finally, an example of trailing edge, turbulent inflow and total noise SPL is shown in fig 4.8:

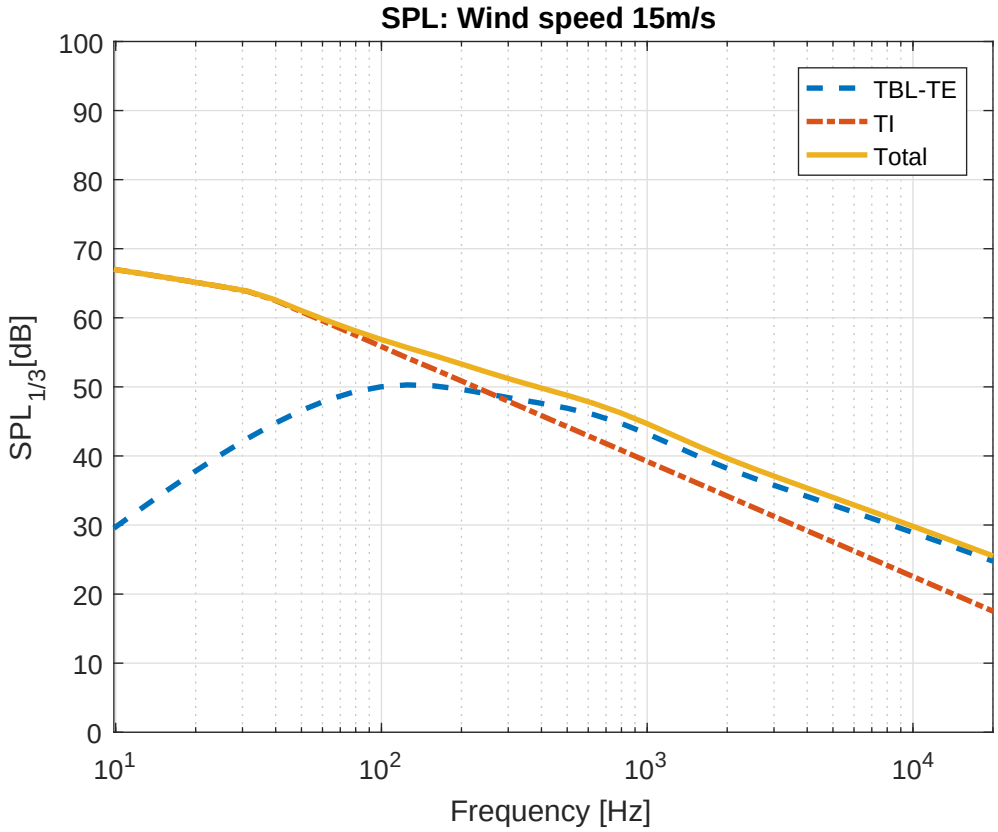

Figure 4.8: SPL output of the aeroacoustic module

Chapter 5

Bidimensional Validation of the models implemented

Before applying the various noise models in the computation of the emission of a whole wind turbine, they have all been compared and tested in order to assure the correct implementation of the models. Validation of results has been performed using experimental data from several publications. In order to do so, an aeroacoustic 2d solver that computes the noise spectrum of an isolated wing section have been developed: the code takes as input a great number of variables, described in Appendix A); the user can choose which model to use and the noise source to take into account. This code is somewhat similar to the NREL's software NAFNoise, which has been also included in the present aeroacoustic solver, easying the debugging phase.

5.1 Turbulent Boundary layer - Trailing edge noise

Validation of TBL-TE BPM noise model has been performed through direct comparison with the experimental data from *Brooks et al.*[39]. This document, in fact, reports experimental results under a great number of different conditions, being so far one of the most complete source of data available in the literature.

TNO models have been compared with the ones obtained from the BPM previously validated, showing good agreement. It has in fact not been possible to compare results of the current TNO implementation with many others implementation of the

same model due to the general lack of data in the literature: almost no publication reports the complete set of parameters necessary for the computation of noise emissions, limiting very much accuracy of results. Considering that, a comparison with results from the database BANC III [53] has been finally performed, and generally good results are obtained.

5.1.1 BPM model

In order to validate the BPM model, sound pressure levels (discretized on 1/3 octave band) from NAFNoise and current implementation of TBL have been compared with those taken from *Brooks, Pope and Marcolini*. Acoustic measurements were performed on $NACA0012$ airfoils of various chords, at different wind speeds and angles of attack. The microphone was placed directly above the trailing edge, i.e. $\Phi = \Theta = 90°$ (reference angle as 3.1). Transition of boundary layer was forced through application of strips from the leading edge up to 20% of the chord, and boundary layer thickness is given as empirical function of Re and α.

Wind section span is $0.45m$ while distance between source and observer is set to $1.22m$; comparison between suction and pressure sides are reported, while only total SPL are shown if $\alpha = 0°$, due to the symmetrical shape of $NACA0012$.

Figures 5.1-5.4 shows that the current implementation of BPM essentially coincides with data from NAFNoise and experimental data, demonstrating the correct implementation of the tool. A comparison between NAFNoise and the current implementation at varying angle of attack is shown in fig 5.5:

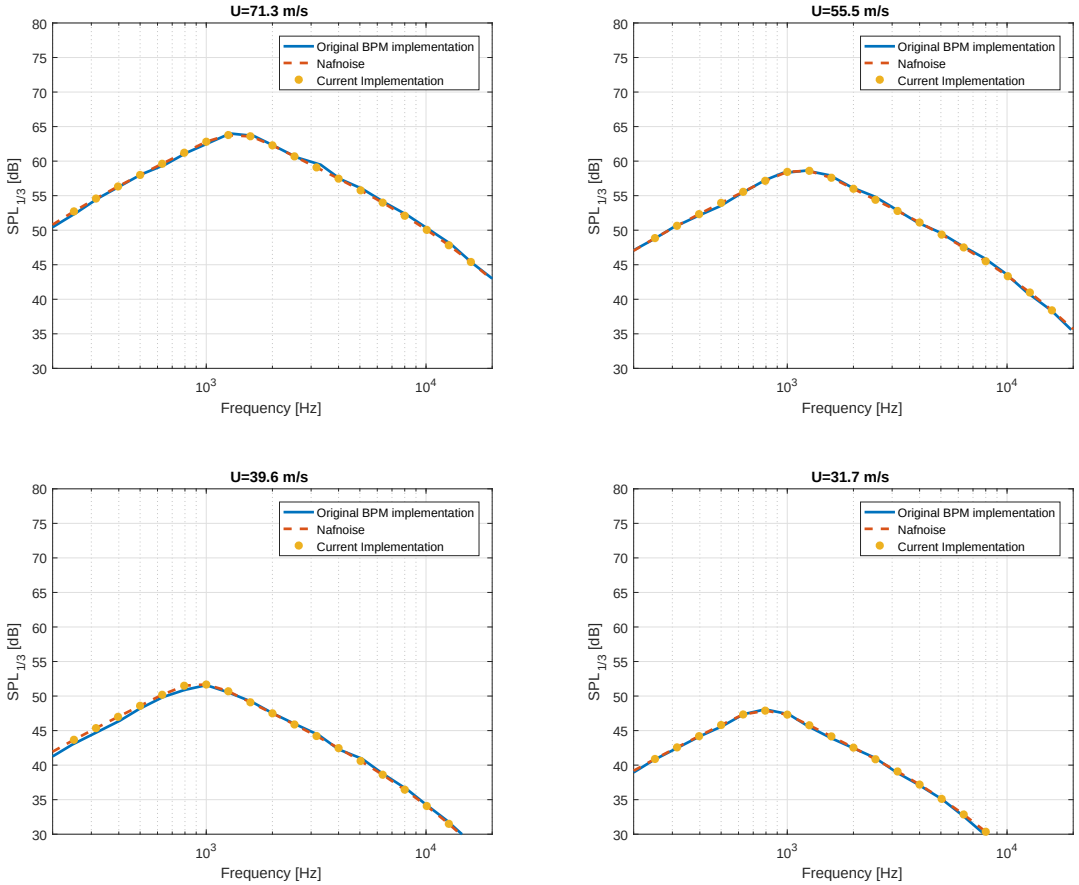

Figure 5.1: Total SPL comparison between BPM models: $Chord = 0.3048m$, $\alpha = 0°$

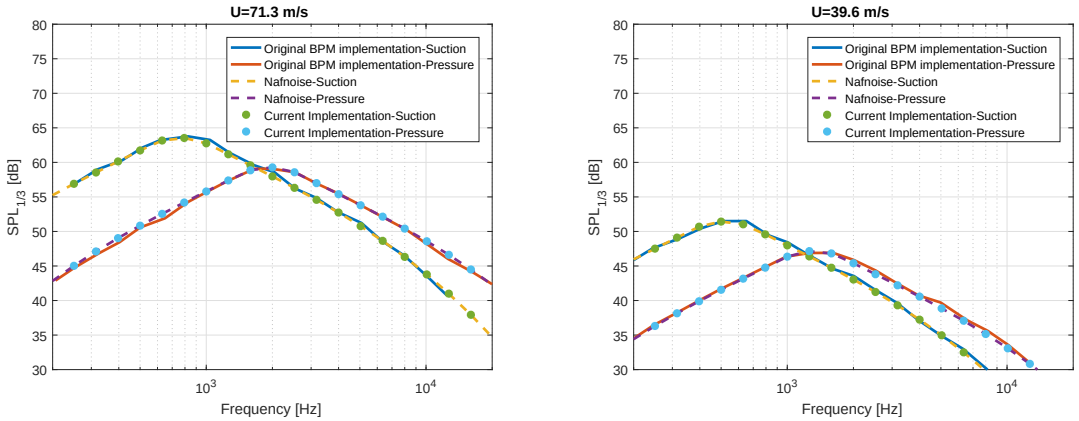

Figure 5.2: Suction and Pressure side SPL comparison between BPM models: $Chord = 0.3048m$, $\alpha = 4°$

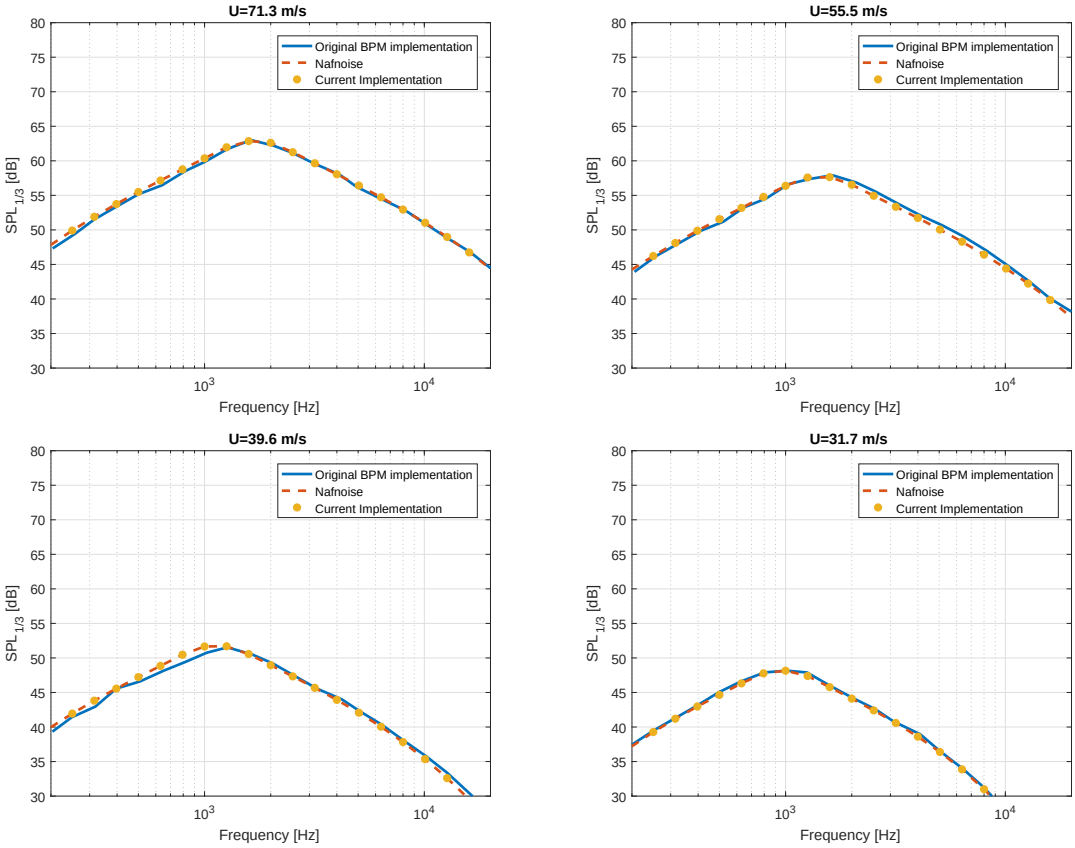

Figure 5.3: Suction and pressure side SPL comparison between BPM models: $Chord = 0.2286m$, $\alpha = 0°$

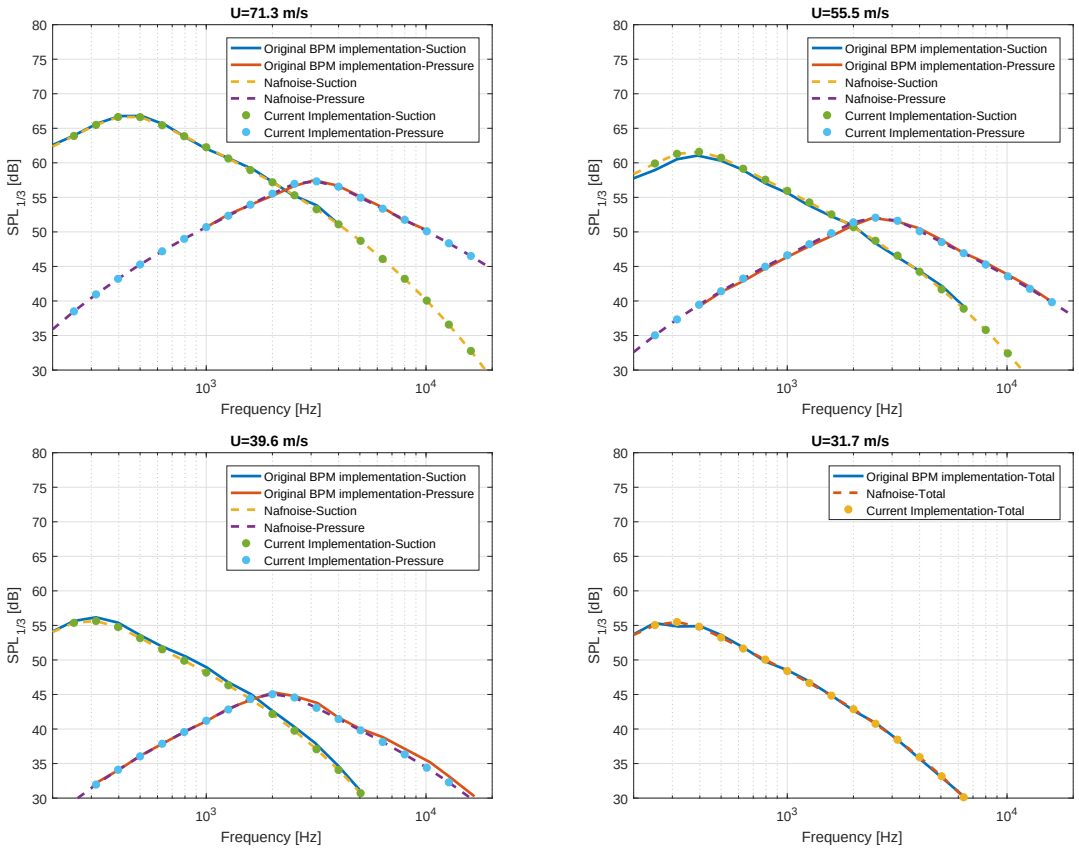

Figure 5.4: Suction and pressure side SPL comparison between BPM models: $Chord = 0.2286m$, $\alpha = 7.3°$

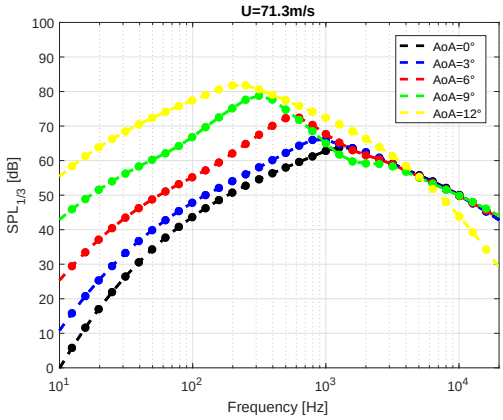

Figure 5.5: Comparison between NAFNoise (dashed) and current implementation (dotted) of BPM model, for increasing angles of attack

As already mentioned boundary layer input can be given through empirical formula or panel methods (i.e. Xfoil). It is important then to evaluate the difference in SPL given by different BL computations. Such evaluation is performed for a $NACA0012$ in fig:5.8: accordance between noise spectra worsen as the angle of attack increases, due to different boundary layer thicknesses predicted by the two methods (the only input of the BPM model varying with the angle of attack). It must be said however that such differences may be due to the tripping of the boundary layer applied by Brooks, Pope and Marcolini, that is not replicable through Xfoil.

It is also important to remark that experimental fitting on displacement thickness δ^* are valid **only** for $NACA0012$ (fig: 5.6); this is the main limitation of the BPM model: shape of the airfoil comes into the model only through δ^*, then every airfoil with a given displacement thickness $\overline{\delta}^*$ at the trailing edge would produce the same noise spectrum of a $NACA0012$ with the same displacement thickness. In fig:5.9 SPL from a very different airfoil ($DU08-W-210$, used in wind energy applications, fig:5.7) is presented, showing a great similarity with the spectra of fig: 5.8.

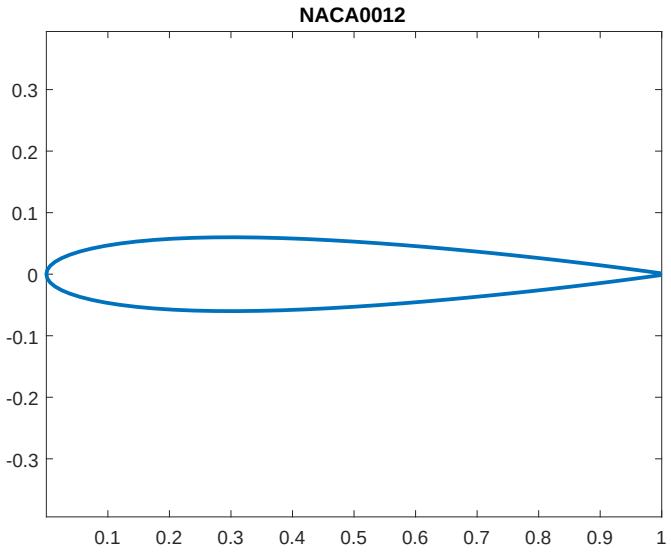

Figure 5.6: NACA0012

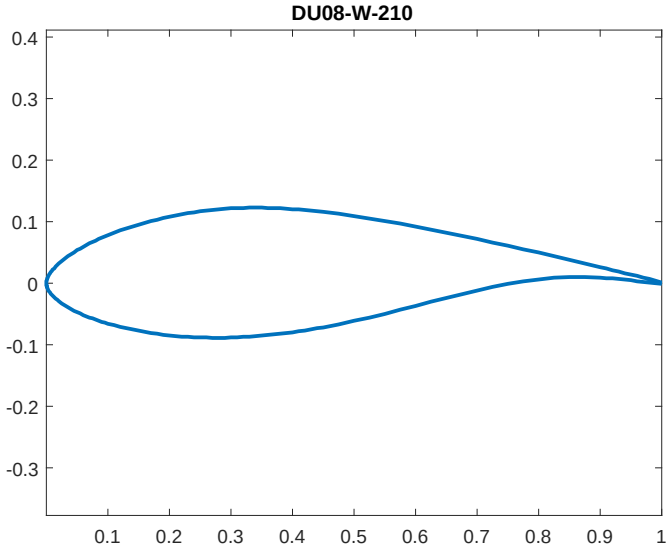

Figure 5.7: DU08-W-210

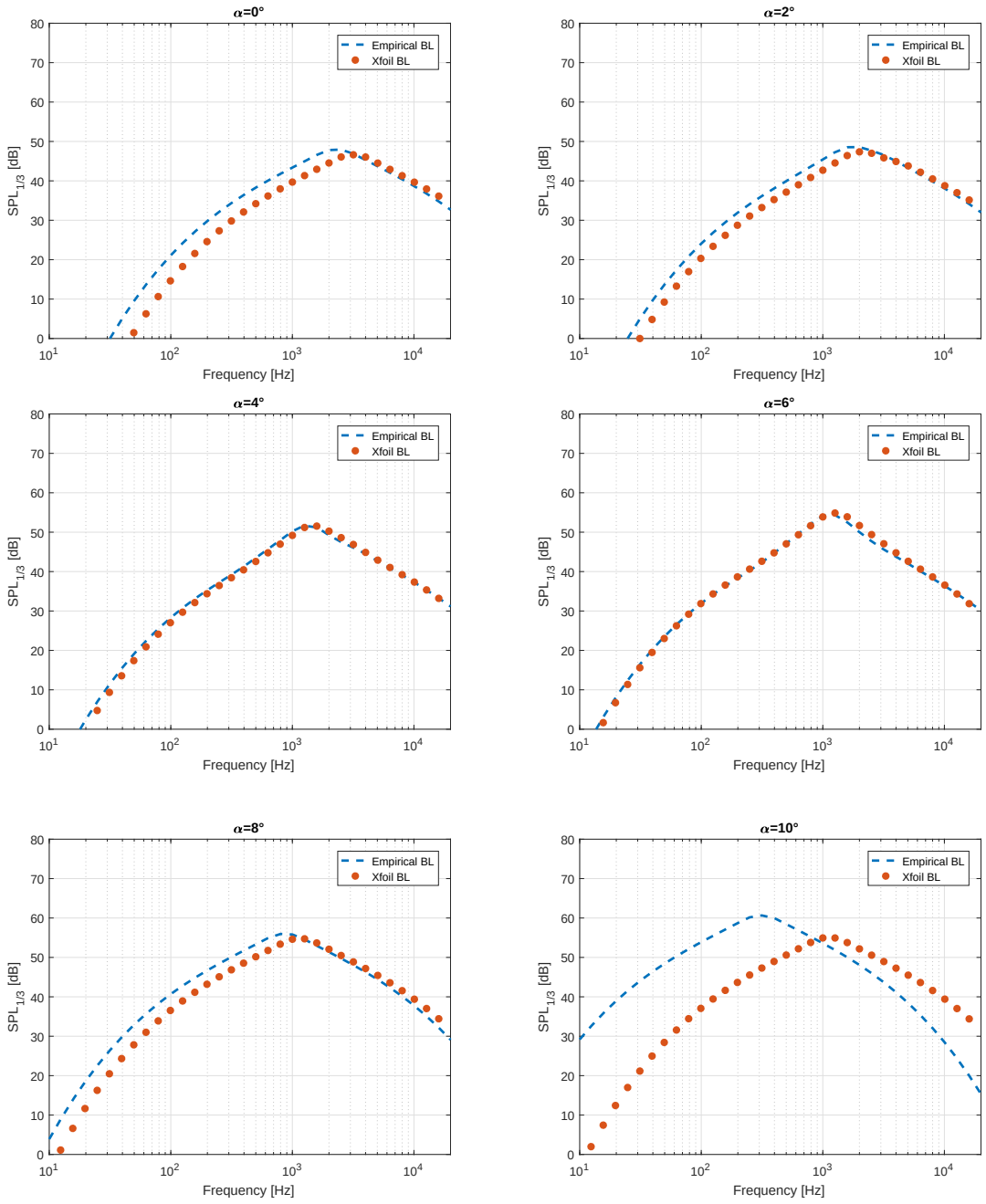

Figure 5.8: SPL comparison for a $NACA0012$, $Chord = 0.3048m$ and $U = 40m/s$, for different BL input: empirical and Xfoil

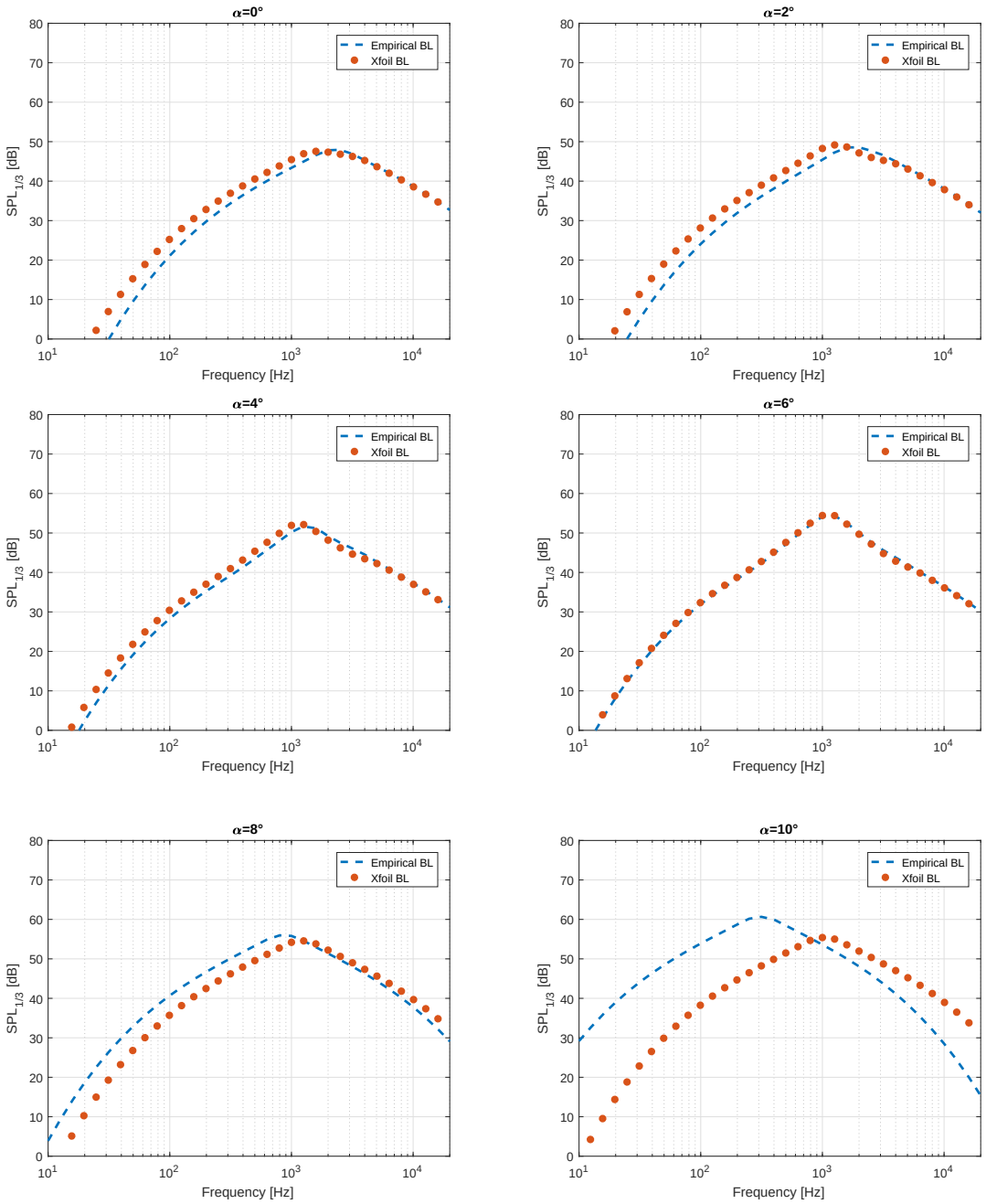

Figure 5.9: SPL comparison for a $DU08-W-210$, $Chord = 0.3048m$ and $U = 40m/s$, for different BL input: empirical and Xfoil

Finally, experiments from *Brooks, Pope, Marcolini* were performed on an anechoic wind tunnel. Flow around the profile in free air and wall bounded is not the same, and wind tunnel corrections had to be taken into account by the authors. For this reason a relation between wind tunnel AoA and equivalent AoA has been established, limiting de facto the maximum angle of attack for which the BPM model

has been fitted; this angle can be considered around $\alpha \approx 8°$. Operating at too high angles of attack may bring to convergence problem of Xfoil or, in case of stalled airfoil, to a totally erroneous consideration of the noise source (TBL-TE noise instead of Stall noise).

5.1.2 TNO model

Validation of TNO have been performed by comparing BPM data with those obtained from various implementation of TNO model. In order to obtain the best approximation possible of real spectra, original BPM set of data have been used, i.e. $NACA0012$, $Chord = 0.3048$, $\Phi = \theta = 90°$, $R = 1.22m$.

Difference between different ϕ_{22} computation was first investigated, in order to assess which model best fits data from BPM: fig 5.10 reports comparison between BPM, TNO with isotropic ϕ_{22} (indicated as TNO-Original) and TNO with anisotropic ϕ_{22} (TNO-Anisotropy), performed at $U = 71.3m/s$. It can be seen that TNO with anisotropy of boundary layer permits to approximate better experimental data from BPM, where original TNO predicts generally lower sound spectra, as already pointed out by other authors [35] [54] [29].

Difference in ϕ_{22} are here reported, for the sake of completeness:

$$\phi_{22}(k_1, k_3, k_e) = \frac{4}{9\pi k_e^2} \frac{\hat{k}_1^2 + \hat{k}_3^2}{(\hat{k}_1^2 + \hat{k}_3^2 + 1)^{\frac{7}{3}}} \tag{5.1}$$

For isotropic spectrum, while:

$$\phi_{22}(k_1, k_3, \Lambda) = \frac{4\Lambda^2 \beta_1 \beta_3}{9\pi} \frac{(\beta_1 \Lambda k_1)^2 + (\beta_3 \Lambda k_3)^2}{((\beta_1 \Lambda k_1)^2 + (\beta_3 \Lambda k_3)^2 + 1)^{\frac{7}{3}}} \tag{5.2}$$

In case of anisotropic boundary layer. for details in theory and implementation the reader can refer to Chapter 3.

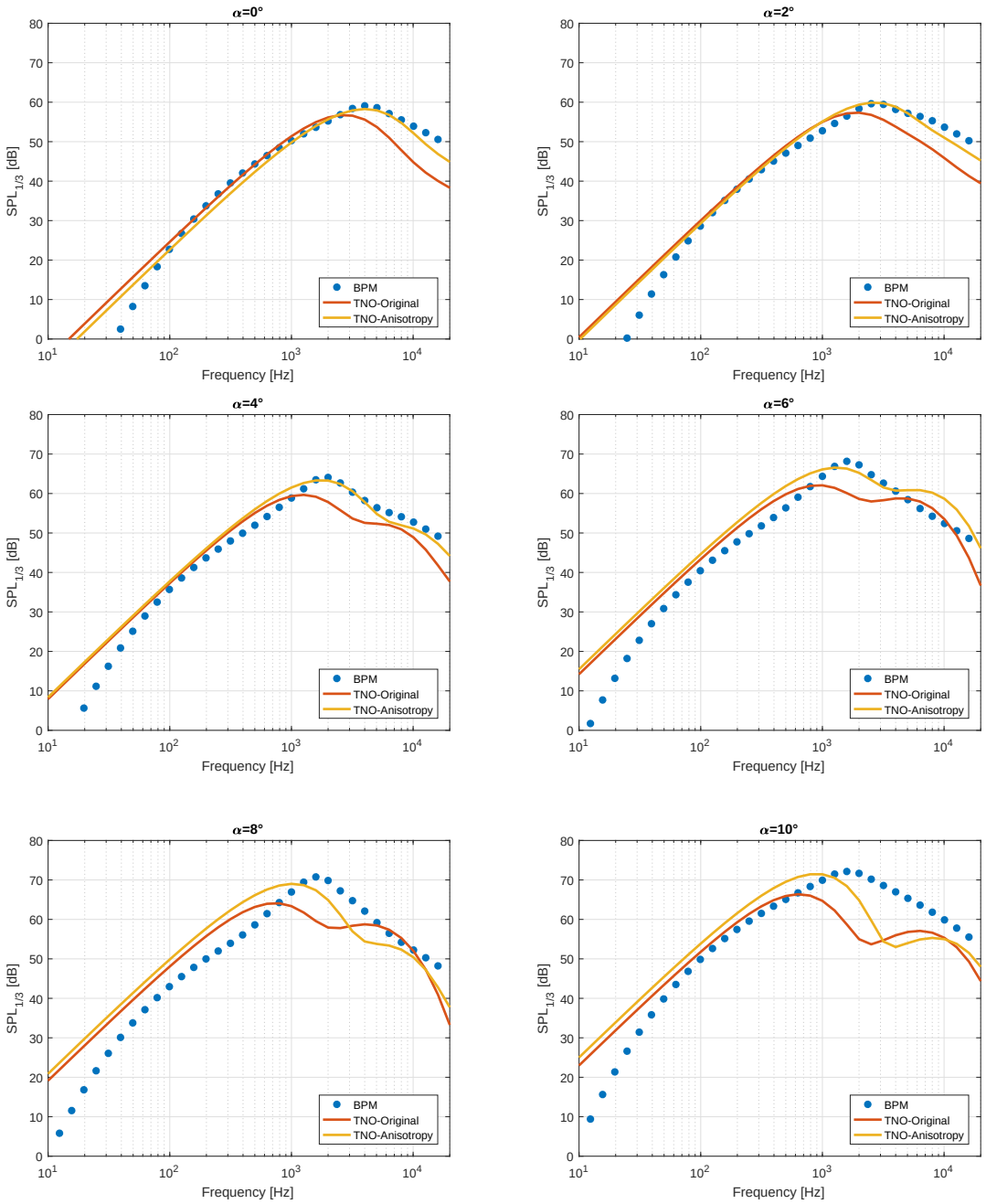

Figure 5.10: SPL comparison between BPM and different ϕ_{22} computation: isotropic (TNO-Original) and anisotropic (TNO-Anisotropy)

All the following comparison will then be performed by using anisotropic boundary layer TNO model. At this point, the following noise models will be compared:

- BPM model
- TNO - Directivity and convectivity based on Howe

- TNO - Directivity and convectivity based on Bertagnolio-DTU
- TNO - NAFNoise implementation

Comparison for $U = 71.3m/s$ at varying angle of attack is reported in fig: 5.11.

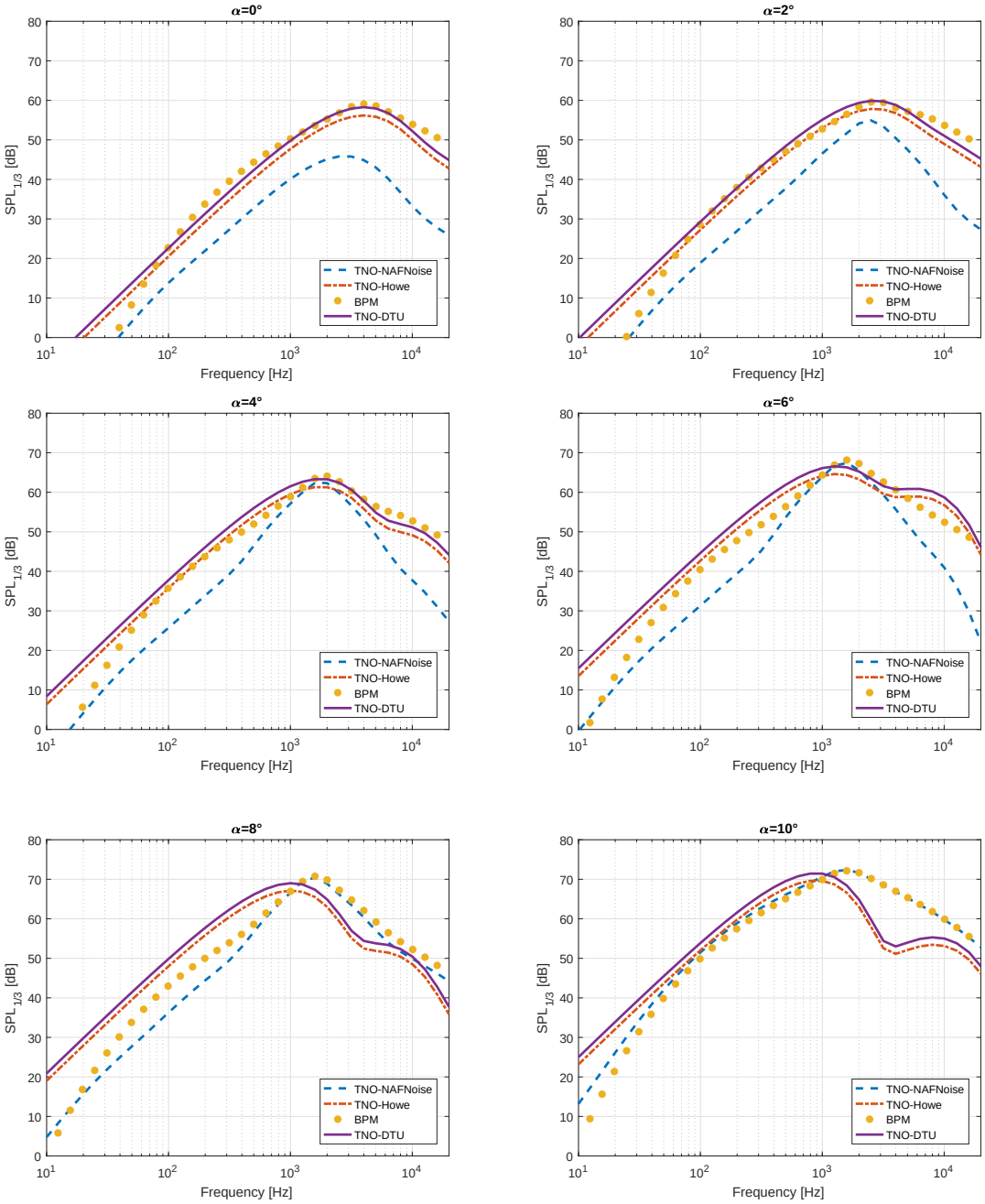

Figure 5.11: SPL comparison between different TNO implementations at varying angle of attack

From the previous graph it may looks like TNO implemented in *NAFNoise* gives very good approximation for higher angles of attack than the TNO models

implemented. The fact that $NAFNoise$ data approximates better the BPM data is due to the fact that the $NAFNoise$ SPL are corrected with a «Separation side TBL» factor which is the same as the one implemented in the BPM and that dominates at higher angles of attack. Furthermore, the TNO model can't compute noise from surfaces with negative friction coefficients: in case of separation, friction coefficient is reset to a value of $10e-4$, while $NAFNnoise$ code computes SPL through BPM.

It is possible to compute $NAFNoise$ TNO without this correction (fig: 5.12), leading to the conclusion that TNO model included in this tool presents some major scaling factor difference.

Difference between $TNO-Howe$ and $TNO-DTU$ are very small: this is due to the fact that those models only differs for the directivity and convective amplification factor implemented and, if the observer is placed perpendicular to the trailing edge, directivities for both models equal one. Difference is then only a scaling factor linked to the convectivity formula used.

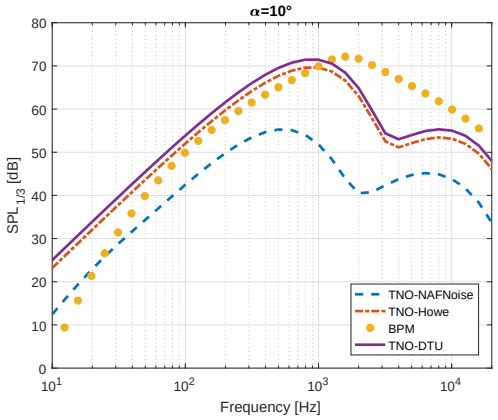

Figure 5.12: SPL comparison between TNO: NAFNoise-TNO without separation correction

It is interesting to observe the agreement of models for different values of asymptotic wind speed, such comparison is shown in fig:5.13 ($\alpha = 0$).

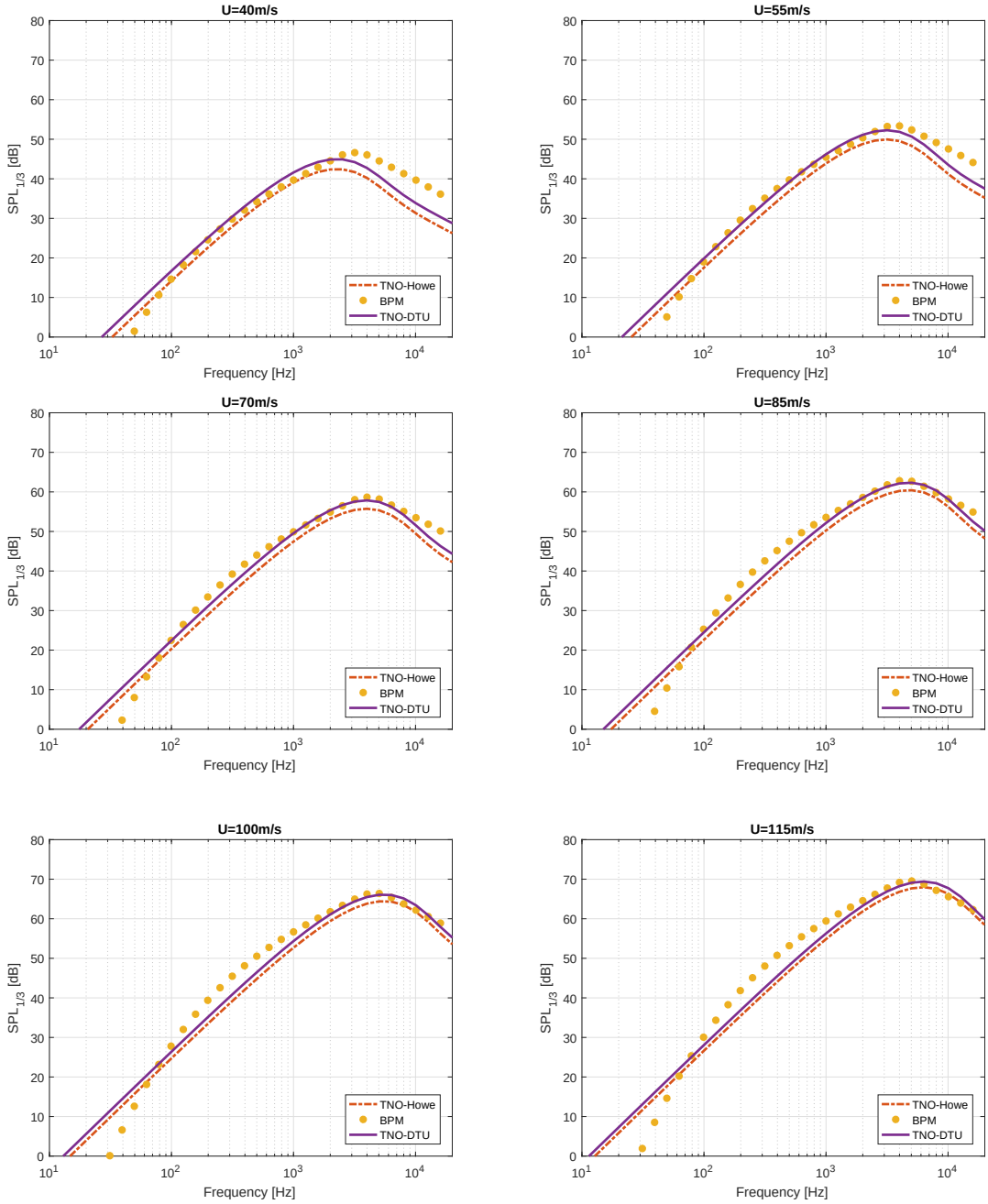

Figure 5.13: SPL comparison between different TNO implementations at varying asymptotic wind speed

The next comparisons evaluate variations of SPL predicted by changing in observer position; Fig: 5.14, 5.15 for varying Φ and Θ angle, respectively, while fig:5.16 for increasing source-observer distance R. It can be seen that while a change in Θ or R doesn't increase divergences of the models, for values of Φ much lower than 90° difference between TNO-Howe and TNO-DTU becomes noticeable, while BPM and

TNO-DTU show the same behavior: this is due to the fact that BPM and TNO-DTU have the same directivity function, which is slightly different from TNO-Howe one.

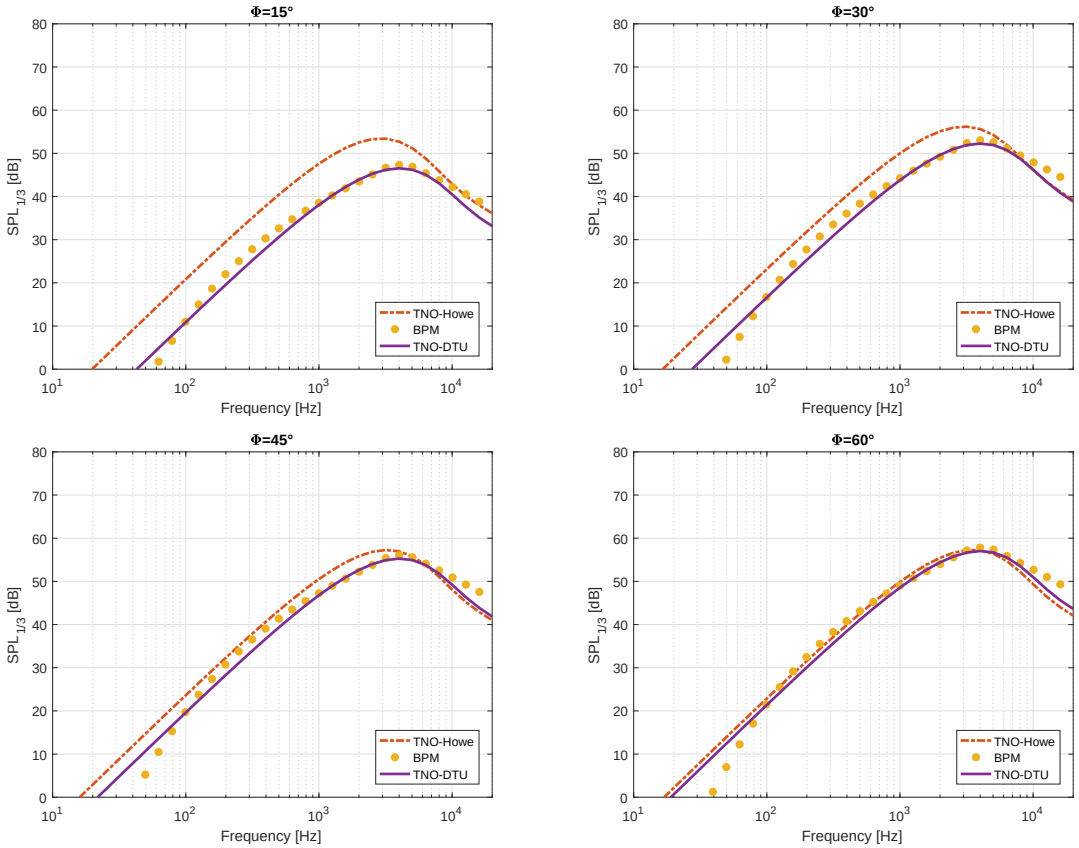

Figure 5.14: SPL comparison between different TNO implementations at varying Φ angle

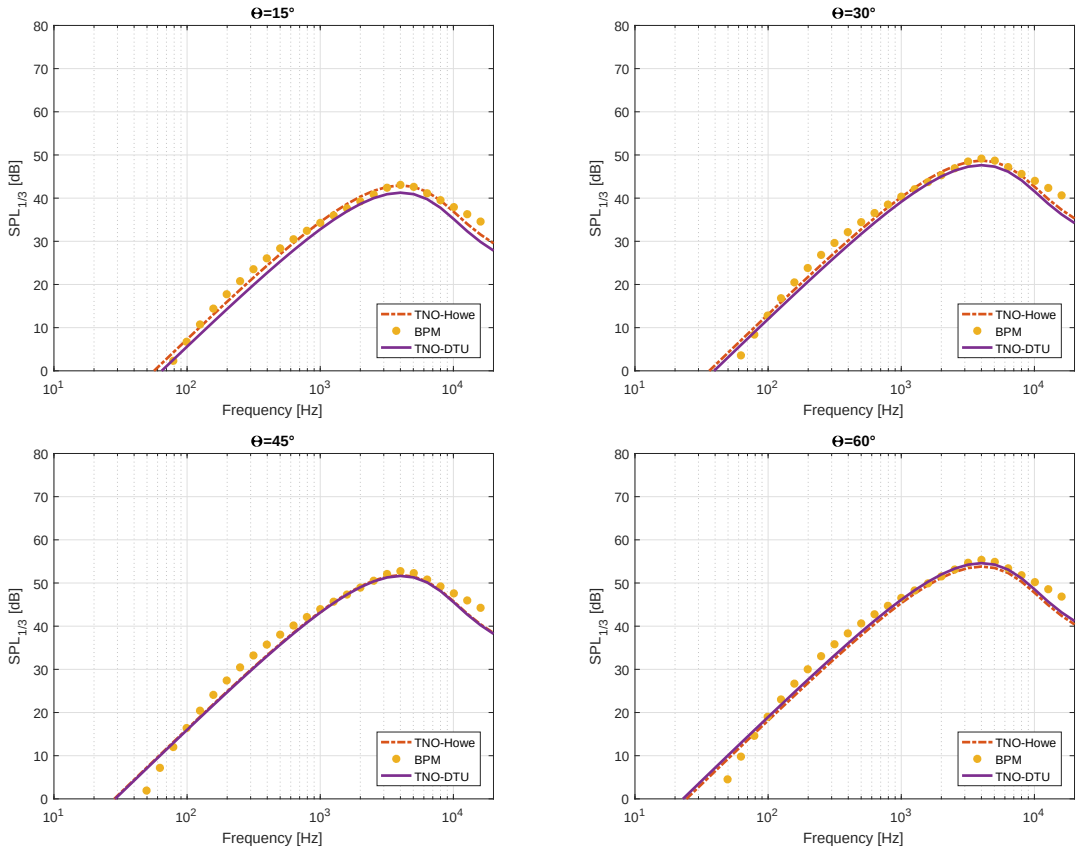

Figure 5.15: SPL comparison between different TNO implementations at varying Θ angle

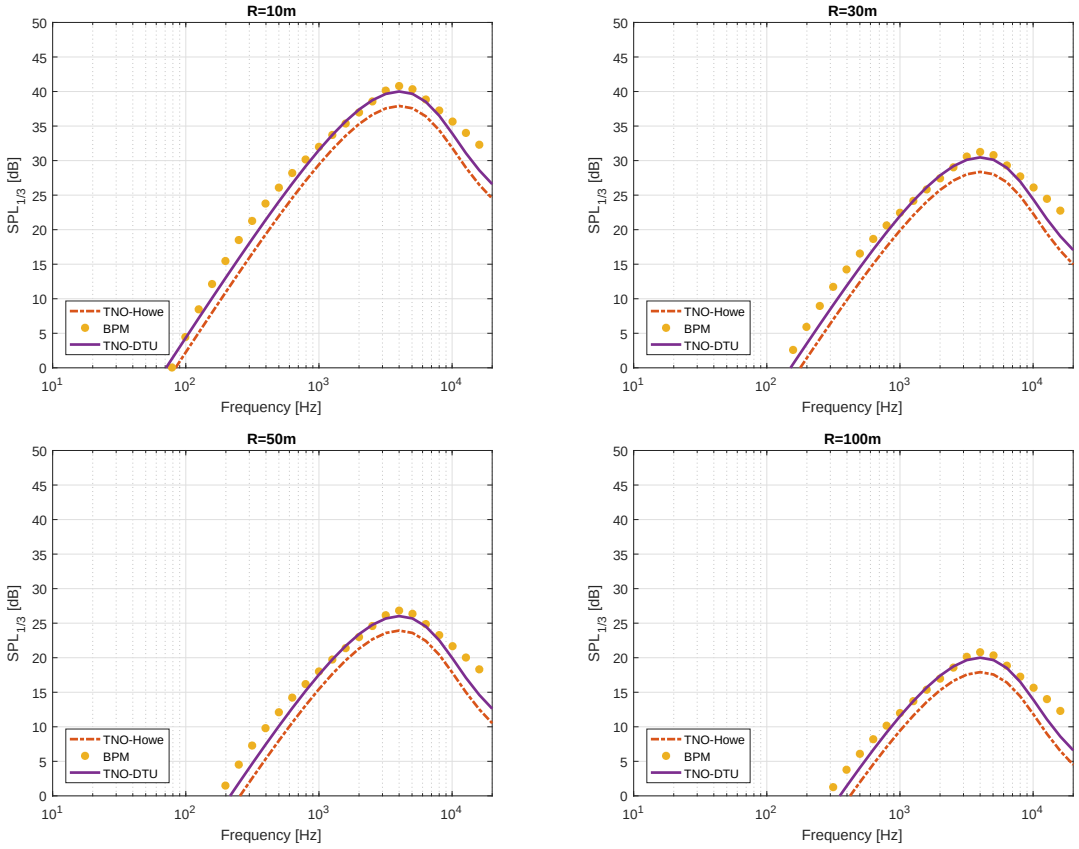

Figure 5.16: SPL comparison between different TNO implementations at varying distance from observer

It is now shown a comparison with data coming from the Third Workshop on Benchmark Problems for Airframe Noise Computations, BANC-III [53]. In this document, trailing edge noise on specific "cases" are computed from several institutes, using different trailing edge noise computation methods (see Tab:5.1). Noise spectra are calculated on an airfoil of $Chord = 0.4m$ and $Span = 1m$, with observer placed perpendicular to the trailing edge at a distance $R = 1m$; two cases have been considered:

- NACA0012, with transition position 0.065/0.065(suction/pressure side), $\alpha = 0°$, $U = 56m/s$
- NACA0012, with transition position 0.065/0.065(suction/pressure side), $\alpha = 4°$, $U = 55m/s$

Comparisons are shown in fig:5.17. It can be seen that the TNO model implemented predicts reasonable results, in line with those obtained by other authors.

Divergences between the model may be due to the boundary layer data given as input, which are computed through Xfoil in the present tool, reducing the accuracy of results. Considerations about the framework in which the tool is going to operate and the need for fast computations make the author evaluate this results as acceptable.

Institution	**Computational method used**
PoliTo	Hybrid RANS/LES (IDDES) coupled with synthetic turbulence LEST (Large-Eddy STimulation) and FWH far field propagation (RANS: CFD++ + SA, QCR terms)
DLR	CAA solver PIANO, coupled with stochastic source model FRPM (Fast Random Particle-Mesh Method), based on RANS statistics (RANS: TAU + SST)
IAG	Simplified theoretical surface pressure model (Blake-TNO-derivative) Rnoise (RANS-based TE noise prediction model) with far field propagation according to Brooks and Hodgson, based on diffraction (RANS: FLOWer + SST)
DTU	Simplified theoretical surface pressure model (Blake-TNO-derivative), with far field propagation according to Brooks and Hodgson, based on diffraction theory (RANS: EllipSys2D + SST)

Table 5.1: Overview of BANCIII contributions

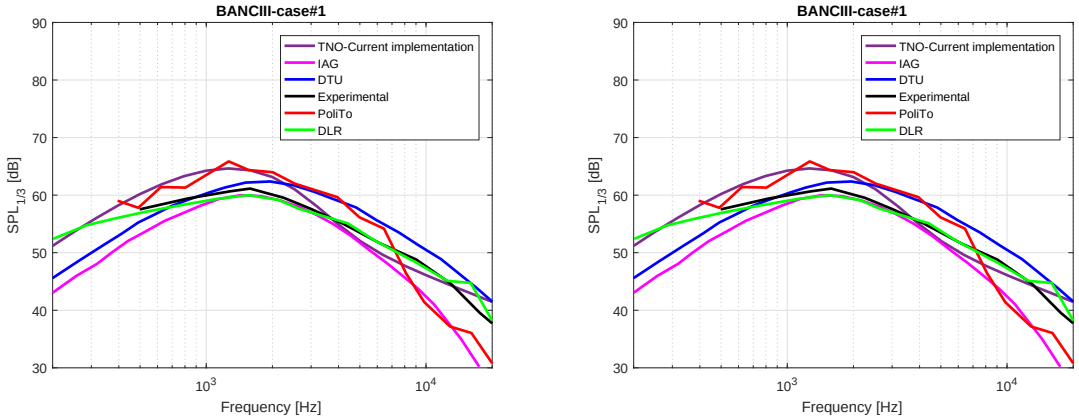

Figure 5.17: BANCIII Trailing edge noise comparison

Comparison of noise spectra from TNO have been also performed for airfoils other than NACA0012, in the original BPM data set (fig: 5.18): it can be seen that thicker airfoils, such as those in use in wind turbine industry, produce higher sound emission, due to the presence of a thicker boundary layer.

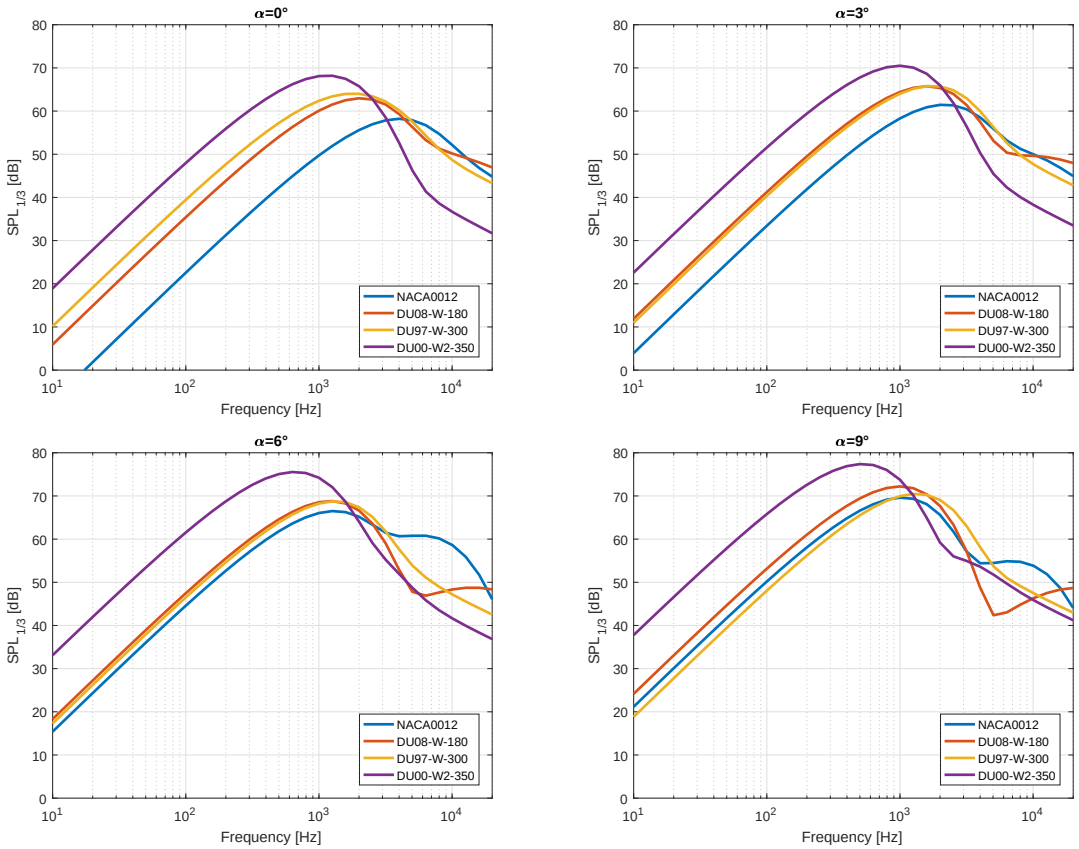

Figure 5.18: SPL comparison for different airfoils, at varying angle of attack

5.1.3 Discrepancies between TNO and BPM

After comparison and validation of the trailing edge noise models described in the previous section, it can be deduced that TNO and BPM model give good accordance, at least on the set of data investigated by *Brooks, Pope and Marcolini* [39]. In this section both BPM and TNO models have been compared in conditions similar to those experienced from a real wind turbine wing section. Comparison is performed on an airfoil DU91-W2-250, starting from the well known dataset of BPM ($U = 71.3m/s$, $\Phi = \Theta = 90°$, $R = 1.22m$, $Chord = 0.3048m$, $Span = 0.45m$, $\alpha = 0°$); sound pressure levels are calculated from this condition, changing one parameter at the time to investigate the effects of such changes on the models spectra.

Comparison in the BPM conditions is shown in fig:5.19. As expected, the models give quite good agreement.

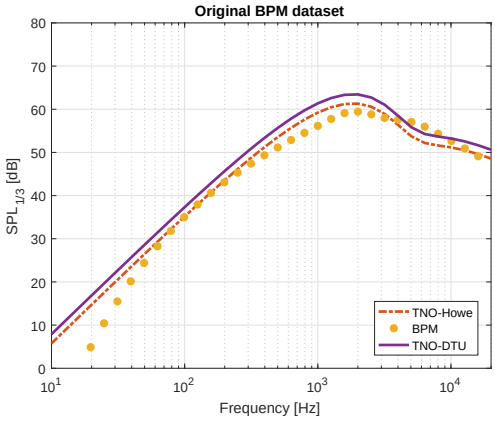

Figure 5.19: SPL comparison in the original BPM dataset: $U = 71.3m/s$, $\Phi = \Theta = 90°$, $R = 1.22m$, $Chord = 0.3048m$, $Span = 0.45m$, $\alpha = 0°$

The first parameter changed has been the distance between source and the observer; this new value was set to $R = 150m$, leaving all the others quantities unchanged (fig:5.20). Changes in observer distance cause a reduction of SPL and, even though this difference remains small under an absolute point of view ($3 - 4dB$), the relative difference between the models becomes evident.

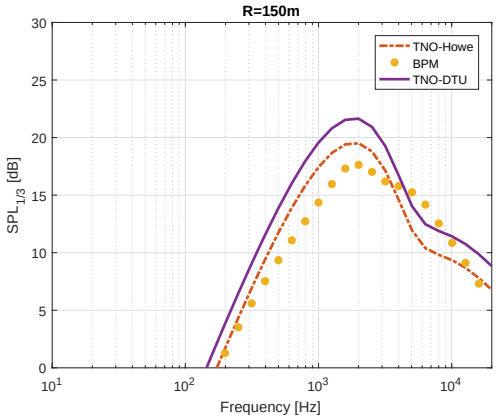

Figure 5.20: SPL comparison at different distance from observer: $U = 71.3m/s$, $\Phi = \Theta = 90°$, $R = 150m$, $Chord = 0.3048m$, $Span = 0.45m$, $\alpha = 0°$

At last, changes in Θ angle and chord length are added in fig: 5.21 and 5.22. Differences between the models becomes important, especially after the change in chord length. This effect will produce BPM spectra much lower than TNO ones when comparing overall noise emissions from wind turbines.

Chord enters both models through boundary layer data, that are adimensionalized with respect to the chord length. More accurate BL data (such as those, for example, obtained through CFD) would probably help improving results. Furthermore, BPM experiments were performed on airfoils with chords around $\approx 0.3m$ with much thinner boundary layer displacement thickness, and the model is then tuned to fit this range of δ^*. It is unclear whether the use of a thicker boundary layer would exceed the boundaries of BPM model.

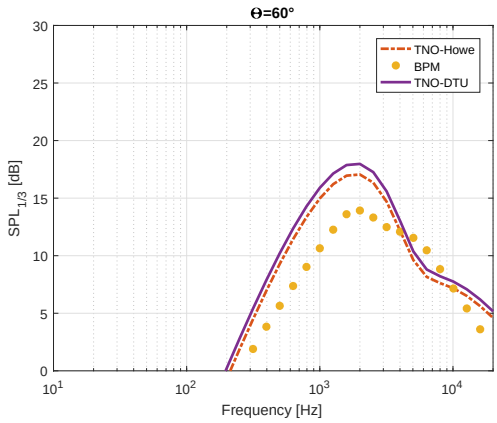

Figure 5.21: SPL comparison with different Θ angle: $U = 71.3m/s$, $\Phi = 90°, \Theta = 60°$, $R = 150m$, $Chord = 0.3048m$, $Span = 0.45m$, $\alpha = 0°$

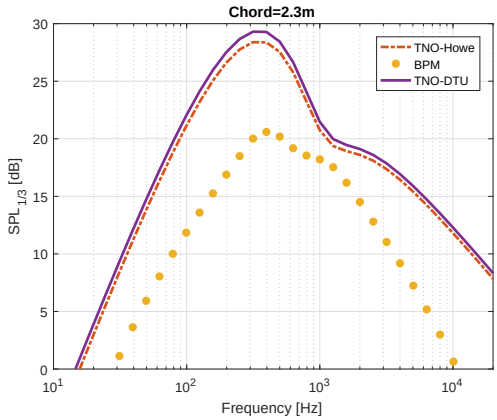

Figure 5.22: SPL comparison with different Chord: $U = 71.3m/s$, $\Phi = 90°, \Theta = 60°$, $R = 150m$, $Chord = 2.3m$, $Span = 0.45m$, $\alpha = 0°$

The last plots are intended to show discrepancies between TNO and BPM models for a NACA0012 and a DU91-W2-250, in a typical wind turbine data set, at low and high angles of attack 5.23.

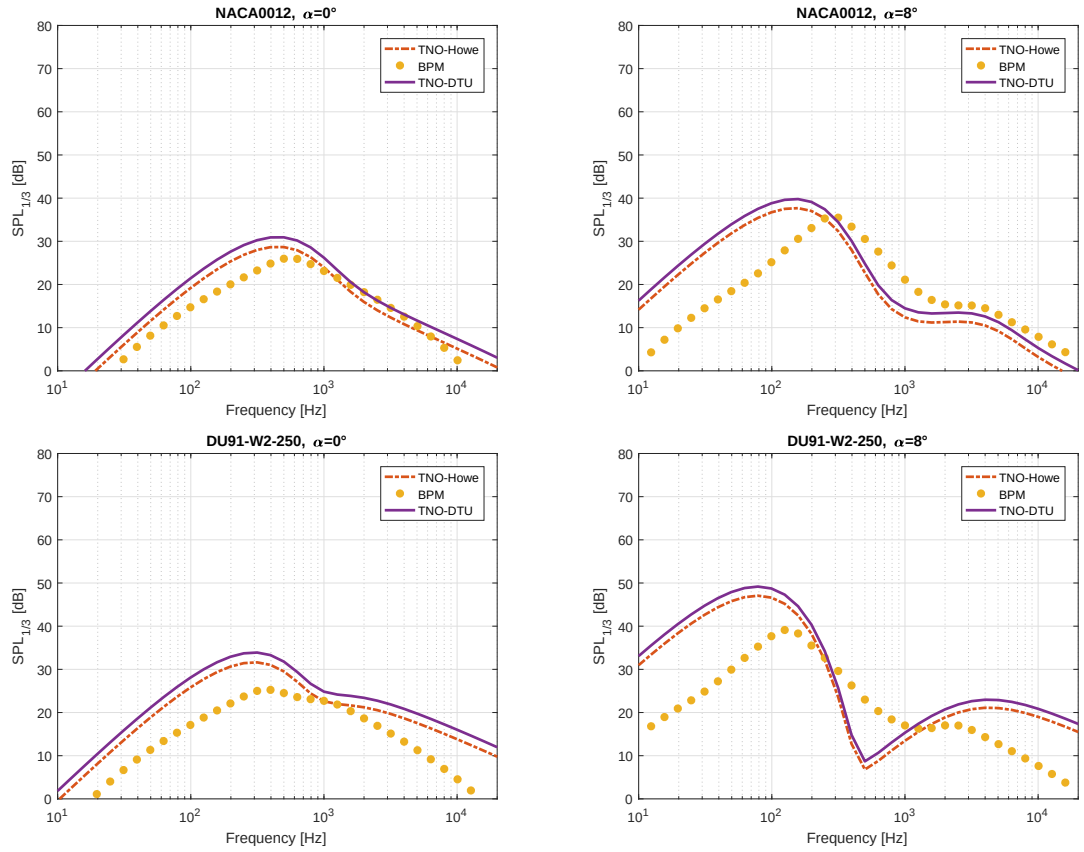

Figure 5.23: SPL comparison for NACA0012 and DU91-W2-250 at two different angles of attack: $U = 60m/s$, $\Phi = 90°, \Theta = 90°$, $R = 150m$, $Chord = 2.3m$, $Span = 1.2m$

5.2 Turbulent Inflow noise

Validation of turbulent inflow model has been performed comparing data from *Amiet* [22] and SPL produced by the current implementation of Amiet model. Differently from BPM, sound pressure levels are given only in one dataset, thus limiting the number of comparisons possible. No Lowson model validation data have been found in the literature, then only a comparison between Amiet and Lowson models is performed to point out differences among the tools.

5.2.1 Amiet model

Experiments conducted by *Fink*[55] are used by *Amiet* to investigate noise emissions from an airfoil in a turbulent stream and relate it to the SPL predicted from the

Amiet model.

Data set of the experiments is reported in Tab:5.2, measurements of turbulence in the test section showed that turbulence properties are well approximated by an isotropic model.

Parameter	**Symbol**	**Units**	**Quantity**
Span	L	m	0.5334
Chord	c	m	0.4572
Angle of attack	α	$^\circ$	0
Turbulent length	L_t	m	0.0317
Distance Source-Observer	R	m	2.1336

Table 5.2: Experimental setting for Amiet model validation

Microphones were located perpendicular to the mid-chord span, so that $\Phi = \Theta = 90°$, turbulence intensity $I = \overline{u^2}/U^2$ is equal to 4.4% at $U = 103ft/s$, and follows approximately the expression:

$$I = CU^{0.2} \tag{5.3}$$

With C constant. It follows that turbulence intensity decreases with increasing airspeed U, as shown in fig:5.24.

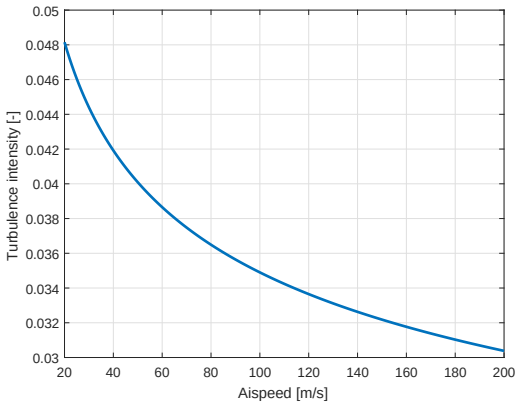

Figure 5.24: Amiet approximation of turbulence intensity as a function of airspeed

Comparison is performed at various Mach numbers, and is reported in fig:5.25; it

can be seen that current implementation matches almost exactly with SPL obtained by Amiet, demonstrating the correct implementation of the model.

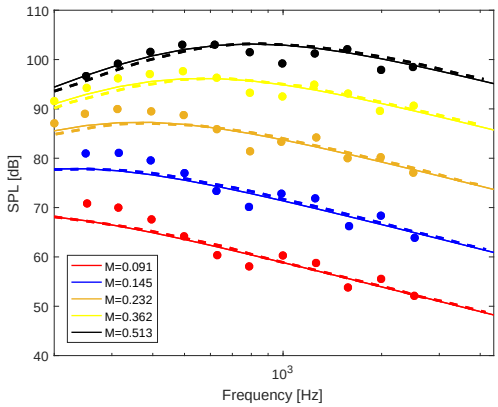

Figure 5.25: SPL comparison for turbulent inflow noise at different Mach numbers: current implementation (continuous line), Amiet implementation (dashed line), experimental data (points)

5.2.2 Comparison among TI models

It is now compared SPL from all turbulent inflow noise models implemented, at varying turbulence intensity I and integral length L_t; airspeed has been set to $U = 60m/s$, all other data are reported in tab:5.2.

Plots are shown in fig:5.26,5.27; the models compared are the following:

- TI Full implementation: obtained through the computation of power spectral density of far field noise for different adimensional pressure jump function g (as reported in section 3.2.1)
- TI Amiet approximated: computation of sound pressure levels for "low" and "high" frequency through approximated formulas, as reported by *Amiet-Paterson*[23]
- TI Lowson
- TI Amiet-Lowson: computation of high frequency SPL as reported by Amiet, and low frequency approximation obtained through Lowson (details in section 3.2.1)

In order to give a clearer idea of the entity of noise emissions due to turbulent inflow, trailing edge noise obtained through TNO-DTU has been added to the comparisons.

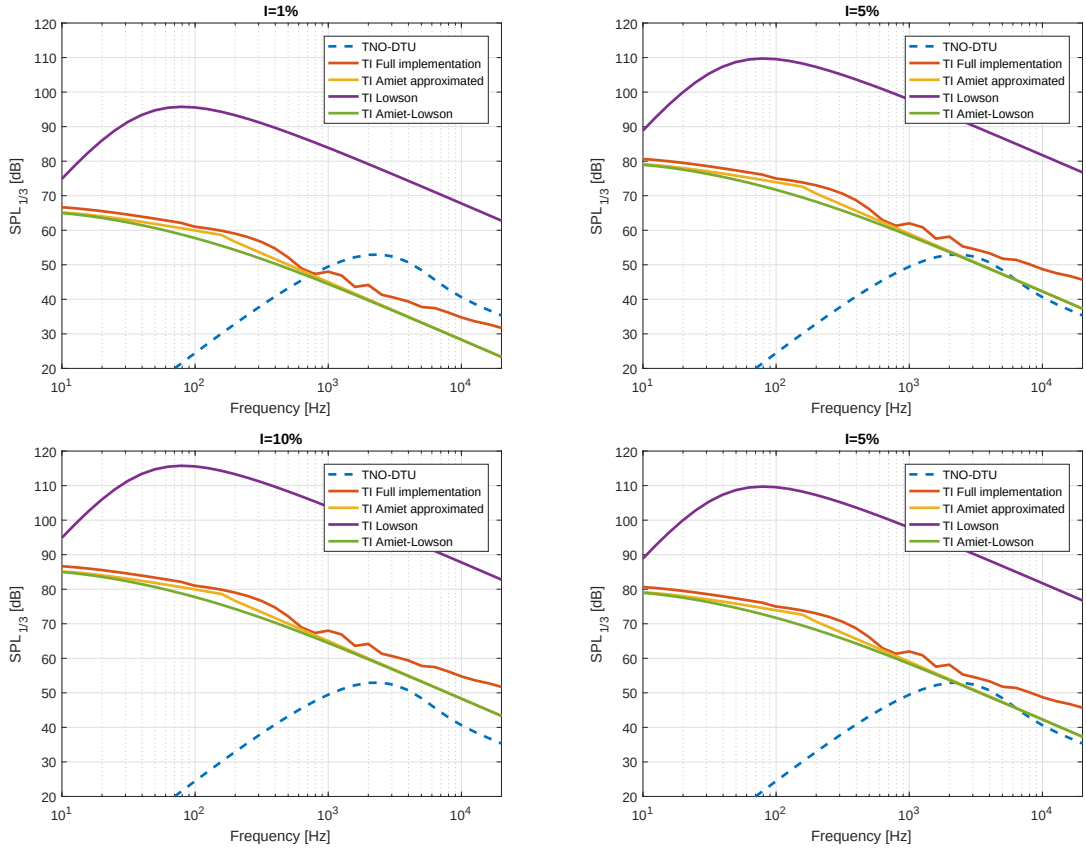

Figure 5.26: SPL comparison among different TI models at varying turbulence intensity

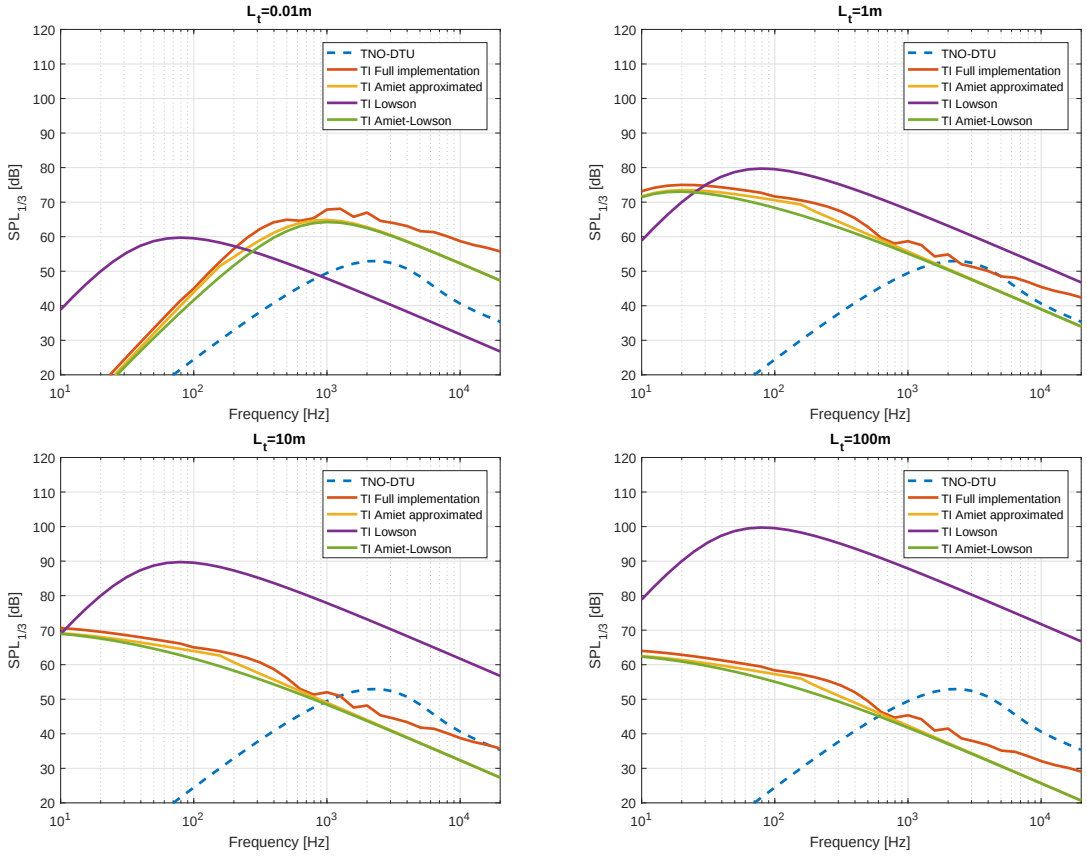

Figure 5.27: SPL comparison among different TI models at varying integral length

Increasing turbulence intensity I increases TI noise for all the spectra, while increasing turbulent integral length L_t causes a reduction of SPL for all the "Amiet based" models and a big increase of sound pressure level for the Lowson model. Divergence in behaviors is due to the different definition of wavenumber K used for the computation of isotropic velocity spectrum.

Amiet model makes use of a wavenumber adimensionalized with respect of the dimension of mean eddies k_e (eq:3.116):

$$\hat{K}_1 = \frac{2\pi f}{U_{inf} k_e} \tag{5.4}$$

While Lowson model defines wavenumber K as (eq:3.2.2):

$$K = \frac{\pi f c}{U_{inf}} \tag{5.5}$$

Finally, it can be seen that Lowson model predicts very high values of turbulent

inflow noise, clearly dominating the trailing edge noise spectrum. In case of prediction of noise emission from a whole wind turbine, this fact would lead to dominating turbulent inflow: this fact was already observed by *Moriarty*[26]. It is then unclear whether Lowson model constitutes a valid tool for turbulent inflow noise assessment or not, at least with the current definition of turbulence intensity and integral lengthscale of the turbulence.

Chapter 6

Noise Analysis Results

In the present chapter noise spectra from a whole model of wind turbine are computed under a great number of condition, in order to assess robustness of the code and coherence of results. The model, developed at the Wind Energy Institute of the Technische Universität München (TUM), is a 3 bladed wind turbine of IEC Class 3A. Description of the wind turbine model (named "TUM3.6MW") is given in tab 6.1:

Rotor Orientation	Upwind
Control	Variable speed collective pitch
Rated Mechanical Power	$3.6MW$
Rotor Diameter	$130m$
Hub Height	$110m$
Cut In Wind Speed	$3m/s$
Cut Out Wind Speed	$25m/s$
Omega Rated	$11.75rpm$
Wind Speed Rated	$9.59m/s$
Max Tip Speed	$80m/s$

Table 6.1: Technical characteristics of the TUM3.6MW model

A first simulation allowed computation of static curves of the wind turbine subjected to steady wind speed. Plots with mechanical power, rotational speed and pitch angle as a function of wind speed are reported in fig:6.1, 6.2, 6.3.

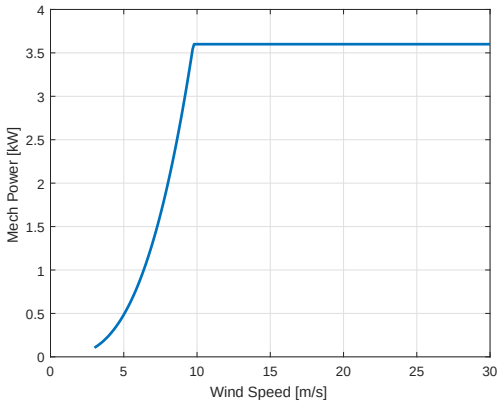

Figure 6.1: TUM3.6MW static curve: Mechanical Power vs Wind Speed

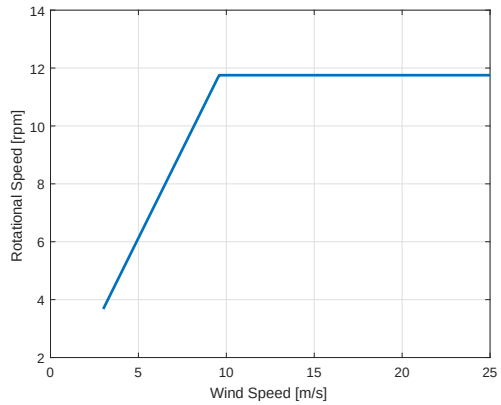

Figure 6.2: TUM3.6MW static curve: Rotational Speed vs Wind Speed

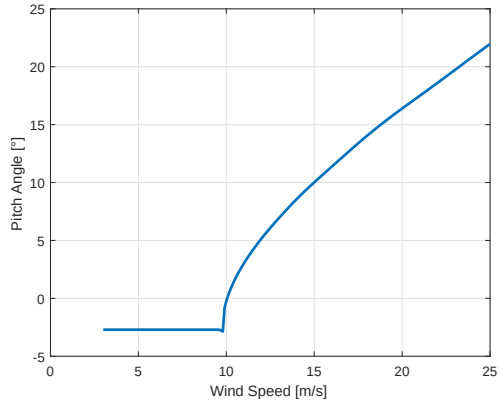

Figure 6.3: TUM3.6MW static curve: Pitch Angle vs Wind Speed

It must be remarked that for both turbulent inflow and trailing edge noise emis-

sions strongly depend on relative wind speed along the blade. Once length of the blade is fixed, maximum wing tip speed imposes the rotational speed of the wind turbine, which is then one of the main parameters able to affect relative wind speed on the blade and thus noise production.

6.1 Sensitivity Analysis

At first, noise analysis module was tested in order to assess coherence and sensitivity of results at varying input data. Considering the large number of parameters the code is able to take as input and the fact that each parameter has an influence of the computation time, this step has allowed determination of a dataset able to give robust results without increasing excessively execution time.

Four are the parameters here investigated:

- Observation window length
- Observation frequency
- Portion of blade emitting noise
- Number of sensors along the blade

Each of those quantity will be now discussed in detail. Dynamic simulation with turbulent wind speed at $15m/s$ (mean wind speed) together with TNO-DTU model for TBL-TE and Amiet-Lowson model for TI noise are used here to compute all the noise analysis of the present section. Observer is located downwind, at a distance of $H + D/2$ from the tower, as reported by IEC61400-11[2].

Cp-Max aeroelastic simulations are usually performed on a simulation time of $630s$; it would be unnecessary to compute noise spectra on the same time domain of the aeroelastic simulation: observation time window must be long enough to avoid noise peaks (or reductions) due to changes of rotational speed under the effect of turbulent wind but not too long to keep computation time reasonable.

Effects of observation window length on Total SPL are reported in fig: 6.4, where differences on noise emissions become noticeable only if very short periods are chosen. Total SPL are azimuthally averaged so as a rule of thumb it can be said

that a good observation window should cover at least one whole revolution period of the wind turbine.

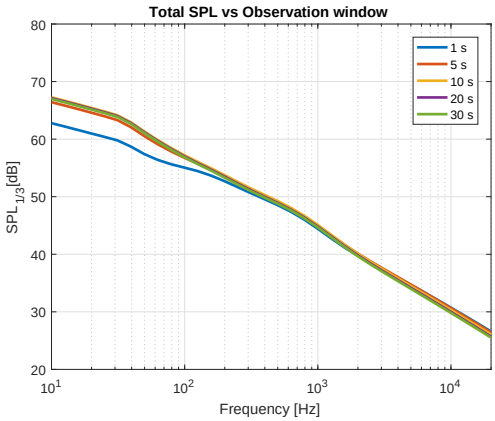

Figure 6.4: Effect of observation window on total sound pressure level

Observation window length has then been set to $20s$ for the next computations.

The following parameter analyzed has been the observation frequency, identified by the parameter $f_{analysis}$ already described in section 4.3. It can be seen in fig:6.5 that averaged total SPL are almost not affected by a change in this parameter.

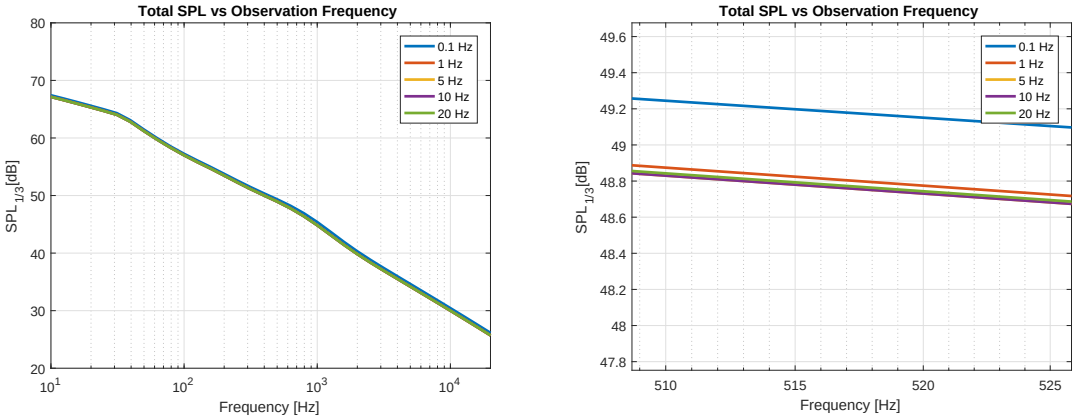

Figure 6.5: Effect of observation frequency on total sound pressure level (on the left), and magnification (on the right)

It is interesting to analyze the temporal history of sound pressure level for the case $f_{analysis} = 20Hz$ and to investigate its frequency content; as it is possible to expect, values of sound pressure levels are related to the rotational regime of the wind turbine. Plots of rotor speed and maximum SPL value time histories are shown

in fig:6.6 6.7: it is clear that a decreasing trend in rotational speed leads to a similar behavior in SPL emissions.

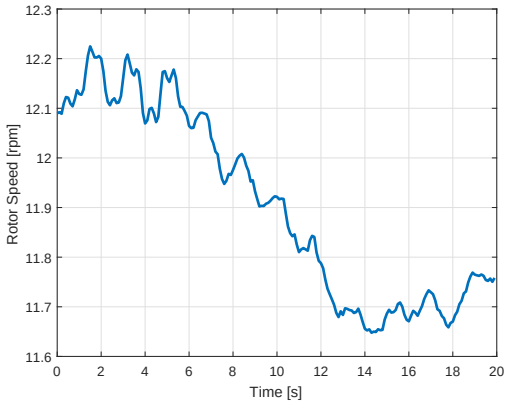

Figure 6.6: Rotor speed time history

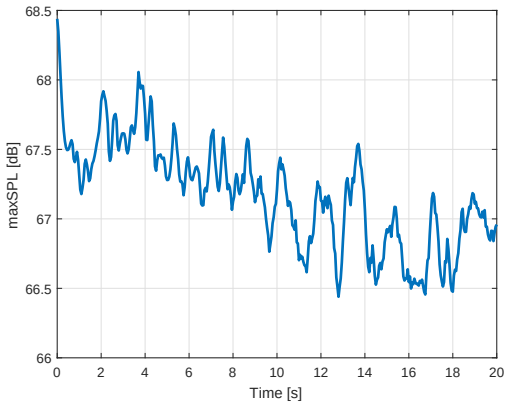

Figure 6.7: maxSPL time history

The average rotor speed can be computed and is equal to $\Omega = 11.905 rpm$, and 3p frequency is then equal to $f \approx 0.6 Hz$. Transformation of maxSPL through FFT and manipulation to obtain single sided spectra leads to fig:6.8; the current tool is then able to detect periodicity of the SPL due to passing blades, at least in case of high sampling frequency of observation period.

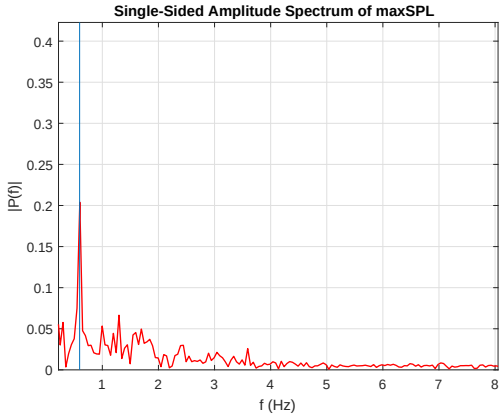

Figure 6.8: Amplitude of maxSPL spectrum vs Frequency

The same frequency analysis have been performed also for decreasing frequencies (fig:6.9), showing that the same behavior is achieved also at lower frequencies, except for the case at $1Hz$ where the frequency discretization is not small enough to allow peaks in $\approx 0.6Hz$

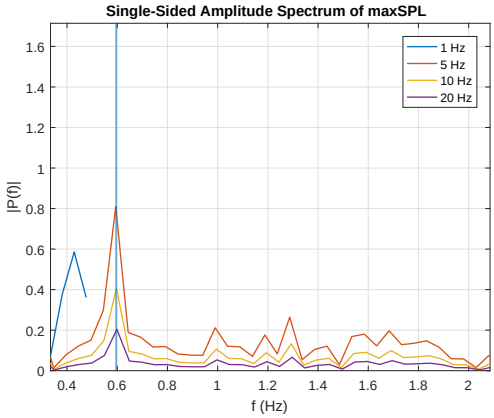

Figure 6.9: Comparison between maxSPL spectra for different $f_{analysis}$

After sensitivity analysis of observation parameters, variations of SPL due to different blade sensors positioning is investigated. As already mentioned, sensors are used to retrieve informations about loads, positions, aerodynamic properties, and other quantities along the blade; distribution of sensors along the blade is then necessary to perform noise analysis. Several configurations of blade coverage have been tested while keeping the number of sensors constant (equal to 40); outer portion of blade is considered to be the main contributor to noise [56], and this fact is verified

also by the current aeroacoustic module. Blade tip has been excluded in order to avoid numerical problem due to discontinuities, but tip noise is generally considered as a minor noise contributor to overall sound emissions.

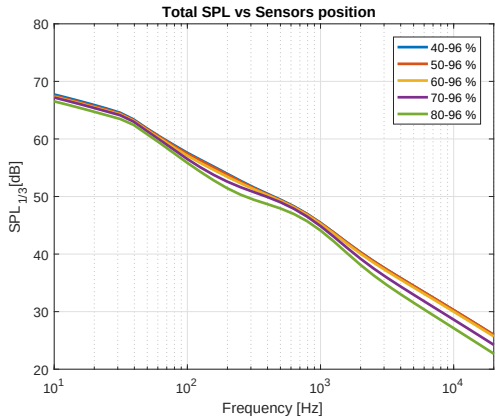

Figure 6.10: Comparison between total SPL at different blade sensor coverage: outer bound fixed to 96% and inner bound progressively reduced

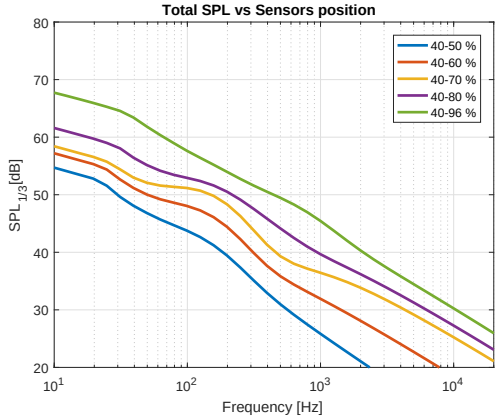

Figure 6.11: Comparison between total SPL at different blade sensor coverage: inner bound fixed to 40% and outer bound progressively increased

From the graphs above, it is possible to deduce that the terminal part of the blade is a main contributor to SPL and cannot be excluded from the computation (due to the high relative wind speed), while curves overlap when considering blade portions "close" to the blade root: a good trade off is obtained by considering only half of the blade (from 50% to 96%).

Finally, effect of different number of sensors have been analyzed in fig:6.12. Noise

spectra are very insensitive to this parameter while computational time increases dramatically; it is then good practice to keep this value as low as possible.

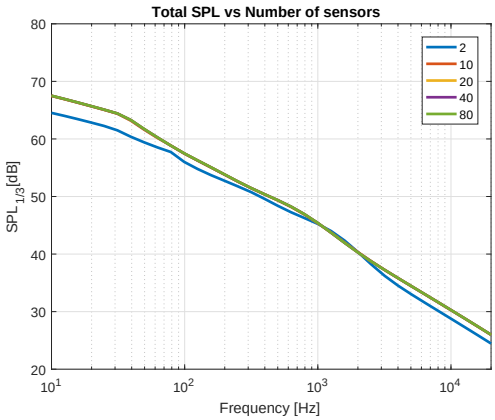

Figure 6.12: Comparison between total SPL at different number of sensors

6.2 Noise Spectra

This section reports noise spectra computations on the "TUM3.6MW" model. All the noise simulations have been performed under an "optimal" data set, emerged from the previous section (6.2). All the noise source models implemented are tested at different wind speed, and their results compared.

Observation window length	$20s$
Observation frequency	$2Hz$
Sensors position	$50 - 96\%$
Number of sensors	10

Table 6.2: Numerical dataset used for noise spectra computations

The next figure (6.13) presents sound pressure levels obtained from all the models implemented, turbulent boundary layer - trailing edge noise and turbulent inflow noise, at different wind speeds . It can be seen that "TI Amiet-Lowson" and "TI Amiet-Approximated" are exactly the same at higher frequencies and differs only in the lower part of the spectrum, due to the different low frequency approximation. As already stated out in a previous chapter, "TI Lowson" predicts values of noise spectra clearly dominating for all the wind speeds. It is interesting to note that,

in case of whole wind turbine comparison, differences between TNO Models and BPM have emerged, as it was possible to expect from the considerations done in section 5.1.3.

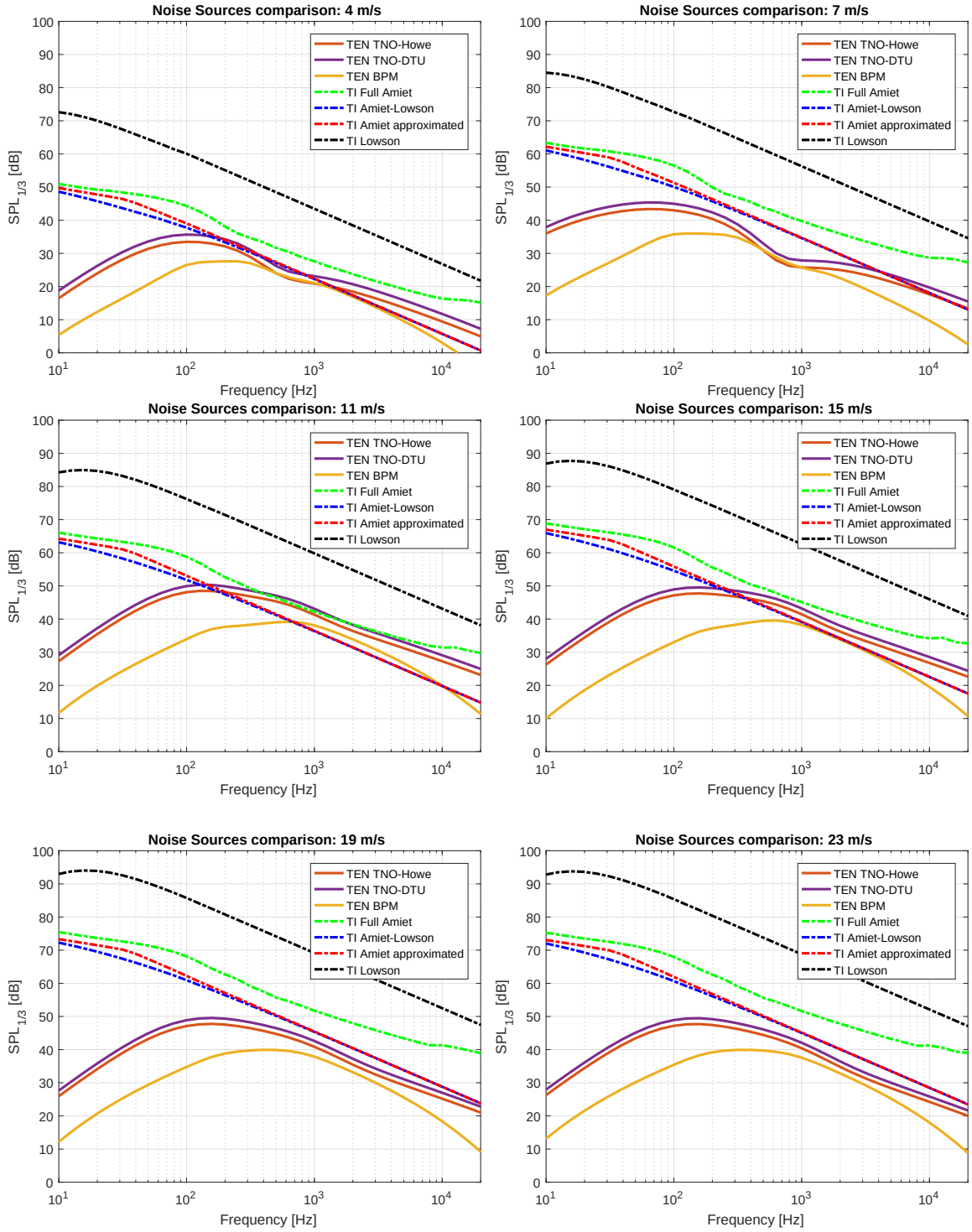

Figure 6.13: Noise Spectra prediction for different source models computed at various wind speed: TBL-TE (continuous) and TI (dashed)

Generally, it can be seen that sound pressure levels keep increasing for all the turbulent inflow models, as a consequence of the fact that they only feed on the relative wind speed along the blade, neglecting incidence or any airfoil shape. On the other side, trailing edge noise increases only up to $\approx 10 - 11 m/s$, which is the wind speed rated: from fig:6.2 it is clear that rotor speed does not increase after this point. At higher wind speeds rotational speed is kept constant by a decrease in the angles of attack along the blades; this effect keeps noise emissions due to TBL-TE approximately constant.

Total sound pressure level is showed in fig:6.14, together with its TBL-TE and TI contributors: in order to compute total spectra, "TNO-DTU" model has been chosen to evaluate TBL-TE noise, while "Amiet-Approximated" computes turbulent inflow. Trailing edge noise is the dominating source in the "high" frequency range of the spectrum while turbulent inflow tends to dominate the lower frequency range; same results were obtained also by other authors ([15][38][27]). At very high wind speed turbulent inflow effects are to dominate the whole frequency spectrum, because of the already mentioned fact that turbulent inflow noise increases for increasing wind speeds, differently from TBL-TE. It is unclear whether this fact is about to happen in practice or not.

In fig 6.15 and 6.16 TBL-TE, TI and Total noise spectra are plotted at increasing wind speed. Again, it is possible to see that TBL-TE noise does not increase after the rated wind speed, and Total SPL above this wind speed differs mainly in the lower part of the spectrum, where TI dominates.

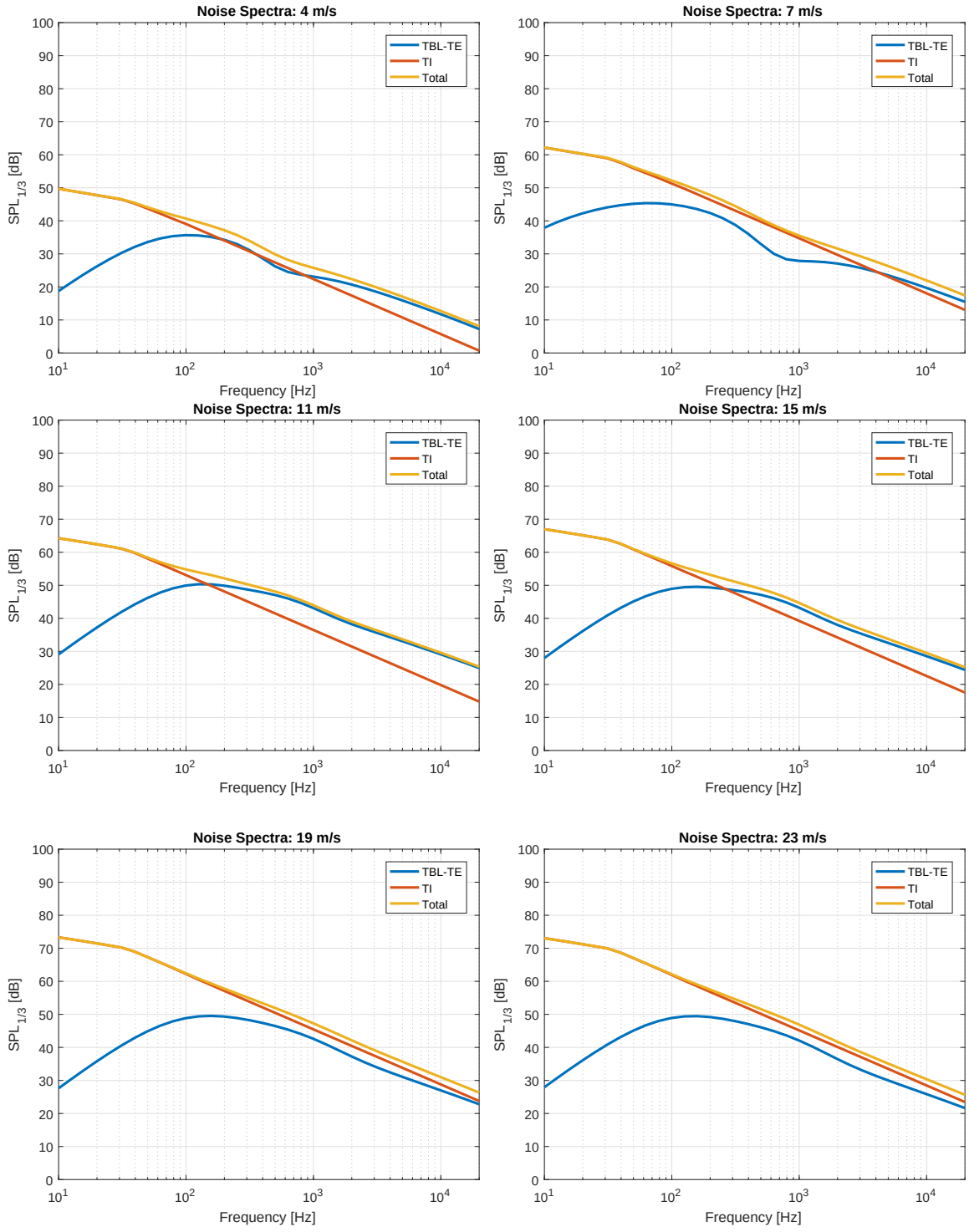

Figure 6.14: SPL comparison between different TNO implementations at varying asymptotic wind speed

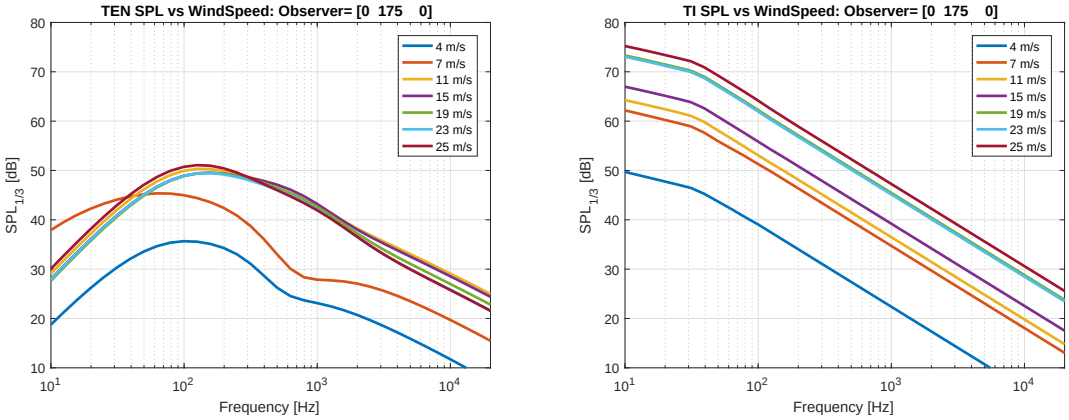

Figure 6.15: SPL of TBL-TE and TI at varying wind speed

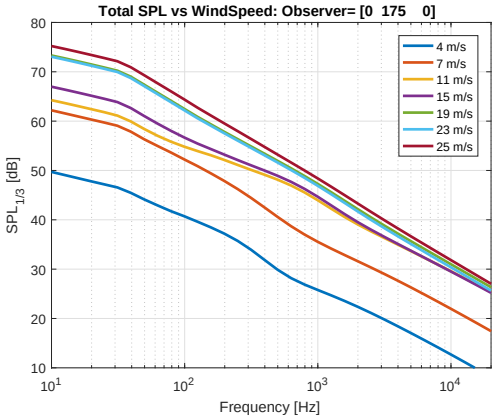

Figure 6.16: Total SPL at varying wind speed

A-Weighted SPL shows the effective spectra perceived by a human observer; considering the very bad sensitivity of human ear at low frequencies is can be seen (Fig: 6.17) that even if the highest Total SPL are produced by the turbulent inflow, the audible SPL spectrum would be much lower and focused on a mid-frequency range. Fig: 6.18 reports OverAll SPL (OASPL) for both the non-weighted and A-weighted noise spectra, for increasing asymptotic wind speed.

Finally, OASPL is computed for an array of microphones placed around the wind turbine and for increasing distance from the WT, in order to assess prediction of in-plane noise reduction (as reported by *Oerlemans* [57]) and decreasing of noise emissions at increasing distance from the tower. Position of observers and relative SPL are plotted in fig 6.19: directivity analysis is performed with a constant spacing

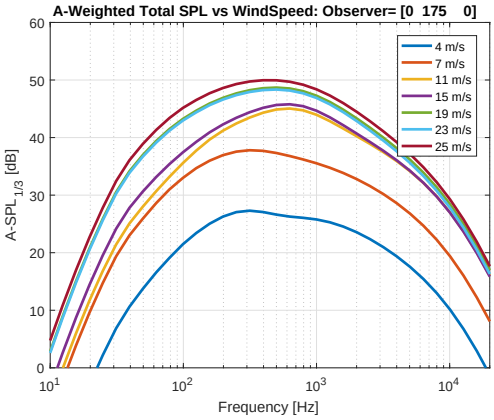

Figure 6.17: A-Weighted SPL at varying wind speed

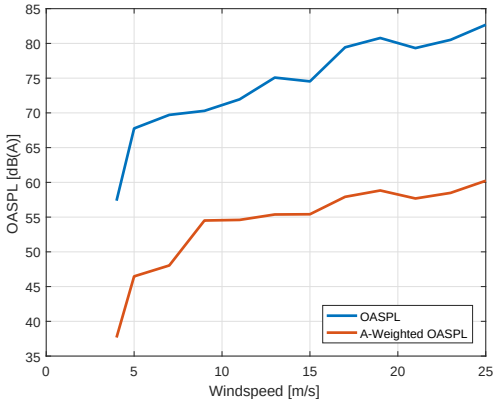

Figure 6.18: OASPL for Total SPL and A-Weighted Total SPl as a function of wind speed

of 30° between the observers, while for the second analysis microphones are located at distances equal to $0.3, 0.5, 1, 2, 5, 10$ times the IEC distance (which is $175m$ for the present wind turbine).

The present tool is then able to reproduce the noise trend around a WT, with decreasing emissions for in-plane observers; reduction of SPLs at increasing distance from the rotor is also observed. In real cases, noise emissions are subject to absorption by atmosphere, reflections from the ground and refraction from wind, effects that are not yet included in the aeroacoustic module.

To summarize, the tool developed predicts reasonable spectra and is able to reproduce the right trends expected from wind turbines such as: importance of the outer region of the blade, dominance of TI noise for the low frequency range, de-

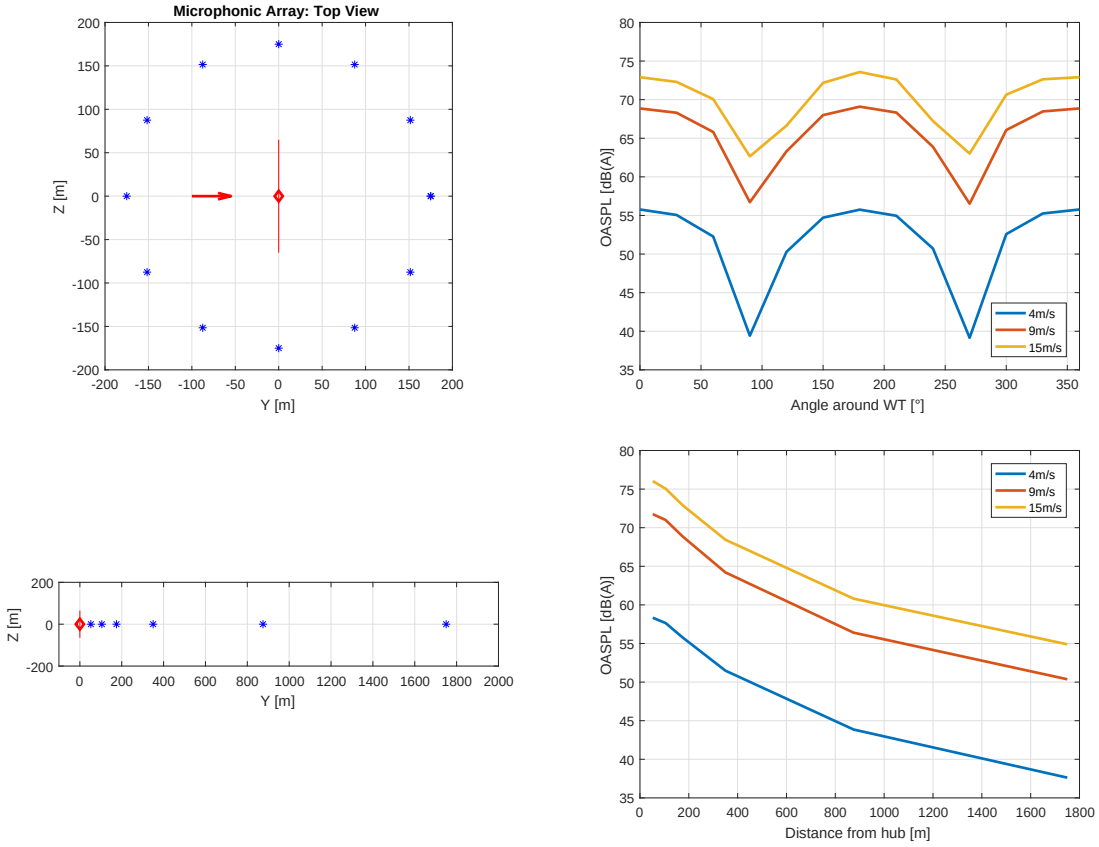

Figure 6.19: Position of Microphones (on the left) and relative Noise emissions (on the right). Arrow indicates direction of mean flow

pendence of noise emissions on the rotor speed, decreasing of sound pressure level for in-plane and increasingly distant observers.

At last, is must be said that validation of the tool would require detailed description of the wind turbine geometry and of the operations conditions, together with a detailed experimental noise analysis campaign. While it has been possible to find works reporting noise emissions, wind turbine details are usually not available, due to restriction of data. This fact has limited validation possibility of the present tool that, even though it produces "qualitatively" correct spectra, nothing can be said on the "quantitative" accuracy of results.

Chapter 7

Conclusions and future developments

The present work was focused on developing an aeroacoustic tool for wind turbine noise prediction that could work within the framework in use at Politecnico di Milano and Technische Universität München for wind turbine simulation and design. The tool has been included as an additional noise analysis module that could work separately from the rest of the code. Frequency based methods for turbulent inflow and turbulent boundary layer - trailing edge noise have been studied, being the sources affecting wind turbine noise the most. For both the noise sources various models found in the literature have been implemented and their results compared. BPM and TNO are the models used to predict turbulent boundary layer - trailing edge noise while *Amiet* and *Lowson* compute turbulent inflow; boundary layer data are given by the software $Xfoil$.

Correct implementation of the models have been performed through comparisons with experimental results and by making use of $NREL's$ code $NAFNoise$. Comparison between BPM and TNO has shown good agreement of models when the original dataset in which BPM has been experimentally verified is used, but discrepancies have emerged when very different conditions are investigated. Those differences have been attributed to limitation in applicability range of BPM due to the empirical nature of the model, tuned on a restricted set of data. More accurate boundary layer data may help improve the results. Comparisons between *Amiet* and

Lowson model have shown very high prediction of sound pressure levels given by the latter compared to the formed, a fact already observed by other authors. More specifically, derivation of *Lowson* model is unclear and improper use of the model, i.e. changing of equations or wrong units of measure adoption has been found in the literature. In view of the above, it is unclear whether *Lowson* model can be considered as an accurate model for turbulent inflow noise prediction.

The noise prediction module developed takes as input detailed WT geometrical and operational data in order to assess noise spectra. The tool have been extensively tested on a 3.6MW wind turbine model and reasonable results, as well as correct trends are predicted. Turbulent inflow seems to be the main noise source at low frequency, while trailing edge noise is more important in a higher range of frequencies (in which human ear appear to be more sensitive, according to A-weighting curve). in-plane noise reduction and dependence of the noise on rotational speed is also predicted by the aeroacoustic tool.

Unfortunately, validation of the aeroacoustic module has not been possible, due to lack of detailed wind turbine informations in the literature. A comparison with data obtained through a noise measurement campaign on a real wind turbine is then the next step needed to assess quantitative accuracy of results.

Many are the development areas opened by the present work. Under a numerical point of view, although running time of the aeroacoustic module is quite short and not even comparable with CAA computations, performances can be improved by adequate parallelization of the process. An eventual use of the present tool in an optimization process would require computation of a great number of noise analysis, making the time consumption constraint even more important. A 2d CFD solver may be included to replace Xfoil in boundary layer data computations, and a comparative study among trailing edge noise emissions obtained through different BL solver could be investigated. Turbulent inflow appear to be highly dependent on L_t and $\overline{u^2}$: many different definitions of such parameters exist and could be included in the module, to study effects on TI emissions. Finally, effects of air

absorption, terrain reflection and wind refraction can be included, in order to take into account environmental influence on sound propagation, together with wake interactions between different wind turbines. This last step would be fundamental for example in case of wind farms, in which effects of inflow variations due to a wake produces changing in noise emissions, opening the road to wind farm noise computations and reductions.

Bibliography

[1] M. Bastasch, "Summary of international wind turbine noise," 2011.

[2] "Iec-61400-11, "wind turbine generator systems – part 11: Acoustic noise measurement techniques", edition 2:2002," tech. rep.

[3] M. J. Lighthill, "On sound generated aerodynamically. i. general theory," vol. 211, pp. 564–587, The Royal Society, 1952.

[4] N. Curle, "The influence of solid boundaries upon aerodynamic sound," vol. 231, pp. 505–514, The Royal Society, 1955.

[5] J. F. Williams and D. L. Hawkings, "Sound generation by turbulence and surfaces in arbitrary motion," *Philosophical Transactions of the Royal Society of London A: Mathematical, Physical and Engineering Sciences*, vol. 264, no. 1151, pp. 321–342, 1969.

[6] J. F. Williams and L. Hall, "Aerodynamic sound generation by turbulent flow in the vicinity of a scattering half plane," *Journal of Fluid Mechanics*, vol. 40, no. 4, pp. 657–670, 1970.

[7] K. S. Brentner and F. Farassat, "Modeling aerodynamically generated sound of helicopter rotors," *Progress in Aerospace Sciences*, vol. 39, no. 2, pp. 83–120, 2003.

[8] F. Farassat, *Theory of noise generation from moving bodies with an application to helicopter rotors*. National Aeronautics and Space Administration, 1975.

[9] F. Bertagnolio, "Trailing edge noise model applied to wind turbine airfoils," tech. rep., Danmarks Tekniske Universitet, Risø Nationallaboratoriet for Bæredygtig Energi, 2008.

[10] M. S. Howe, "A review of the theory of trailing edge noise," *Journal of Sound and Vibration*, 1978.

[11] K. S. Brentner, "Prediction of helicopter rotor discrete frequency noise: a computer program incorporating realistic blade motions and advanced acoustic formulation," 1986.

[12] K. S. Brentner, L. Lopes, H.-N. Chen, and J. F. Horn, "Near real-time simulation of rotorcraft acoustics and flight dynamics," *Journal of aircraft*, vol. 42, no. 2, pp. 347–355, 2005.

[13] C. Arakawa, O. Fleig, M. Iida, and M. Shimooka, "Numerical approach for noise reduction of wind turbine blade tip with earth simulator," *Journal of the Earth Simulator*, vol. 2, no. 3, pp. 11–33, 2005.

[14] A. Rasam, J. D. Botha, K. Bolin, C. J. O'Reilly, G. Efraimsson, and H. J. Rice, "Aerodynamic noise prediction for a wind turbine using numerical flow simulations and semi-empirical modelling approaches," American Institute of Aeronautics and Astronautics, 2016.

[15] J. Botha, A. Rasam, D. Catháin, H. Rice, and A. Shahrokhi, "Some noise predictions for small wind turbines,"

[16] P. J. Morris, L. N. Long, and K. S. Brentner, "An aeroacoustic analysis of wind turbines," pp. 5–8, 2004.

[17] M.V.Lowson, "Assessment and prediction of wind turbine noise," *Flow Solutions Report 92/19*, 1993.

[18] F. W. Grosveld, "Prediction of broadband noise from horizontal axis wind turbines," *Journal of Propulsion and Power(ISSN 0748-4658)*, vol. 1, pp. 292–299, 1985.

[19] S. Glegg, S. Baxter, and A. Glendinning, "The prediction of broadband noise from wind turbines," *Journal of sound and vibration*, vol. 118, no. 2, pp. 217–239, 1987.

[20] A. S. H. Lau, J. W. Kim, J. Hurault, and T. Vronsky, "A study on the prediction of aerofoil trailing-edge noise for wind-turbine applications," *Wind Energy*, vol. 20, no. 2, pp. 233–252, 2017.

[21] R. Parchen, "Progress report draw : a prediction scheme for trailing edge noise based on detailed boundary layer characteristics," 1998.

[22] R. K. Amiet, "Acoustic radiation from an airfoil in a turbulent stream," *Journal of Sound and Vibration, Volume 41, Issue 4, p. 407-420*, 1975.

[23] R. W. Paterson and R. K. Amiet, "Acoustic radiation and surface pressure characteristics of an airfoil due to incident turbulence," *3rd AIAA Aero-Acoustics Conference (1976) Palo Alto CA*, 1976.

[24] G. Guidati, R. Bareiss, S. Wagner, T. Dassen, and R. Parchen, "Simulation and measurement of inflow-turbulence noise on airfoils," *American Institute of Aeronautics and Astronautics Paper*, pp. 97–1698, 1997.

[25] P. Moriarty, G. Guidati, and P. Migliore, "Prediction of turbulent inflow and trailing-edge noise for wind turbines," *Proc. of the 11th AIAA/CEAS Aeroacoustics Conf.(Monterey, CA), AIAA Paper*, vol. 2881, p. 2005, 2005.

[26] P. Moriarty and P. Migliore, "Semi-empirical aeroacoustic noise prediction code for wind turbines," tech. rep., National Renewable Energy Lab., Golden, CO.(US), 2003.

[27] P. Fuglsang and H. Aagaard Madsen, "Implementation and verification of an aeroacoustic noise prediction model for wind turbines," 1996.

[28] K. Boorsma and J. Schepers, "Enhanced wind turbine noise prediction tool silant," *Technical Report ECN-M-12-004*, 2011.

[29] M. Kamruzzaman, T. Lutz, A. Herrig, and E. Kraemer, "Rans based prediction of airfoil trailing edge far-field noise: Impact of isotropic & anisotropic turbulence," No. 2008-2867, 2008.

[30] J. Schepers, A. Curvers, S. Oerlemans, K. Braun, T. Lutz, A. Herrig, W. Wuerz, A. Mantesanz, L. Garcillan, M. Fischer, *et al.*, "Sirocco: silent rotors by acoustic optimisation," vol. 2021, 2007.

[31] W. K. Blake, *Mechanics of Flow-Induced Sound and Vibration, Volume 1: General Concepts and Elementary Sources*. Academic press, 2017.

[32] D. M. Chase, "Noise radiated from an edge in turbulent flow," *AIAA J*, vol. 13, no. 8, pp. 1041–1047, 1975.

[33] K. Chandiramani, "Diffraction of evanescent waves, with applications to aerodynamically scattered sound and radiation from unbaffled plates," *The Journal of the Acoustical Society of America*, vol. 55, no. 1, pp. 19–29, 1974.

[34] M. Drela, "Xfoil: An analysis and design system for low reynolds number airfoils,"

[35] F. Bertagnolio, H. Aagaard Madsen, and C. Bak, "Experimental validation of tno trailing edge noise model and application to airfoil optimization," *2009 European Wind Energy Conference and Exhibition*, 2009.

[36] K. G. Hermann Schlichting (Deceased), *Boundary-Layer Theory*. Springer-Verlag Berlin Heidelberg, ninth edition ed., 2017.

[37] F. Bertagnolio, A. Fischer, and W. Zhu, "Tuning of turbulent boundary layer anisotropy for improved surface pressure and trailing-edge noise modeling," *Journal of Sound and Vibration*, vol. 333, no. 3, pp. 991–1010, 2014.

[38] F. Bertagnolio, H. Aagaard Madsen, C. Bak, and A. Fischer, "Validation of an aero-acoustic wind turbine noise model using advanced noise source measurements of a 500 kw turbine," *2016 Proceedings of 16th International Symposium on Transport Phenomena and Dynamics of Rotating Machinery. 2016.*

[39] T. F. Brooks, D. S. Pope, and M. A. Marcolini, "Airfoil self-noise and prediction," *NASA Reference Publication 1218*, 1989.

[40] T. F. Brooks and T. H. Hodgson., "Trailing edge noise prediction from measured surface pressures.," *Journal of Sound and Vibration, 78(1):69–117*, 1981.

[41] J. Graham, "Similarity rules for thin aerofoils in non-stationary subsonic flows," *Journal of Sound and Vibration, 43(4), 753-766*, 1970.

[42] P. Moriarty, "Nafnoise and fast noise module," tech. rep., NREL, National Renewable Energy Laboratory, 2008.

[43] M. Moriarty, Guidati, "Recent improvement of a semi-empirical aeroacoustic prediction code for wind turbines," *10th AIAA/CEAS Aeroacoustics Conference*, 2004.

[44] Y. Tian, B. Cotté, and A. Chaigne, "Wind turbine noise modelling based on Amiet's theory," 2013.

[45] W. J. Zhu, N. Heilskov, W. Z. Shen, and J. N. Sørensen, "Modeling of aerodynamically generated noise from wind turbines," *Journal of Solar Energy Engineering*, vol. 127, no. 4, pp. 517–528, 2005.

[46] J. Counihan, "Adiabatic atmospheric boundary layers: a review and analysis of data from the period 1880–1972," *Atmospheric Environment (1967)*, vol. 9, no. 10, pp. 871–905, 1975.

[47] "ESDU 85020: Characteristics of atmospheric turbulence near the ground. Part 2: Single point data for strong winds (neutral atmosphere)," tech. rep., 1985.

[48] A. Croce and L. C. Bottasso, "Cp-lambda: User's manual," tech. rep., Politecnico di Milano, 2006-2011.

[49] B. Jonkman and L. Kilcher, "Turbsim user's guide," tech. rep., NREL, National Renewable Energy Laboratory, 2012.

[50] "IEC-61400-1, "wind turbines – part1: Design requirements", third edition 2005-08," tech. rep.

[51] P. Moriarty, "Nafnoise user's guide," *National Renewable Energy Laboratory*.

[52] R. H. Schlinker and R. K. Amiet, eds., *Helicopter rotor trailing edge noise*, Oct. 1981.

[53] H. Michaela, E. Roland, R. Christof, K. Mohammad, B. Dimitrios, A. Renzo, I. Andrea, B. Paul, C. Sukumar, and B. Franck, "Broadband trailing-edge noise predictions—overview of banc-iii results," *Proceedings 21st AIAA/CEAS Aeroacoustics Conference*, 2015.

[54] A. Humpf, E. Ferrer, and X. Munduate, "Investigation of computational aeroacoustic tools for noise predictions of wind turbine aerofoils," vol. 75, IOP Publishing, 2007.

[55] M. R. Fink, "Experimental Evaluation of Theories for Trailing Edge and Incidence Fluctuation Noise," *AIAA Journal*, vol. 13, pp. 1472–1477, Nov. 1975.

[56] S. Oerlemans, P. Sijtsma, and B. M. López, "Location and quantification of noise sources on a wind turbine," *Journal of Sound and Vibration*, vol. 299, no. 4–5, pp. 869 – 883, 2007.

[57] S. Oerlemans and J. Schepers, "Prediction of wind turbine noise and validation against experiment," *International journal of aeroacoustics*, vol. 8, no. 6, pp. 555–584, 2009.

[58] M. Roger and S. Moreau, "Extensions and limitations of analytical airfoil broadband noise models," *International Journal of Aeroacoustics*, vol. 9, no. 3, pp. 273–305, 2010.

Appendix A

2d Aeroacoustic Solver Input

The present appendix reports a detailed explanation of the input required by the bidimensional aeroacoustic solver.

Name	Description
Airfoil and observer data	
Airfoil profile $[-]$	Filename with the coordinates of the airfoil, used by TBL-TE and TEB noise models, and by TI if thickness correction apply
Chord $[m]$	
Distance Source-Observer $[m]$	
Span $[m]$	
Phi/Theta $[m]$	Directivity angles as reported by Brooks, Pope, Marcolini ([39], Appendix B)
Environmental and flow Settings	
Angle of attack $[^\circ]$	
Air Density $[kg/m^3]$	
Airspeed $[m/s]$	
Reference pressure $[Pa]$	Reference pressure used to express the Sound Pressure level in logarithmic scale (dB), its value is set to $P_{ref} = 2 \times 10^{-5} Pa$

Name	**Description**
Turbulence Intensity $[-]$	Intensity of the turbulence, defined as the ratio between the root mean square of velocity fluctuations and the mean velocity of the flow ($T.I. = u_{rms}/U_{mean}$), used by the turbulent inflow noise models
Turbulent lengthscale $[m/s]$	Length that indicates the main extension of the eddies impinging on the airfoil, used by turbulent inflow models
Viscosity $[m^2/s]$	
Speed of sound $[m/s]$	
Computational settings	
Frequency range $[Hz]$	Specify the range of frequency in which the noise analysis is performed, $[f_{min}, f_{max}]$
Octave fraction discretization $[-]$	Allows the use of different frequency discretization, depending on the desired octave band fraction $(1/3, 1/2, ecc...)$
Boundary layer computation $[-]$	BPM TBL-TE and TEB noise models need as input the displacement thickness of the BL, this can be given through Xfoil or BPM experimental fitting by modifying the present flag. It must be noted that BPM's experiments have been performed on a NACA0012, making the experimental fitting reliable only for this airfoil
BPM's boundary layer trip $[-]$	If the boundary layer data are obtained through empirical relations, two possible formulas are available, depending if the airfoil is considered "heavy tripped" or "untripped" [39]

Name	Description
Xfoil transition position [−]	Allows the user to force the transition of the boundary layer on the top and the bottom of the airfoil
TNO model [−]	Two possible way of computing the pressure fluctuation spectrum at the trailing edge are possible, the first aprroach considers an isotropic boundary layer and a turbulent lengthscale independent on the frequency, while the second one takes into account anisotropy of BL and dependency of the turbulent length with the frequency (see eq: 3.25)
Thickness correction flag [−]	Is it possible to choose among two possible thickness corrections for the turbulent inflow model, the Guidati method [25] and the Roger and Moreau correction [58], as reported in section 3.2.1
NAFNoise settings [−]	Not changed compared to the original one (see NAFNoise User's Guide [51])